Spring 2017

Long-period fiber grating corrosion sensors for life-cycle monitoring and assessment of reinforced concrete structures

Yizheng Chen

Follow this and additional works at: https://scholarsmine.mst.edu/doctoral_dissertations

Part of the Civil Engineering Commons

Department: Civil, Architectural and Environmental Engineering

Recommended Citation

LONG-PERIOD FIBER GRATING CORROSION SENSORS FOR LIFE-CYCLE

MONITORING AND ASSESSMENT OF REINFORCED CONCRETE STRUCTURES

by

YIZHENG CHEN

A DISSERTATION

Presented to the Faculty of the Graduate School of the

MISSOURI UNIVERSITY OF SCIENCE AND TECHNOLOGY

In Partial Fulfillment of the Requirements for the Degree

DOCTOR OF PHILOSOPHY

in

CIVIL ENGINEERING

2017

Approved by
Dr. Genda Chen, Advisor
Dr. Guirong (Grace) Yan
Dr. Lesley Sneed
Dr. Mohamed ElGawady
Dr. Jie Huang

ABSTRACT

This study aims to: (1) explore, develop, calibrate and validate Fe-C coated, long period fiber grating (LPFG) sensors for short-term mass loss measurement of the Fe-C coating; (2) develop, calibrate, and validate steel tube-encapsulated, fiber optic probes and LPFG sensors for long-term mass loss detection of the steel tube; (3) correlate the corrosion process of packaging metal materials with that of steel bars in direct contact with the packaged probe or sensor except for a thin insulation tape; and (4) apply both types of corrosion sensors into reinforced concrete (RC) structures for reinforcing bar corrosion monitoring and structural condition assessment. For short-term monitoring, the corrosion mechanism of the Fe-C coating and the corrosion sensitivity of the Fe-C coated LPFG were investigated and characterized in 3.5 wt. % NaCl solution. For long-term detection, the probe or sensor was used to measure the pitting corrosion growth of steel tubes in simulated concrete pore solution. To validate them in an application setting, two types of LPFG corrosion sensors were embedded in three RC beams under accelerated corrosion test. The resonant wavelength of a Fe-C coated LPFG sensor can be linearly related to the mass loss of Fe-C coating up to 60~90%. When tested in 3.5wt. % NaCl solution, the LPFG sensor coated with an 8~20 µm thick Fe-C layer has a sensitivity of 0.15~0.23 nm/1% Fe-C mass loss. This sensitivity is translated into approximately 1300 nm/g in mass loss of reinforcing steel bars. In RC beam applications, the resonant wavelength of an Fe-C coated LPFG sensor is reduced by 0.49 nm/hour when installed along a steel bar under accelerated corrosion conditions and 0.95 nm/day when installed near the bottom surface of a beam under natural corrosion condition. The corrosion penetration rate through the wall of a steel tube is approximately 8.6 µm/day.

ACKNOWLEDGMENTS

TABLE OF CONTENTS

LIST OF ILLUSTRATIONS

LIST OF TABLES

1. INTRODUCTION

1.1. BACKGROUND

Over the past two decades, structural health monitoring with various sensing technologies has become one of the most active and fruitful research topics in civil engineering. As illustrated in Figure 1.1, bridge experiences damage or deteriorates over time in different ways, such as concrete cracking, concrete delamination, steel reinforcement corrosion, foundation scour, fatigue and overstress. In the U.S. alone, over 1500 bridges collapsed between 1966 and 2005 [1] due to various causes as summarized in Figure 1.2. The 4% of bridge collapses was attributed to steel structures (4%), which are likely associated with steel corrosion and stability of slender members.

Figure 1.1. Schematic view of various structural behaviors.
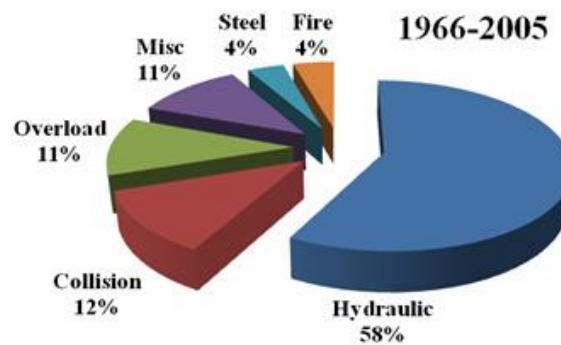
Figure 1.2. Causes of over 1500 bridge collapses.

Reinforced concrete (RC) structures, such as highway bridges, buildings, dams, and tunnels, often undergo physical and chemical deterioration when exposed to various harsh and aggressive environments. Corrosion of reinforcement steel bars is one of the

main causes of premature deterioration in RC structures [2-6]. In general, steel bars are protected by a passive film that is formed on their surface in concrete pore solution – an alkaline environment [7, 8]. However, this protective film can be destroyed by carbonation of the concrete cover or ingress of chlorides, resulting in the onset of corrosion. Once initiated, corrosion can cause cracking and delamination of the concrete cover, impair the bond between steel bars and their surrounding concrete, and reduce the cross sectional area of steel bars, thus reducing the structural load-bearing capacity [9-11]. It is estimated in 2002 that the annual direct cost of corrosion for replacement and maintenance of highway bridges in the U.S. alone is approximately $13.6 billion. The indirect cost of corrosion due to traffic delay and lost productivity was estimated to be as high as 10 times that of direct corrosion costs [12]. Therefore, it is imperative to develop an effective corrosion sensing system for corrosion monitoring of steel reinforcement, which will improve the safety and serviceability of RC structures and reduce the direct and indirect costs induced by corrosion.

Electrochemical sensors for corrosion monitoring of steel reinforcement include embedded reference electrodes, corrosion macro cell current probes, linear polarization sensors, and electrical resistance sensors [13-15]. Most of them depend on a reliable and durable reference electrode that can survive the severe environment of concrete to obtain successful measurements. Some solid reference electrodes embedded in concrete have been developed to investigate electrochemical characteristics [16, 17]. Non-electrochemical sensors are mainly based on acoustic emission [18], ultrasonic guided wave [19], chloride concentration [20, 21], oxygen concentration [22], and other parameters [23].

Compared to the above methods, fiber optic sensors have several advantages such as high sensitivity, high precision, immunity to electromagnetic interference, corrosion resistance, compactness, lightweight, multiplexed sensing points along one optical fiber, long-distance monitoring, and ease to be integrated into a large sensor network [24-27]. Many fiber optic sensors have been developed for strain [28-35], temperature [36-42], displacement [43-49], humidity [39, 50-56], PH [57-60], and crack [61, 62] monitoring and measurement. Additionally, fiber optic sensors have been applied to monitor the corrosion of steel rebar in RC structures [63, 64]. A Fe-C or iron film was coated on the

core surface or at the cleaved end of an optical fiber to directly relate steel mass loss to the change of a transmitted or reflected light spectrum [65, 66]. Fe-C was also coated on the cladding surface of a fiber Bragg gratings (FBG) sensor to measure the shift in resonant wavelength as a result of the strain induced by the volume expansion of Fe-C corrosion products [67]. Alternatively, a FBG sensor was configured such that the corrosion-induced relative movement of twin steel bars is measured and in turn related to the mass loss [68]. These approaches are indirect for corrosion monitoring and could be quite uncertain in the prediction of steel mass loss since the strain-corrosion relationship largely depends upon corrosive environment and confining condition of the FBG sensor in applications.

Long period fiber gratings (LPFGs) are inscribed on the core of an optical fiber to form a periodic modulation of refractive index over a grating length of a few centimeters [69]. The grating period in the order of 100~1000 µm can considerably exceed the wavelength of radiation propagating in the fiber. The gratings enable coupling of light from the propagating core mode to the co-propagating cladding modes at discrete wavelengths, therefore producing a series of attenuation bands in a transmission spectrum. The resonant wavelength at each attenuation peak can be calculated by phase matching condition,

$$\}_{res} = (n_{co}^{eff} - n_{cl,m}^{eff})\Lambda \tag{1.1}$$

where $_{res}$ is the resonant wavelength, is the grating period, n_{co}^{eff} and $n_{cl,m}^{eff}$ are the effective refractive indices of the fundamental core mode and the mth cladding mode, respectively. The term $n_{cl,m}^{eff}$ is a function of refractive indices of the core (n_1) and cladding (n_2) of the fiber as well as its surrounding medium (n_3). Therefore, the resonant wavelength changes with the refractive index of the medium surrounding the gratings, and LPFG has been applied into physical [70, 71], chemical [72, 73], and bio-chemical [74, 75] sensing devices.

The concept of Fe-C coated LPFG sensors for corrosion monitoring was recently proposed by Dr. Genda Chen's group [76]. To the best knowledge of the author, no other papers discuss the relationship between a transmission spectrum of the LPF sensors and its causative steel mass loss.

1.2. LITERATURE REVIEW AND STATE-OF-THE-ART DEVELOPMENT

In this section, the different electrochemical methods used in industry and research field were simply introduced. The different corrosion and its essential characteristics can be measured according to the corresponding method.

1.2.1. Electrochemical Corrosion Test and Monitoring Technology. Many techniques have been developed to test and monitor the corrosion process in steel reinforcement and members including physical, chemical and electrochemical methods [77]. The electrochemical method is one of the most effective ways to monitor the initiation and propagation of corrosion. It includes the linear polarization resistance, electrochemical impedance spectroscopy, and open-circuit potential measurements with a standard three-electrode test setup.

1.2.1.1 Linear polarization resistance (LPR). LPR is one of the most common methods to monitor the rebar corrosion in cement or concrete. It is easy to operate and just use a connection to the steel bar under monitoring. The test data show the instantaneous corrosion rate of steel bars. An electrical potential is applied to the steel bar around the open circuit potential, and then the electrical current was recorded at the same time. The applied range of potential V usually ranges from 10 to 30 mV with respective to the open circuit potential. The polarization resistance is the slope of the applied electrical potential to the measured electrical current around the open circuit potential. The resistance R_p can be calculated by:

$$R_p = \Delta V / \Delta I \tag{1.2}$$

where V represents the applied potential range and I is the measured electrical current, respectively. The corrosion current can be calculated by the Stern-Geary equation based on the polarization resistance [78]:

$$i_{corr} = \mathsf{S}_a \mathsf{S}_c / [2.303(\mathsf{S}_a + \mathsf{S}_c)R_p] = B / R_p \tag{1.3}$$

where i_{corr} is the corrosion current density, $_a$ is the anodic Tafel slope, $_c$ is the cathodic Tafel slope, and B is the Stern-Geary constant. The LPR method is influenced by factors such as temperature and humidity.

1.2.1.2 Electrochemical impedance spectroscopy (EIS). EIS is an effective and nondestructive method to monitor the corrosion of steel. This technique has been commonly used to study the corrosion mechanism of steel in solution or concrete. The

applied amplitude of potential signal is around 10 mV, and both the potential and the current signals are functions of the excitation frequency. By extracting parameters at different frequencies, EIS can be used to study the evolution of both the material and the corrosion properties, such as coating resistance/capacitance and steel-electrolyte interfacial parameters (charge transfer resistance and double layer capacitance). It is also effective to study the long-term corrosion performance of materials.

The most important procedure to analysis a EIS spectrum is to find a suitable equivalent electrical circuit (EEC). Several representative EEC models are presented in Figure 1.3.
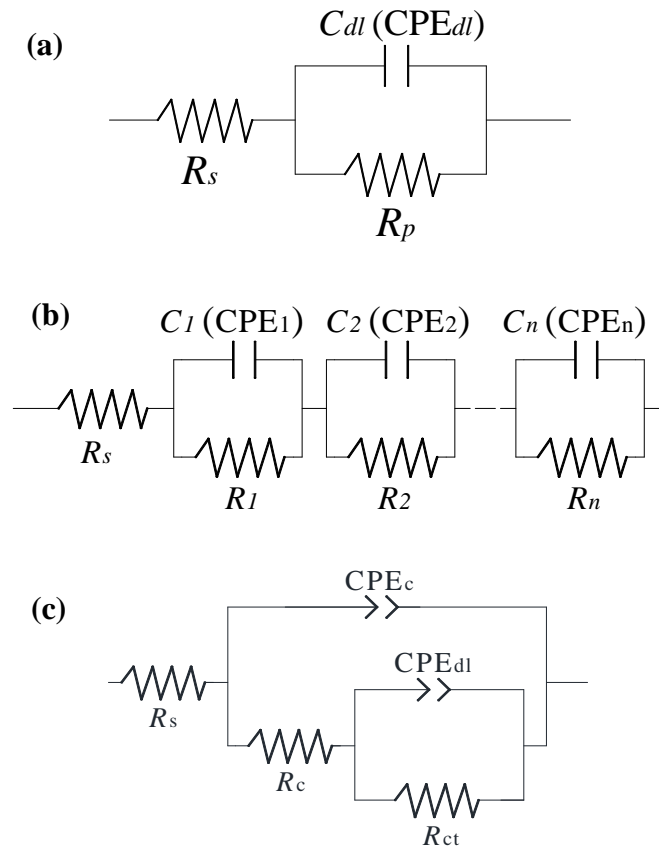
Figure 1.3. Classical electrical circuits for RC systems: (a) Randle's circuit, (b) resistor-capacitor in series, and (c) resistor-capacitor in mixed mode.

Using EIS as a corrosion monitoring technique provides some information of a steel-concrete system such as changes in the concrete resistance and corrosion evolution

from passive state to active state. Therefore, the EIS is also widely used to study the corrosion behavior of steel reinforcement in concrete structures.

        1.2.1.3 Open circuit potential (OCP). OCP, often referred to as a half-cell potential, is widely used for corrosion monitoring of reinforcement steel due to its simplicity and ease in operation. It measures two potential differences between one of two reference electrodes and a steel bar in active corrosion state. The two reference electrodes include a saturated calomel electrode (SCE) and a copper sulfate. Copper sulfate as specified in ASTM Standard C876 is widely used in concrete structures [79]. According to the C876, the probability of no corrosion is 90% when the potential exceeds -0.2 V; the corrosion activity is uncertain when the corrosion potential is between -0.2 V and -0.35 V; and the steel bar has a 90% probability of active corrosion when the corrosion potential is lower than -0.35 V (more negative).

        The OCP method has some limitations. For example, the result may be influenced by many factors [80, 81], such as chloride concentration, concrete or solution resistivity, concrete crack, and cracks in corrosion inhibitor materials. Therefore, the corrosion result measured by this method can be used to combine with other methods, such as EIS, to obtain a stable and correct result.

        1.2.1.4 Other corrosion measurement methods. In addition to the above-mentioned methods for corrosion monitoring, other techniques for corrosion detection include concrete resistivity, Tafel extrapolation, and electrochemical noise [82-95]. Concrete resistivity measurements are usually based on a four-pin array. An external potential was applied to the outer two pins, and then the electrical current was measured between the inner two pins. The concrete resistance can be obtained using the electrical potential and the measured current. However, the measurement is also affected by other environmental factors or the surface condition of the concrete specimen. Electrochemical noise analysis is also used to monitor the corrosion of RC structures. The corrosion condition of steel can be evaluated through the variation of corrosion potential noise spectra [91-95].

        1.2.2. Fiber Optic Corrosion Sensors. In recent years, a number of optical fiber sensors have been developed for corrosion monitoring. By coating a thin layer of iron film on the flat end of an optical fiber, the iron corrosion can be monitored by

observing the change in the light reflectivity over time since the iron film became thinner as corrosion proceeded [66]. A fiber optic coil winding was created based on the Brillouin mechanism to monitor the corrosion of steel rebar. The expansion strain along the fiber optic coil winding area was decided by corrosion degree and the strain was a linear function of frequency. Use of this method needs a transfer of the corrosion to strain. However, the corrosion is not directly detected and influenced by other factors which affect the strain value [96]. An assembly was also proposed to monitor the corrosion using FBG sensor. This assembly was a steel tube containing a carbon fiber and a FBG optical fiber [97]. The carbon fiber was preheated using a power and the temperature of the outside steel tube increased correspondingly. As corrosion occurred on the steel tube, the temperature would change, resulting in a temperature change around the FBG sensor. Then the spectral change of the FBG sensor reflected the degree of corrosion in the outside steel tube. A Fe-C coated FBG was also proposed to monitor steel bar corrosion [19]. The FBG sensor was firstly sputtered with an inner silver film and then electroplated with an outer layer of Fe-C coating. As corrosion proceeded, the expansive volume of corrosion products would generate a strain on the FBG sensor, resulting in a change of the reflected spectrum. The change in the resonant wavelength of the reflected spectrum was correlated to the steel bar corrosion. However, the strain is affected by many other factors such as confining condition, adhesion at the interfaces of the Fe-C coating, the silver film and the optical fiber cladding. Nano iron and silica particles were also coated on the surface of LPFG to monitor the corrosion of a steel bar [24]. The resonant wavelength is influenced by the change in the pH value of the solution due to corrosion. However, a relationship between the resonant wavelength and the corrosion mass loss was not established.

Corrosion sensors based on bare LPFGs were also investigated [98, 99]. A bare LPFG was kept straight and merged in a phenolic resin. The corrosion products dissolved in phenolic resin and changed the effective ambient refractive index of the bare LPFG. The change in ambient refractive index is dependent on the corrosion products accumulated over time.

1.2.3. Techniques to Protect Steel from Corrosion. Many methods have been developed for corrosion prevention. Fly ash, pozzolanic materials, and low-nickel stainless steel were used to increase the corrosion resistance of steel bars in concrete structures [100-102]. Corrosion inhibitors were also studied and used to improve the corrosion resistance [103, 104]. Compared with other methods, use of protective coating is one of the most effective and efficient methods to protect steel bars from corrosion. The fusion bonded epoxy (FBE) is the most widely used protective coating for steel bars in concrete structures [105-107]. Zinc Oxide component were also introduced to reduce the content of chloride and reduce the porosity of concrete [108-110]. The corrosion performance of a concrete member wrapped with a carbon fiber-reinforced polymer (CFRP) laminates or wraps was also evaluated [111-113]. The DINITROL AV 30® coating was developed for application on steel bars [114] as well.

1.3. RESEARCH OBJECTIVES AND SCOPE OF THIS WORK

In this study, novel fiber optic corrosion sensors will be developed and applied to monitor the corrosion of steel bars in mortar cylinders and concrete structures. Specifically, LPFG sensors will be packaged in two different ways to monitor both the short- and long-term corrosion processes. For short-term monitoring, an LPFG sensor is coated with a Fe-C layer with various thicknesses, which represents the main chemical elements of steel rebar, and its corrosion sensitivity and service life will be investigated in 3.5 wt. % NaCl solution. For long-term monitoring, an LPFG is incased in a small steel tube with various wall thicknesses, which is directly made from steel rebar. When the steel tube is corroded through its wall, corrosion products will deposit around the LPFG surface, resulting in a shift of transmission spectrum from the LPFG sensor. The encapsulated LPFG sensor will be embedded in RC beams to validate their performance for long-term corrosion monitoring.

To achieve the above objectives, six technical tasks are designed as follows:

(1) Develop and validate an LPFG sensor coated with a Fe-C layer for short-term corrosion monitoring and mass loss measurement in 3.5wt. % NaCl solution.

(2) Validate and correlate the Fe-C coated LPFG corrosion sensor with steel rebar corrosion in 3.5wt. % NaCl solution.

(3) Apply the Fe-C coated LPFG sensor for early-stage corrosion monitoring of steel bars embedded in mortar cylinders in 3.5wt. % NaCl solution.

(4) Develop and validate an EFPI based corrosion assembly for pitting corrosion growth monitoring in saturated $Ca(OH)_2$ and 3.5wt. % NaCl solution.

(5) Develop and apply an LPFG based sensor assembly for long-term corrosion monitoring of steel bars in concrete slabs.

(6) Apply both the short-term and long-term LPFG based corrosion sensors for the life-cycle corrosion monitoring and assessment of RC beams using accelerated corrosion tests in 3.5wt. % NaCl solution.

Tasks 1-3 are focused on corrosion monitoring in short term, Tasks 4 and 5 deal with corrosion monitoring in long term, and Task 6 represents a simple case study with RC beams to illustrate potential applications of the developed corrosion sensing technology in RC structures.

1.4. ORGANIZATION OF THIS DISSERTATION

This dissertation consists of eight sections. Except for Sections 1 and 8, each main section is organized and presented as a stand-alone paper, including a brief introduction.

Section 1 introduces the overall objectives and the scope of work, including literature reviews on related research such as electrochemical corrosion test methods, optical fiber corrosion sensors, and their respective advantages and disadvantages. Moreover, a new method for corrosion monitoring of steel bar in concrete structures is proposed and briefly described.

Section 2 proposes a novel optical fiber sensor to monitor the short-term corrosion of steel bars. An LPFG is coated with an inner layer of Ag and an outer layer of Fe-C that includes the main ingredients of steel bars to be monitored. In this way, corrosion of the Fe-C layer affects the ambient refraction index of the LPFG sensor. The change in resonant wavelength of the LPFG sensor and the EIS of the Fe-C coating are measured simultaneously so that the relationship between the change in resonant wavelength and mass loss of the Fe-C can be established. Additionally, two inner Ag layer thicknesses and three outer Fe-C layer thicknesses are considered to investigate the corrosion sensitivity of the LPFG sensor.

Section 3 uses the same fiber optic corrosion sensor as proposed in Section 2 to monitor the corrosion of a steel bar in 3.5 wt. % NaCl solution. The change in resonant wavelength of the Fe-C coated LPFG and the corrosion evolution of the steel bar are taken simultaneously in 3.5 wt. % NaCl solution. A relationship between the change in resonant wavelength of the Fe-C coated LPFG and the mass loss of the steel bar are established.

Section 4 deals with the application of the Fe-C coated LPFG corrosion sensor for corrosion monitoring of a steel bar embedded in mortar cylinder. The change in resonant wavelength of the Fe-C coated LPFG is measured using an Optical Spectral Analyzer (OSA) and the corrosion evolution of the steel bar in mortar is recorded using the EIS test. Twelve mortar cylinders are cast and tested in 3.5 wt. % NaCl solution for 105 days. Four conditions are considered with complete combinations of two Ag film thicknesses and two Fe-C coating thicknesses. The relationships between the change in resonant wavelength and the corrosion mass loss are established.

Section 5 develops an LPFG sensor encapsulated in a steel tube for pitting corrosion monitoring. The sensor is immersed directly in saturated $Ca(OH)_2$ added with 3.5 wt. %NaCl. The pitting corrosion rate of the encapsulating steel tube is measured using the linear polarization resistance tests, and the change in resonant wavelength of the LPFG was recorded using an OSA. The corrosion pit depth is related to the immersion time.

Section 6 characterizes the performance of an LPFG sensor encapsulated in a steel tube of varying wall thickness. The gratings are completely encased in the steel tube using Marine Epoxy. Five encapsulated LPFG sensors are embedded in a concrete slab for their long-term corrosion monitoring. To accelerate the corrosion test, external current is applied to each steel tube. The mass loss of the steel tube is related to the corrosion penetration time, T_c, when a small hole becomes to show up through the wall thickness of the steel tube.

Section 7 deals with the application of both the Fe-C coated LPFG sensor and the encapsulated LPFG sensor for corrosion monitoring of steel bars in RC beams. Three identical RC beams with a length of 3 ft and a cross section of 6 in $\times$ 6 in are cast and tested. The Fe-C coated LPFG sensor is attached to the surface of a steel bar using

adhesive, and the LPFG sensors encapsulated in steel tubes with different wall thicknesses are attached on the surface of one or more steel bars. The steel bars in RC beams are subjected to accelerated corrosion tests. To investigate the effect of corrosion on the mechanical degradation of RC beams, the RC beams are tested under four-point loading at different corrosion stages. In the end, the reduction in load-carrying capacity due to corrosion is correlated with the change in resonant wavelength measured using the corrosion sensors.

Section 8 summaries the research outcomes, findings, and future works.

2. DEVELOPMENT AND VALIDATION OF AN Fe-C COATED LPFG SENSOR FOR CORROSION MONITORING OF STEEL

2.1. INTRODUCTION

This study aims to understand the mechanism of Fe-C coated sensors for corrosion-induced mass loss measurement, and to determine the sensitivity coefficients of various sensors. A Fe-C coated LPFG sensor consists of long period gratings on an optical fiber, an inner layer of deposited Ag film, and an outer layer of electroplated Fe-C coating. The Ag layer provides a conductive film on the optical fiber that is needed for the electroplating of the Fe-C layer. The Fe-C mixture represents the main chemical composition of low carbon steel bars that are widely used in reinforced concrete structures. To determine sensor sensitivities in various conditions, two Ag film thicknesses and three Fe-C coating thicknesses are considered. The change in resonant wavelength of the LPFG sensor is related to the mass loss of the Fe-C coating by conducting the corrosion test of Fe-C coated LPFG sensors in 3.5wt. % NaCl solution. The microstructures of Ag and Fe-C layers are examined. At the completion of corrosion tests, forensic study is conducted to investigate the sensing mechanism for mass loss measurement.

2.2. EXPERIMENTAL PROCEDURE

In this section, the experimental procedure including preparation of bare LPFG, deposition of silver coating on LPFG, electroplating Fe-C layer on silver layer was described in detail. Then, the spectrum of LPFG and the corrosion rate of Fe-C layer were measured by an optical spectrum analyzer (OSA, Yokagawa AQ6370C) and EIS, respectively.

2.2.1. Preparation of Fe-C Coated LPFG Sensors. An Ag layer was deposited around the grating region by the Discovery-18 Deposition System at a chamber pressure of ~2×10^{-6} m Bar. All the cleaned optical fibers were fixed on a copper frame to ensure that they were kept straight during Ag deposition. The copper frame was placed on a stage that was rotated at a constant speed to ensure a uniform Ag film. Two thicknesses of the Ag layer, 800 nm and 1200 nm, were achieved after deposition for 1.5 and 2.5 minutes, respectively.

After Ag deposition, a layer of Fe-C was electroplated directly on the silver film. The composition of the electroplating solution and the operation parameters of the electroplating process are given in Table 2.1 [67]. The mixture of this solution is intended to produce a Fe-C layer with the same mass ratio of Fe to C as that in reinforcement steel bars. To protect the Ag film from damage and have a good electrical connection, a conductive rubber was wrapped around the Ag coating at the end of the Ag coated optical fiber on which an alligator clip was clamped. For electroplating, an approximately 6.5 cm of the Ag coated optical fiber centered around the LPFG sensor was immersed in the solution. The alligator clip and a graphite rod probed into the solution were connected with the negative and positive ends of an external power supply, respectively, producing a direct current of 2.5 mA. The electroplating process lasted for 1.0 hour, 1.5 hours, and 2.0 hours to produce a Fe-C coating thickness of approximately 8 µm, 14 µm, and 20 µm, respectively.

A total of six LPFG sensors were prepared and tested including two Ag film thicknesses and three Fe-C coating thicknesses. Figure 2.1 shows a schematic view of a Fe-C coated LPFG sensor.

Table 2.1. Bath composition and electroplating condition [67]

$FeSO_4 \cdot 7H_2O$ (g/L)	Citric Acid (g/L)	L-ascorbic acid (g/L)	pH	I (mA/cm^2)	Temperature
40	1.2	3.0	2.5	6	21°C
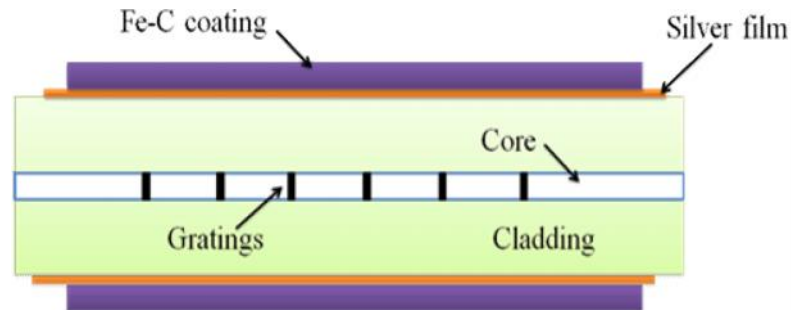
Figure 2.1. Schematic view of a Fe-C coated LPFG sensor.

2.2.2. Characterization of Ag and Fe-C Layers. To better understand the microstructure of Ag and Fe-C layers, two additional fibers were prepared with Ag and Fe-C coatings. Both the surface morphologies and the cross-sectional images of Ag and Fe-C layers were examined using a scanning electron microscopy (SEM S4700, Hitachi, Kyoto, Japan). To prepare a cross-sectional SEM sample, a small piece of the Ag and Fe-C coated fibers were cold mounted with EpoxyMount (Allied High Tech Products Inc.). After 24 hours of curing, the Epoxy mounted fibers were cross-sectioned using a diamond saw, and then abraded using a series of silicon carbide papers to 1200 grit. After abrading, the sample was rinsed with de-ionized water and dried for SEM study.

The surface condition on fiber gratings affects the resonant wavelength of an LPFG sensor. Therefore, the change in the resonant wavelength of each sensor was measured in air and 3.5 wt. % NaCl solution, respectively, with an optical spectrum analyzer (OSA, Yokagawa AQ6370C, accuracy: 0.02nm) after Ag deposition and Fe-C electroplating.

2.2.3. Electrochemical and Optical Spectra Measurements. To prevent the LPFG sensor from bending, the Fe-C coated portion was stretched and fixed to a dumbbell-like plastic bar during tests. Both the plastic bar and the Fe-C coated fiber were immersed in 3.5 wt. % NaCl solution, which was made of distilled water and NaCl powder (certified powder, Fisher Scientific). Electrochemical impedance spectroscopy (EIS) was used to monitor the corrosion process of the Fe-C coating. Before each EIS test, a stable open circuit potential was recorded. EIS tests were conducted with a typical three-electrode setup that consists of a 25.4 mm $\times$ 25.4 mm $\times$ 0.254 mm platinum sheet as a counter electrode, a saturated calomel electrode (SCE) as a reference electrode, and a Fe-C coated fiber as a working electrode. These electrodes were connected to a Gamry, Reference 600 potentiostat/galvanostat/ZRA for data acquisition. The EIS measurements were taken at 5 points per decade when a sinusoidal potential of 10 mV with a frequency range 5 mHz to 100 kHz was applied around the open-circuit potential.

The change in the transmission spectrum of a Fe-C coated LPFG fiber during immersion tests was recorded with an optical spectrum analyzer (OSA). One end of the LPFG sensor was connected to a broadband source (BBS, HP83437A) and the other end

was connected to the OSA. The optical measurements were taken every 12 minutes automatically.

Since optical fiber is small in diameter and curved circumferentially, it is difficult to visually observe the corrosion evolution of the Fe-C layer. Therefore, a silicon disk of 10 mm in diameter and 2.00 mm in thickness was also Ag deposited and Fe-C electroplated, and immersed in 3.5 wt. % NaCl solution at the same time. The thicknesses of inner Ag and outer Fe-C layers are 800 nm and 14 µm, respectively. The surface condition of the Fe-C layer was examined with an optical microscopy (Hirox KH-8700) after 0, 7, 12, and 24 hours of immersion in the salt solution.

2.3. RESULTS AND DISCUSSION

In this section, the microstructure of Ag and Fe-C layers was illustrated through SEM. The relationship between resonant wavelength and time was obtained by measuring the spectrum of Ag and Fe-C layer coated LPFG with six thicknesses. The corrosion rate of Fe-C layer was measured through corrosion test.

2.3.1. Microstructure of Ag and Fe-C Layers. Figure 2.2 shows the surface and cross-sectional SEM images of the thickest Ag film and Fe-C coating applied on the optical fiber as well as the LPFG sensor before and after corrosion tests. As shown in Figure 2.2(a), the Ag film is approximately 1.2 µm thick with randomly distributed grains. The size of the Ag grains is 92±25 nm. As shown in Figure 2.2(b), the electroplated Fe-C coating has a dendritic structure with small Fe-C grains (27±5 nm) that are likely accumulated around large silver grains. The Fe-C coating is approximately 20 µm thick. Figures 2.2(c-1) and 2.2(c-2) show the surface morphologies of the Fe-C coated LPFG sensor prior to the corrosion test and after 24 hours of immersion in 3.5 wt. % NaCl solution. The NaCl solution was made from the purified sodium chloride and distilled water. The scattered grains on the surface of the LFFG sensor as shown in Figure 2.2(c-1) represent the pitting corrosion products formed in air during preparation for SEM imaging. After 24 hours in salt solution, the LPFG surface was covered with a significant amount of corrosion products, increasing the outer diameter from 165 µm to 400 µm as shown in Figure 2.2(c-2).

2.3.2. Change of Transmission Spectra. Figure 2.3(a) shows the change of transmission spectra of a representative LPFG sensor prior to coating (bare fiber), after Ag deposition (800 nm thick), and after Fe-C electroplating (8 µm thick) when tested in air and 3.5 wt. % NaCl solution, respectively. Each transmission spectrum was taken after one minute of immersion in the NaCl solution.
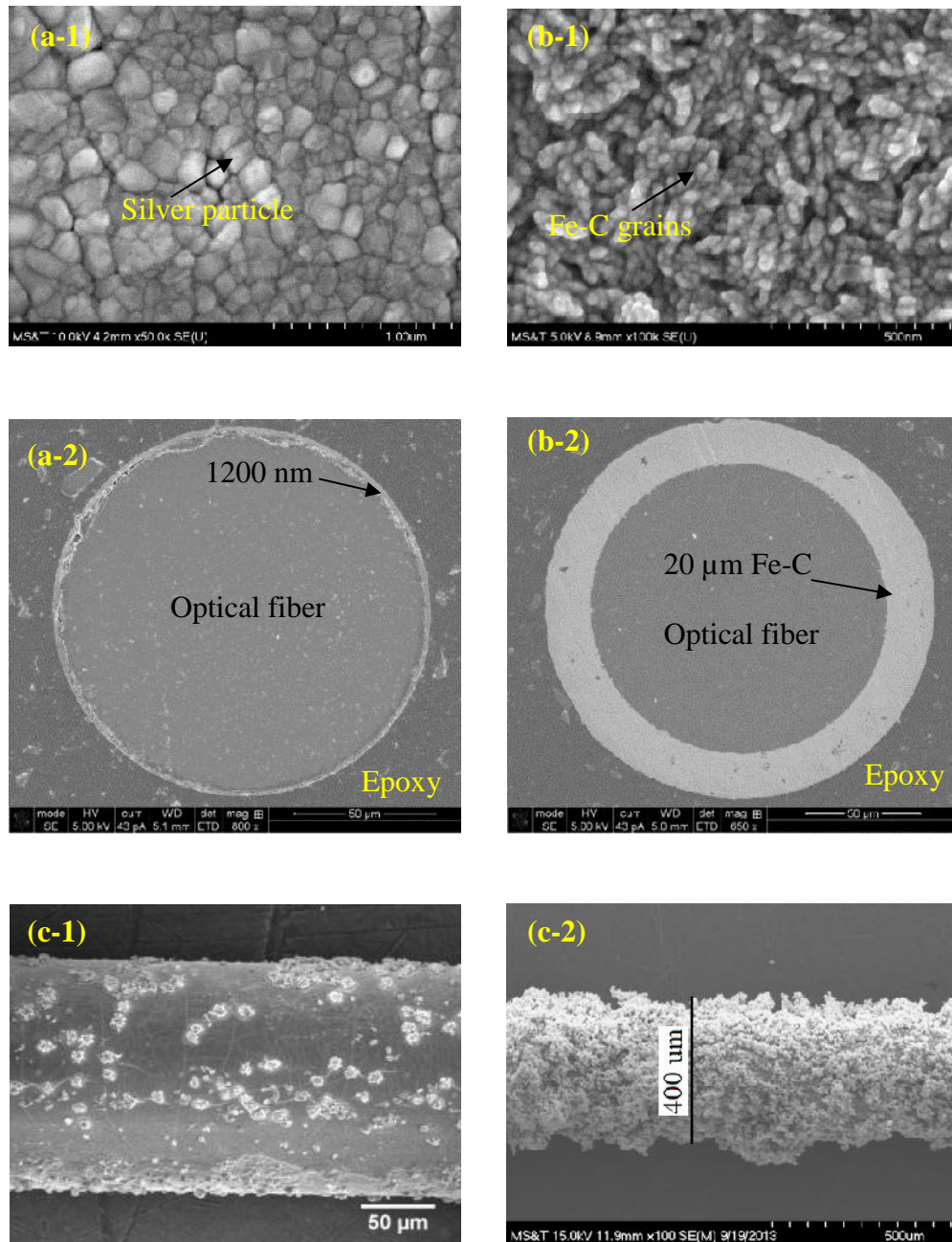
Figure 2.2. Surface (1) and cross-sectional (2) morphologies of (a) Ag film and (b) Fe-C coating; (c) SEM of the LPFG surface (1) before and (2) after 24 hours of tests.

The resonant wavelength of the bare fiber was 1526.2 nm in air, and blue shifted to 1516.2 nm once immersed in NaCl solution. This shift was attributed to the change of refractive index from air (~1.00) to NaCl solution (~1.34) [115, 116]. After Ag deposition, the resonant wavelength increased to 1557.4 nm and the corresponding transmission was changed from -24.12 to -9.25 dB. This was because the Ag film acts as a mirror to the evanescent field and part of the light was recoupled to the fiber core mode [117]. When electroplated with Fe-C coating, the pores among the Ag grains were filled with Fe-C grains, making it more dispersive to light with increasing refractive index and thus resulting in an increased bandwidth of the transmission spectrum and a blue shift of resonant wavelength to 1548.2 nm. The transmission spectrum of either the Ag or the Fe-C coated fiber was not affected by the environmental condition (air versus NaCl solution). This is because the two coatings prevent the arrival of NaCl solution to the fiber cladding in a short time (one minute), resulting in no change in the ambient refractive index.
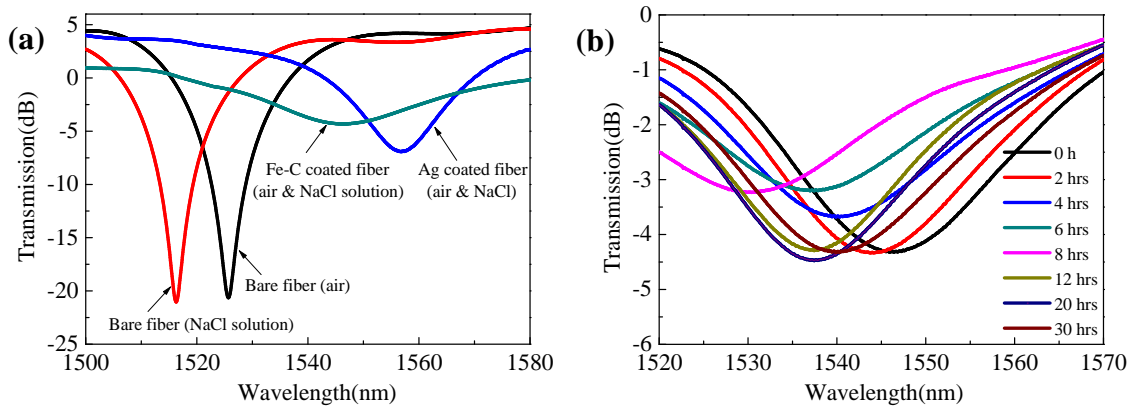
Figure 2.3. Transmission spectra of an LPFG sensor (a) coated and uncoated when tested in air and 3.5wt. %NaCl solution immediately, (b) coated with Ag (800 nm) and Fe-C (8 µm) layers when tested in 3.5 wt. % NaCl solution over time.

Figure 2.3(b) shows the change of transmission spectra of the same Fe-C coated LPFG sensor after immersion in 3.5 wt. % NaCl solution for up to 30 hours. It can be observed from Figure 2.3(b) that the resonant wavelength significantly decreased in the first 8 hours and then slightly increased after that. The rapid decrease in the first 8 hours is attributed to the corrosion of the Fe-C coating, and the solution penetration through the Ag grains till the arrival to the fiber surface, resulting in a continuing increase of the

ambient refractive index. After 8 hours, the slow increase and stabilization of wavelength are both due to the change of refractive index of salt solution as a result of the dissolution of corrosion products.

The changes in resonant wavelength of all six LPFG sensors with different Ag and Fe-C thicknesses are plotted in Figure 2.4 as a function of immersion time in 3.5wt. %NaCl solution. The wavelength change over time can be divided into three stages: I-significant decrease, II-small increase, and III-stabilization. In Stage I, the Fe-C reacted with oxygen dissolved in the salt solution as verified by pitting corrosion later, resulting in the thinning of the Fe-C coating and penetration of salt solution though the Ag film to the surface of the optical fiber. In Stage II, most of the Fe-C grains were turned into corrosion products, slightly reducing the refractive index of the salt solution as a result of the dissolution of corrosion products. In Stage III, all the Fe-C grains were turned into corrosion products and no further corrosion occurred, thus maintaining a constant resonant wavelength.

To understand the sensitivity and service life of Fe-C coated LPFG sensors, the maximum reduction of resonant wavelength and the time needed to reach the maximum reduction are extracted from Figure 2.4. They are presented in Figure 2.5(a) and 2.5(b), respectively, as a function of the Fe-C thickness. It can be seen from Figure 2.5(a) that the resonant wavelength decreases almost linearly with the Fe-C thickness when the Ag film is 800 nm thick. When an Ag film of 1200 nm thick is used, the effect of the Fe-C coating thickness appears negligible. As indicated in Figure 2.5(b), the time to reach the maximum reduction in resonant wavelength increases linearly with the Fe-C coating thickness when the thickness of Ag film is kept the same. The time also increases with the Ag film thickness when the thickness of the Fe-C coating is kept the same. This is because it takes more time to get a thicker Fe-C coating corroded completely or diffuse salt solution through a thicker Ag film. As indicated by Figure 2.5(a) and Figure 2.5(b), the selection of a Fe-C coating thickness is a trade-off between the sensitivity of corrosion measurement and the service life of Fe-C coated LPFG sensors except that the thickness of Ag film exceeds 1.2 μm.
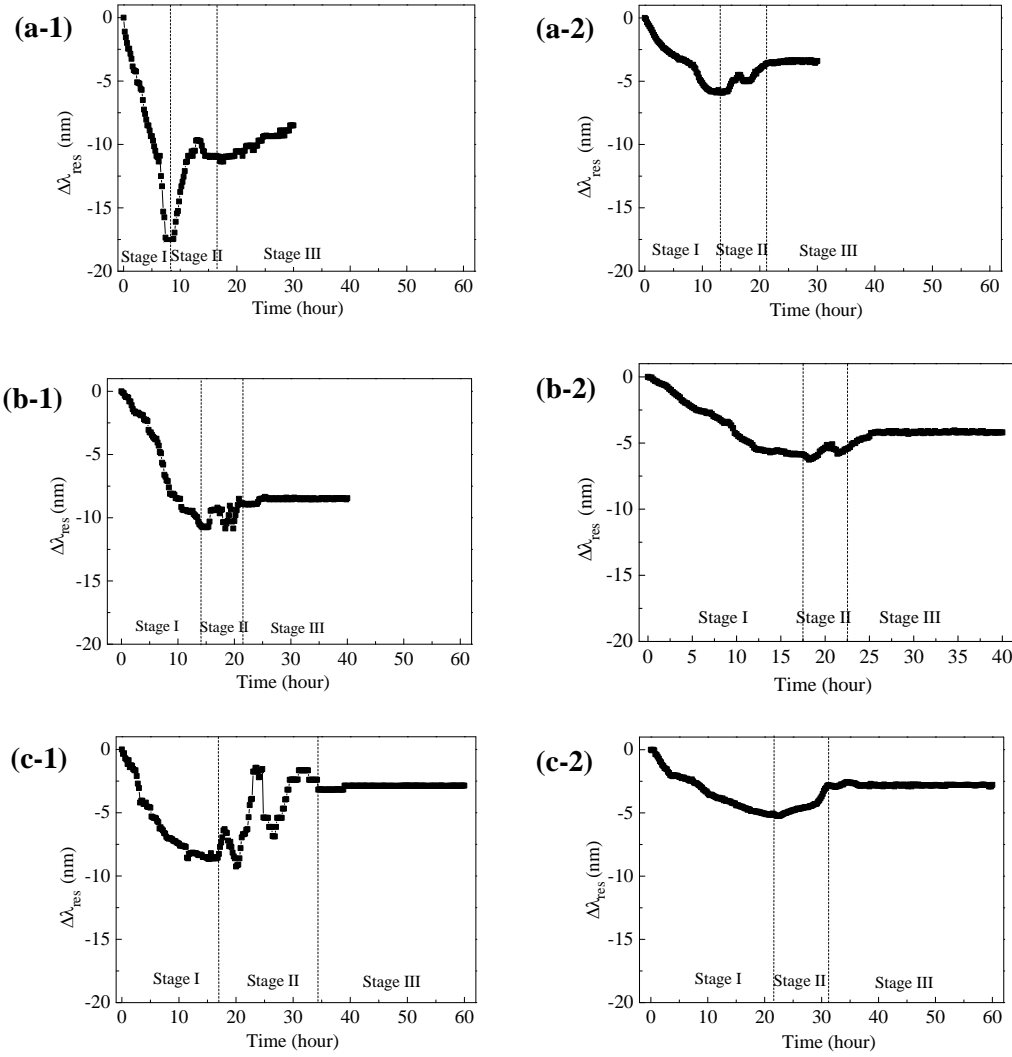
Figure 2.4. The change of resonant wavelength over immersion time in 3.5 wt. % NaCl solution for LPFG sensors with Ag thickness of (1) 800 nm, and (2) 1200 nm; Fe-C thickness of (a) 8 µm, (b) 14 µm, and (c) 20 µm.
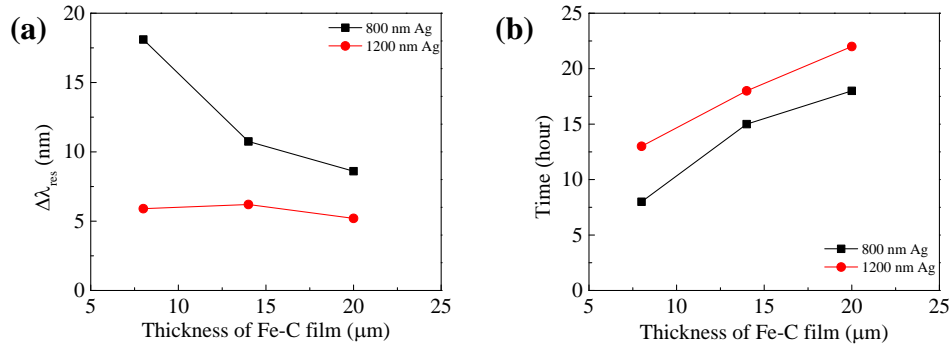
Figure 2.5. Effect of the thickness of Fe-C coating on (a) maximum change of resonant wavelength, and (b) time needed to reach the maximum resonant wavelength change.

2.3.3. EIS Results of the Fe-C Coating. Note the difference between this and the others. Figure 2.6 displays the open circuit potential (OCP) of Fe-C layer on the six LPFG sensors as a function of immersion time in 3.5 wt. % NaCl solution. The evolution of OCP over time can be divided into three stages: active (OCP < 500 mV), transition (500 mV < OCP < 280 mV) and depletion (OCP > 280 mV). In the active stage, the Fe-C coating reacts with oxygen dissolved in the salt solution and are gradually changed into corrosion products. In the transition stage, as the corrosion products are accumulated to some degrees, the remaining Fe-C grains continue to corrode but at significantly reduced rates. In the depletion stage, over 80% of the Fe-C grains have been changed into corrosion products. The thickness of Fe-C coating significantly affects the transition of stages. It can be observed from Figure 2.6 that the 8 µm thick Fe-C coating entered into the transition stage after approximately 8 hours of immersion in 3.5 wt. % NaCl solution, and continued to enter the depletion stage after 18 hours. The transition times from the first stage to the second stage were postponed to 20 hours and 25 hours for the 14 µm and 20 µm thick Fe-C coatings, respectively.
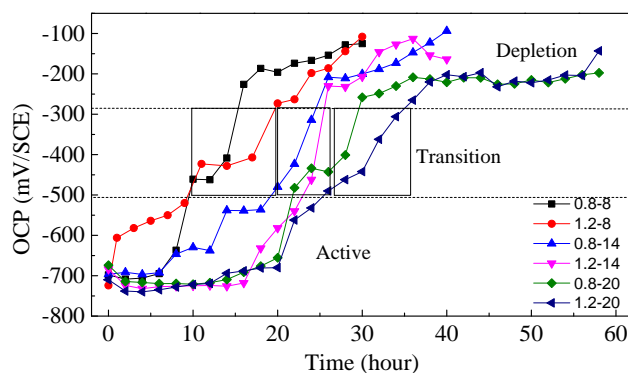
Figure 2.6. The change of open circuit potential over time for six Fe-C coated LPFG sensors (1.2-8 means an LPFG sensor coated with 1.2 µm Ag and 8 µm Fe-C).

Figure 2.7 shows the impedance spectra of Fe-C coating on the six LFFG sensors measured at six immersion times in 3.5 wt. % NaCl solution. Dot points mean experimental data and solid lines represent the data fitting results using an equivalent electrical circuit as shown in Figure 2.8. It can be seen from Figure 2.7 that the impedance spectra of all six specimens follow the same trend over time. Two semi-circles are present in the Nyquist plot. The big semi-circle in the low frequency range

corresponds to the electrolyte-iron interfacial properties: the charge transfer resistance and the double layer capacitance. The small semi-circle in the high frequency range is associated with the pore resistance and capacitive behavior of the Fe-C coating. The radius of the big semi-circle increases over the immersion time, indicating a reduced corrosion rate in the remaining Fe-C coating. When the Fe-C coating becomes thicker, the initiation time for sudden increase of the impedance spectrum is postponed.
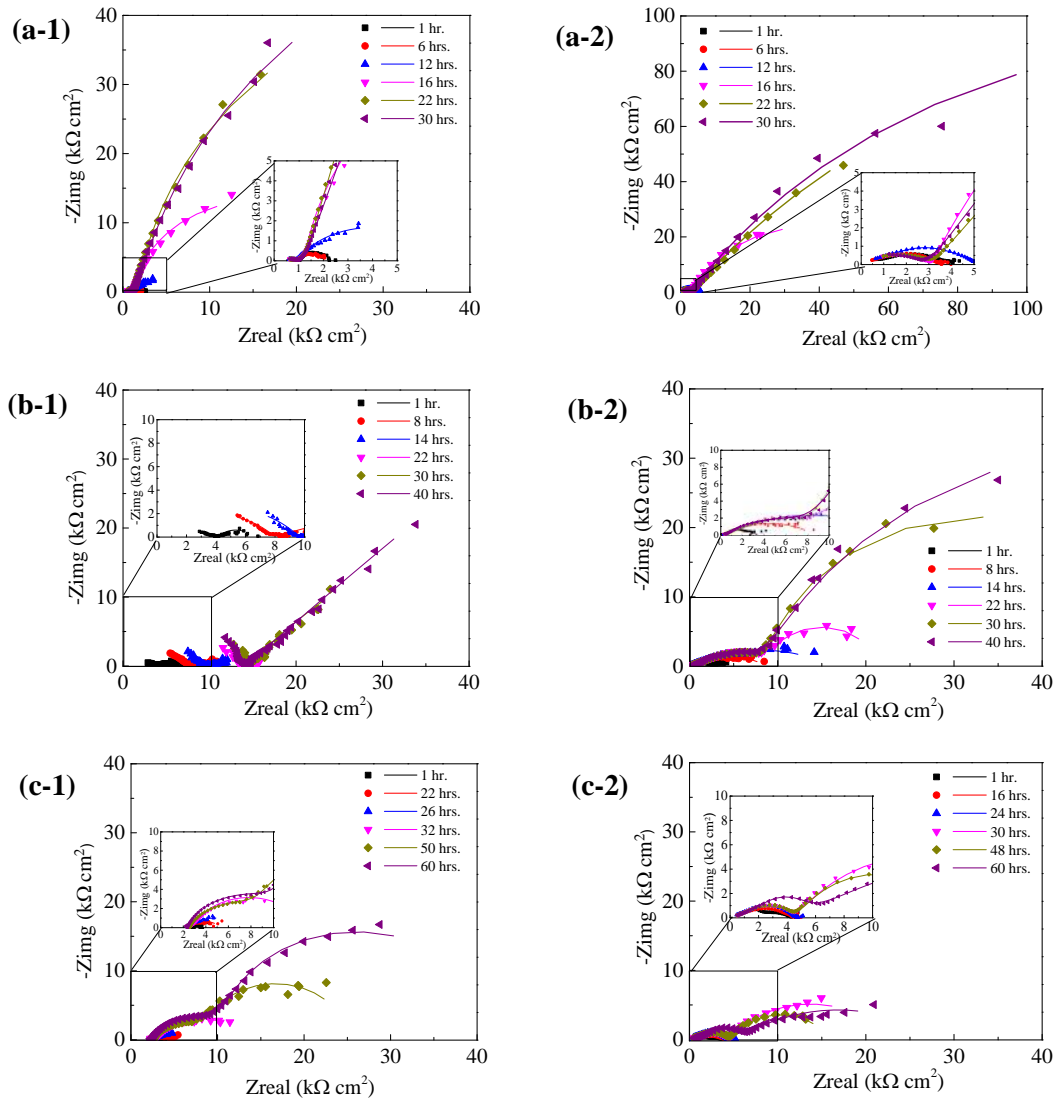
Figure 2.7. The change of impedance spectrum over time for LPFGs in 3.5 wt. % NaCl solution with Ag thickness of (1) 0.8 µm, and (2) 1.2 µm; Fe-C thickness (a) 8 µm, (b) 14 µm, and (c) 20 µm.

Figure 2.8 shows the equivalent electrical model (EEC) used to fit the impedance spectrum data in Figure 2.7 [118, 119]. Here, Rs corresponds to the electrolyte resistance, CPEc and Rc represent the pore resistance and capacitive behavior of the Fe-C coating, CPEdl and Rct represent the double layer capacitance and the charge transfer resistance at the electrolyte-particle interface. A constant phase element (CPE) instead of a pure capacitor was used to account for the non-homogeneity of the Fe-C coating and the double layer. The non-homogeneity of the Fe-C coating is attributed to the random distribution of Fe-C particles and the slight thickness variation over the entire surface as shown in Figure 2.2(b-1). The non-homogeneity of the double layer is attributed to the irregularities of the Fe-C coating such as surface roughness, random distribution of corrosion microcell, and certain processes associated with an irregular distribution of the applied potential [120]. Mathematically, the impedance of a CPE can be expressed into [121]:

$$Z_{CPE} = Y^{-1} \cdot (j\check{S})^{-n} \tag{2.1}$$

where Y is the CPE-constant with unit $^{-1}$ cm^{-2} s^{n}, which is directly proportional to the double layer capacitance of pure capacitive electrode [122], n is the CPE-power ($0 < n < 1$), j is the imaginary unit ($j^2 = -1$), and is the angular frequency of the applied alternative current ($= 2 f, f$ is the frequency in Hz).
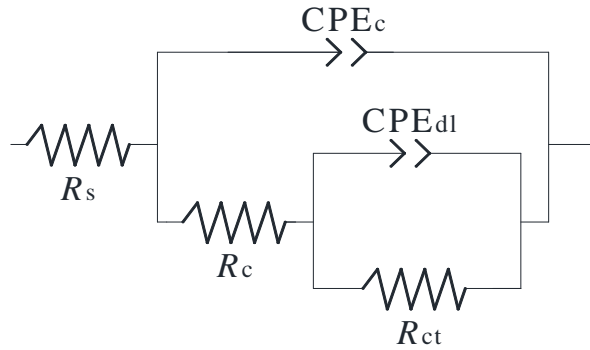
Figure 2.8. Equivalent electrical circuit model.

Among these EEC parameters, only the evolution of the charge transfer resistance over time is presented in Figure 2.9(a). Charge transfer resistance reflects the ease of charge across the electrolyte-particle interface. It can be observed from Figure 2.9(a) that,

with an increase of immersion time, the charge transfer resistance increased slightly and rapidly, and finally was stabilized when the Fe-C coating was completely corroded away. This observation is consistent with that based on the OCP data. Charge transfer resistance can be converted into corrosion rate by [123]:

$$i = B / R_{ct} \tag{2.2}$$

where i is the corrosion rate and B is a constant that was taken as 26 mV [124]. As shown in Figure 2.9(b), the corrosion rate of all Fe-C coatings on the fiber surface decreased with the immersion time in 3.5wt. % NaCl.
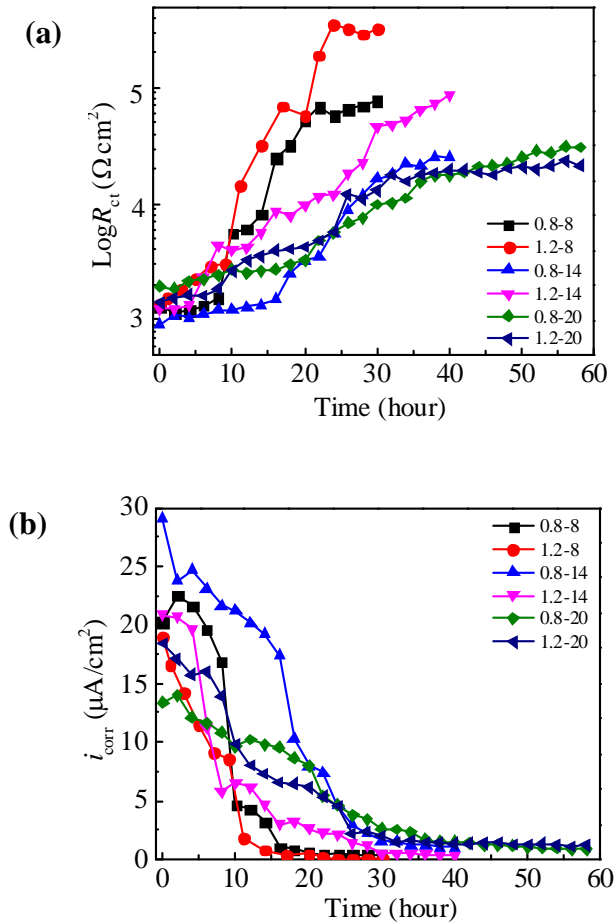
Figure 2.9. The change of (a) charge transfer resistance and (b) corrosion rate over time for six LPFG sensors (1.2-8 means a LPFG sensor with 1.2 µm Ag and 8 µm Fe-C).

2.3.4. Resonant Wavelength Vs. Corrosion Mass Loss. The corrosion rate was converted into mass loss ( ) of the Fe-C coating based on Faraday's law. By comparing Figure 2.9 with Figure 2.4, the mass loss of the Fe-C coating can be related to

the change of resonant wavelength for all six LPFG sensors as presented in Figure 2.10. Corresponding to Figure 2.4, three stages are clearly identifiable. Linear regression analysis for Stage I shows the coefficient of determination R^2 0.90. Therefore, the change in resonant wavelength can be linearly related to the mass loss of the Fe-C coating. The slope of the straight line represents the sensitivity of LPFG sensors for mass loss measurement as presented in Table 2.2 for all six sensors with Fe-C coating.
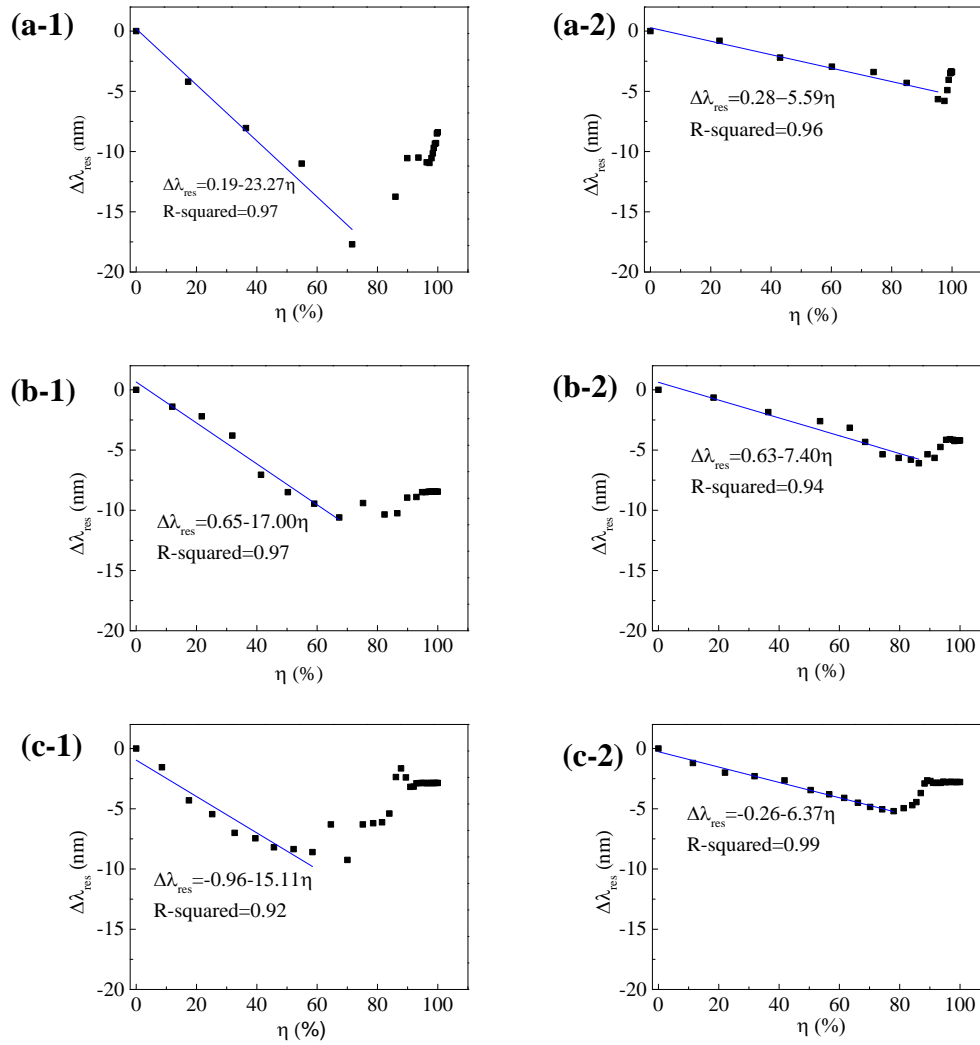
Figure 2.10. The change of resonant wavelength as a function of corrosion mass loss of Fe-C coating on various LPFG sensors with Ag thickness of (a) 0.8 μm, and (b) 1.2 μm; Fe-C thickness (1) 8 μm, (2) 14 μm, and (3) 20 μm.

As shown in Table 2.2, the LPFG sensor with 0.8 μm Ag and 8 μm Fe-C layers is most sensitive to the loss of Fe-C mass with a sensitivity of 0.23 nm per 1% mass loss of

the Fe-C coating. Given a Ag film of 0.8 μm in thickness, the sensitivity of LPFG sensors decreased from 0.23 nm to approximately 0.15 nm per 1% mass loss with an increase of the outer Fe-C coating thickness from 8 μm to 20 μm. The LPFG sensors with 1.2 μm thick Ag film are least sensitive to the mass loss with a sensitivity of approximately 0.06 nm per 1% mass loss of the Fe-C coating, regardless of the thickness of Fe-C coating. The working range of LPFG sensors for effective corrosion monitoring is 60~90% mass loss of Fe-C coating, depending upon the thickness of both inner Ag and outer Fe-C layers.

Table 2.2. Effects of Ag and Fe-C layers on the sensitivity of sensors

Coating thickness		Sensitivity	Effective range
Inner Ag (μm)	Outer Fe-C (μm)	(nm/1% mass loss)	(% mass loss)
	8	0.23	70
0.8	14	0.17	70
	20	0.15	60
	8	0.06	95
1.2	14	0.07	90
	20	0.06	80

2.3.5. The Sensing Mechanism and Corrosion Sensitivity. As indicated in Eq. (2.1), the resonant wavelength of a LPFG sensor is a function of the refractive index of surrounding medium, which is significantly affected by the type and concentration of chemicals around the fiber cladding. The surrounding medium of a Fe-C coated LPFG sensor changes over time as corrosion of the Fe-C coating proceeds. Figure 2.11 schematically illustrates various stages experienced by the corrosion sensor. In Stage I when the Fe-C coated LPFG sensor is just immersed in 3.5wt. % NaCl solution, the fiber cladding is surrounded by porous Ag particles. In Stage II, hundreds and thousands of micro-cells (pitting corrosion) are formed. These active corrosion cells have different corrosion rates due to the varying surface roughness and concentration of oxygen dissolved in the salt solution. When the first group of active corrosion cells are extended through the thickness of the Fe-C coating, electrolyte rich in chloride, sodium, Fe^{2+}, OH^-

and other ions is penetrated through the Ag pores to the surface of the fiber cladding. The air among the Ag particles beneath the active corrosion sites is replaced with the electrolyte, resulting in the change in refractive index of the surrounding medium. In Stage III, the corrosion continued until most of the pores among the Ag particles is filled with such electrolyte. This occurs when 60~90% of the Fe-C corroded as discussed previously. In Stage IV, all the Fe-C grains are turned into iron oxides or iron hydroxides and the pores among the Ag particles are filled with the salt solution and the corrosion products dissolved.
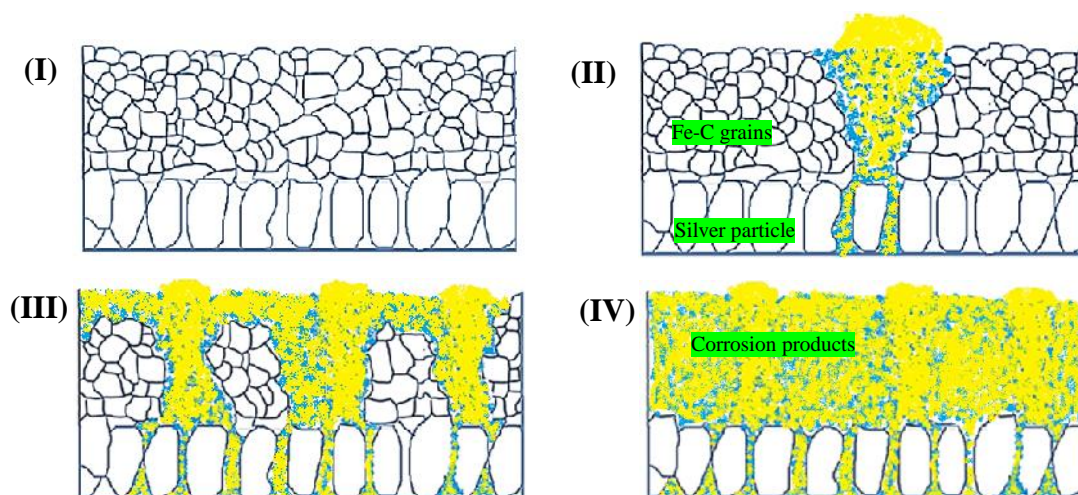
Figure 2.11. Schematic illustration of various stages of corrosion.

Figure 2.12 shows the surface conditions of a silica disk with an inner Ag film (0.8 µm) and an outer Fe-C coating (14 µm) when immersed in 3.5 wt. % NaCl solution for various periods of time. The surface images of the electroplated disc were taken at 0, 12, 25, and 40 hours as presented in Figure 2.12. In the beginning of corrosion tests, the electroplated Fe-C coating displayed a smooth black surface. After 12 hours of immersion, a number of active corrosion sites appeared and were randomly distributed over the entire surface. After 25 hours, over 90% of the Fe-C surface was covered with corrosion products as shown in Figure 2.12(c), which corresponds to Stage III in Figure 2.11. At the end of the corrosion tests (40 hours), the entire Fe-C surface was covered with corrosion products.
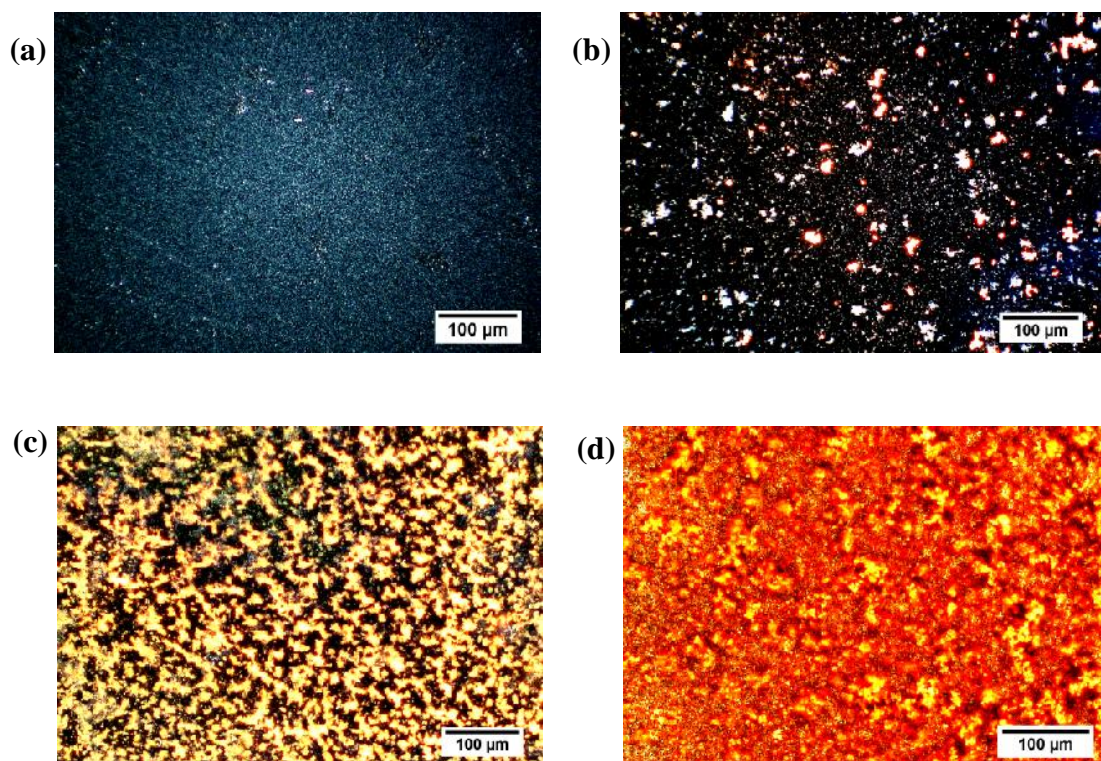
Figure 2.12. The surface condition of a silica disc with 0.8 µm Ag film and 14 µm Fe-C coating at an immersion time of (a) 0 hr., (b) 12 hrs., (c) 25 hrs., and (d) 40 hrs.

2.4. CONCLUSIONS

In this study, Fe-C coated LPFG sensors were characterized in 3.5 wt. % NaCl solution for microstructures, sensitivity in corrosion mass loss measurement, service life, corrosion behavior, and sensing mechanism. The sensors were composed of an inner deposited Ag film and an outer electroplated Fe-C coating. Based on the test results, the following conclusions can be drawn:

(1) The Ag film has a granular structure of particles that are 125 nm in size, and the Fe-C coating has a dendritic structure of grains that are approximately 27 nm in size. Both structures are porous, allowing the penetration of salt solution over time.

(2) Given a Ag film of 0.8 µm thick, the change in resonant wavelength of the sensors decreases from 0.23 nm to approximately 0.15 nm per 1% corrosion mass loss of the Fe-C coating that is originally set 8 µm to 20 µm thick. However, when the Ag film becomes 1.2 µm thick, the effect of the Fe-C thickness on the LPFG sensitivity is negligible.

(3) The service life of the sensors increases with the thickness of either Ag film or Fe-C coating. It is a trade-off of the sensitivity of the sensors unless the Ag film is 1.2 μm thick.

(4) The change in resonant wavelength of the sensors is linearly related to the loss of Fe-C mass. Therefore, the sensors can be used to predict the corrosion mass loss of the Fe-C coating up to 60~90% by measuring the change in resonant wavelength.

3. CORROSION MONITORING OF STEEL BARS BY LONG PERIOD FIBER GRATING SENSORS COATED WITH A THIN Fe-C LAYER

3.1. INTRODUCTION

In this study, the corrosion of steel rebar is monitored by distributed optical fiber grating sensors deployed in parallel with the rebar. Long period fiber grating (LPFG) sensors are coated with a thin Fe-C layer whose corrosion can be correlated with the rebar corrosion. Light can propagate through the core and cladding of a LPFG sensor. The cladding mode of light propagation is significantly affected by the environmental refractive index of the sensor, resulting in a potential change of wavelength over time. The wavelength change is related to the degree of corrosion through laboratory calibration tests by placing both the LPFG and a reinforcing steel bar in the same corrosion environment. The wavelength change and the corrosion degree are quantified by an optical spectrum analyzer (OSA) and an electrochemical impedance spectroscope (EIS), respectively. Test results indicated that the Fe-C coated LPFG sensor can be applied to successfully monitor the onset of corrosion along the length of steel rebar. In practical applications, the change in wavelength of the LPFG sensor is first measured with the OSA and then converted to the degree of corrosion in iron coating through their calibrated relation. For long-term monitoring, LPFG sensors may be coated with a thin layer of stainless steel that can be corroded slowly over time.

3.2. EXPERIMENTAL PROCEDURE

All optical fibers tested in this study were cleansed for 10 min with 20% NaOH solution to remove oil on their surface, further cleansed for 3 min with distilled water using an ultrasonic cleaner, and dried for 5 min at 100℃ in an oven. The clean LPFG sensors were fixed on a copper frame to make sure that the grating part is straight and away from the fixed points. The prepared specimens were finally put into the Discovery-18 Deposition System and deposited with silver for 90 sec to a thickness of around 500 nm. After that, the surface of the LPFG sensors became conductive. The Fe-C film was electroplated onto the metalized optical fiber with an electroplating solution [67]. The composition of the electroplating solution and the operation parameters of the electroplating process are listed in Table 3.1. The mass ratio of Fe to C in the solution is

close to that of the reinforcement steel. The electroplating process lasted for 2 hours. Figure3.1 shows a schematic view of the structure of a Fe-C coated LPFG.

Table 3.1. Bath composition and electroplating conditions [67]

FeSO$_4$·7H$_2$O (g/L)	Citric Acid (g/L)	L-ascorbic acid (g/L)	pH	I (mA/cm^2)	Temperature
40	1.2	3.0	2.5	4.6	25°C
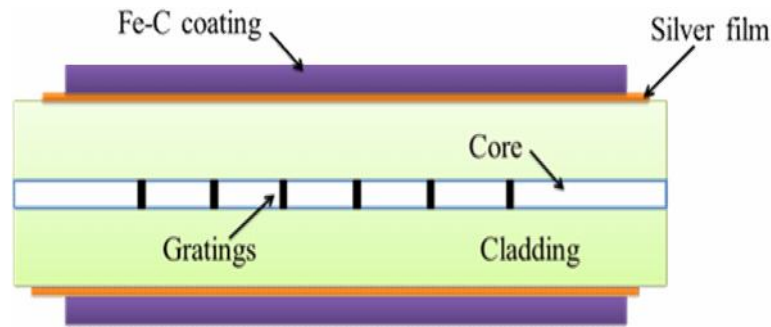
Figure 3.1. Schematic view of the structure of a Fe-C coated LPFG.

One LPFG sensor coated with a Fe-C film was bandaged on a #5 steel bar (d = 0.625 in) and then put in a glass beaker filled with 3.5 wt. % NaCl solution, which was prepared by dissolving purified sodium chlorides (Fisher Scientific) into distilled water. The corrosion area is 20 cm^2. The EIS measurements were taken with a typical three-electrode test setup, as shown in Figure 3.2(a), consisting of a 25.4 mm × 25.4 mm × 0.254 mm platinum sheet as a counter electrode, a saturated calomel electrode (SCE) as a reference electrode, and a Fe-C coated optical fiber as a working electrode. These electrodes were connected to a Gamry, Reference 600 potentiostat/galvanostat/ZRA for data acquisition. EIS measurements were taken at 5 points per decade with a sinusoidal potential of 10 mV applied around the open-circuit potential with a frequency range of 5 mHz to 100 kHz.

The LPFG sensor was fixed on a steel bar to ensure it was straight and demonstrate a deployment scheme, as shown in Figure 3.2(b). It is then connected to the laser (HP 83437A) and an optical spectrum analyzer (OSA, Yokogawa AQ6370C). The light transmissions of the sensor at various wavelengths were taken and recorded every 12 min. The recorded transmission spectra were curve fitted to extract the resonant

wavelength data. The overall test setup with the OSA and the specimen is shown in Figure 3.2(a). As shown in Figure 3.2(b), Kapton tape was adopted to separate the LPFG from the steel and thus eliminate the potential influence of the corrosion process of Fe-C coating on the EIS measurement of the steel bar.
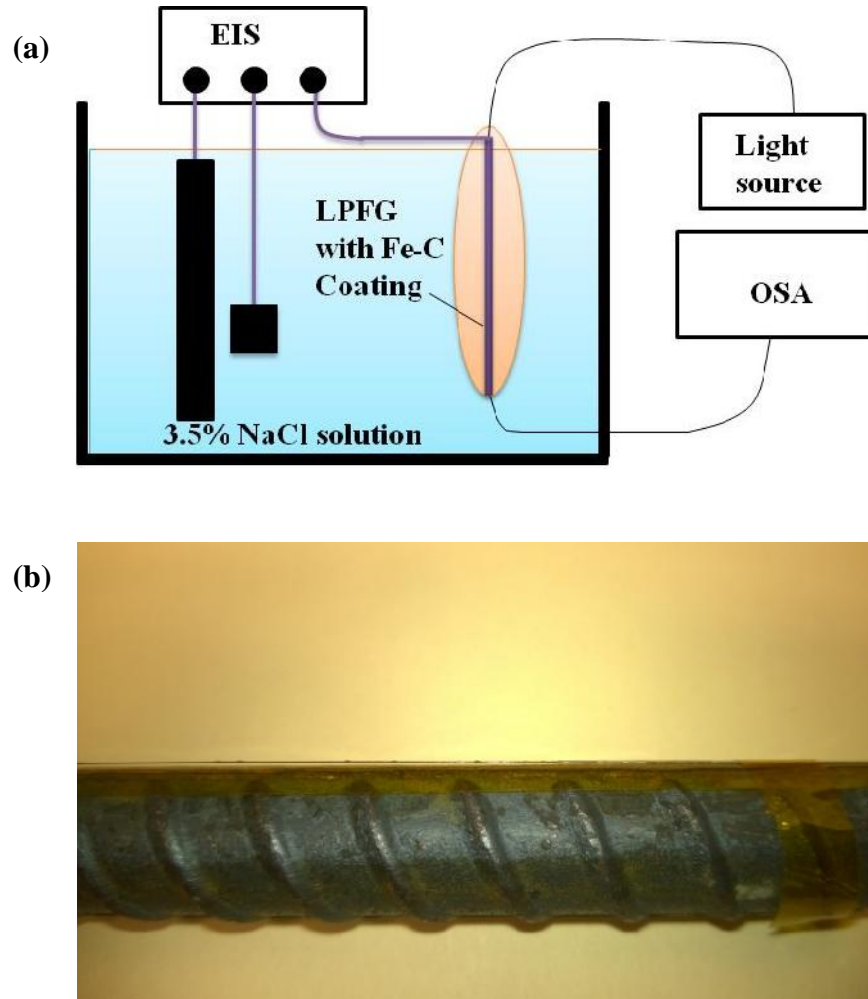
Figure 3.2. Corrosion test of a Fe-C coated LPFG: (a) test setup and (b) Fe-C coated LPFG and #5 steel.

3.3. EXPERIMENTAL PROCEDURE AND RESULTS

Figures 3.3(a)-3.3(c) show the SEM surface morphologies of a Ag coated fiber, a Fe-C coated fiber prior to corrosion test, and the Fe-C coated fiber after 24 hours of corrosion test, respectively. It can be seen from Figure 3.3(a) that small silver grains with 500 nm in size can be seen on the surface of the Ag coated optical fiber. Figure 3.3(b)

shows the Fe-C coated optical fiber prior to corrosion tests. The diameter of the optical fiber increased from 125 µm (bare fiber) to 145.8 µm; the Fe-C film was thus approximately 10.4 µm thick. However, the Fe-C film was full of micro cracks as observed in Figure 3.3(b-2). After 24 hours of corrosion test, corrosion products accumulated on the surface of the LPFG sensor with its diameter increased to 400 µm.
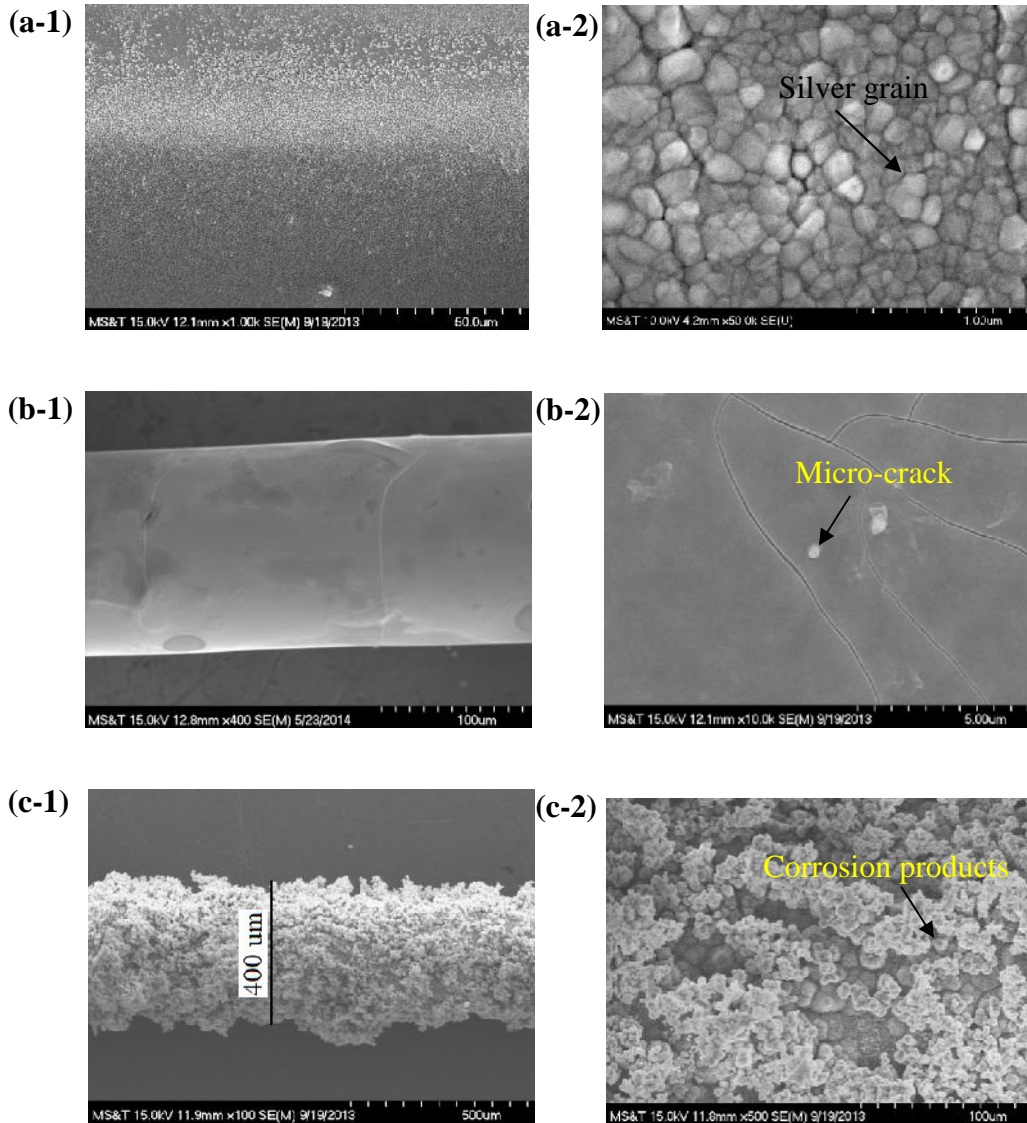
Figure 3.3. SEM images of (a) Ag coated LPFG, (b) Fe-C coated LPFG prior to corrosion test, and (c) Fe-C coated LPFG after 24 hours of corrosion test.

The Changing of Resonant Wavelength and Time is shown in Figure3.4(a), (b) and (c); The average changing of resonant wavelength is shown in Figure 3.4(d). From

Figure 3.4, the resonant wavelength monotone decreased from 0 to 8hours and the decrease speed was more and more slowly. After 8 hours, the resonant wavelength had no experiences on monotone decrease or increase.
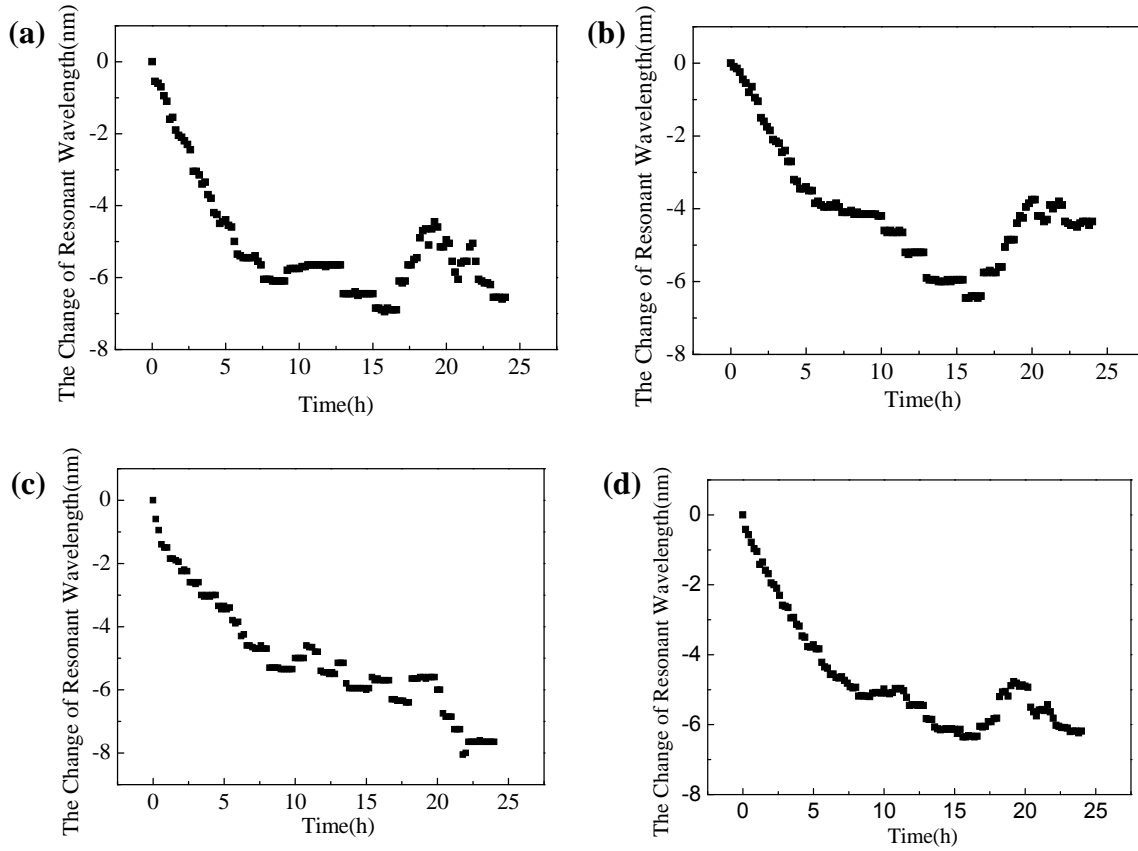
Figure 3.4. The change of resonant wavelength over time for (a) Specimen 1, (b) Specimen 2, (c) Specimen 3, and (d) all specimens (average change).

Figure 3.5(a) shows the OCP data for the three specimens tested. Their corresponding EIS test results are presented in Figure 3.5(b-d). Based on the EIS results, the average corrosion rate and the mass loss rate were calculated from the Faraday's Law and presented in Figure 3.6. In these calculations, the corrosion area was taken to be 20 cm^2. That is, the mass loss rate in gram per hour is equal to 249 (gram) $\times$ I (mA/m^2/day) $\times$ 20 (cm^2) $\times$ (1 m^2/10000 cm^2) $\times$ (1 day/24 hour) and the mass loss in gram is 249$\times$I$\times$(20/10000)$\times$(1/24)t, where I represents the average corrosion rate in mA/m^2/day and t denotes the immersion time in hour. The average mass loss rate, presented in Figure 3.6(b), can be integrated over time to obtain the accumulated mass loss up to different

time as shown in Figure 3.7(a). By correlating Figure 3.7(a) with Figure 3.4(d), the relationship between the change in resonant wavelength and the mass loss at any time can be established and presented in Figure 3.7 (b).
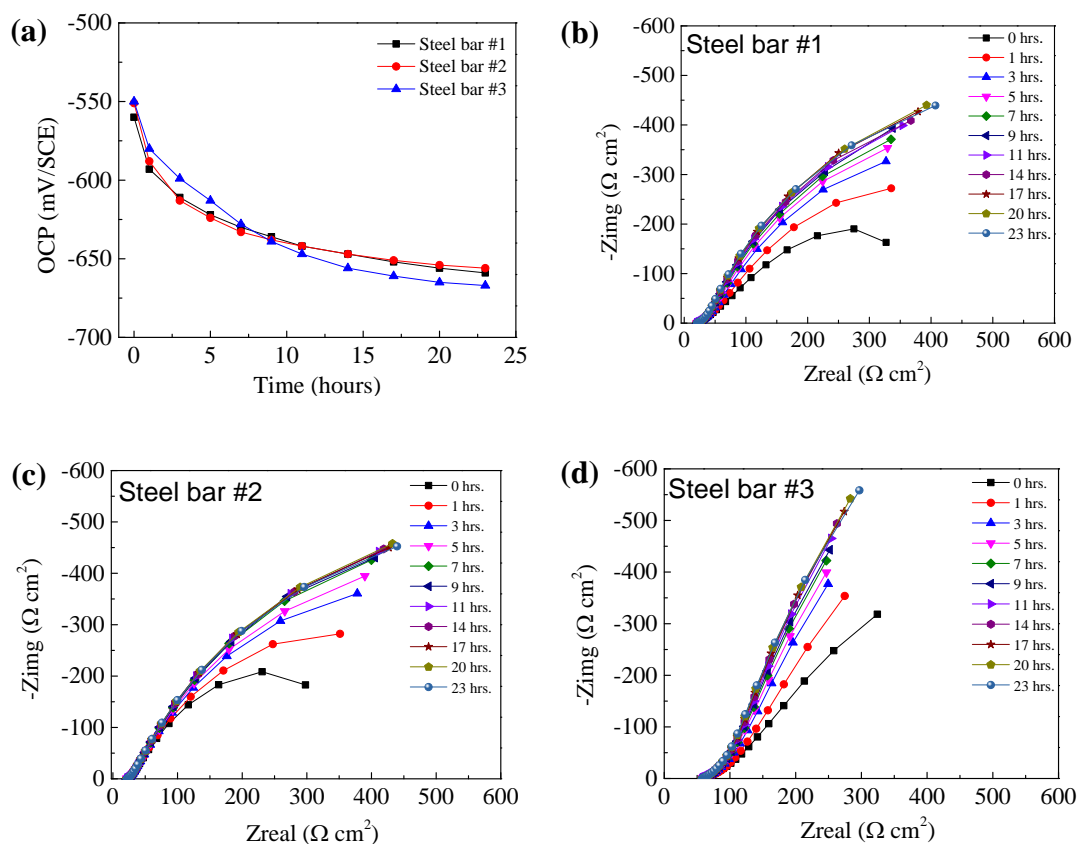
Figure 3.5. The OCP and EIS test results for three steel bars.
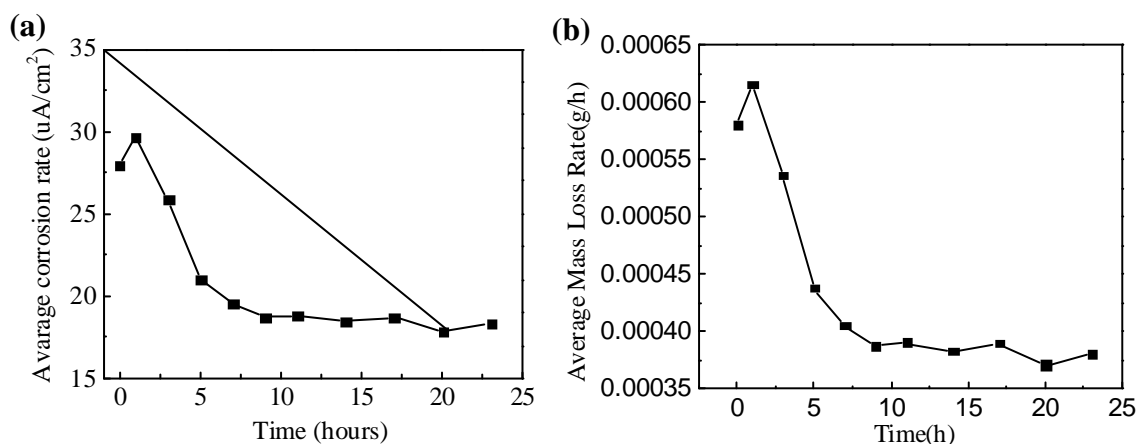
Figure 3.6. The relationship between (a) average corrosion rate and time; (b) average mass loss rate and time.
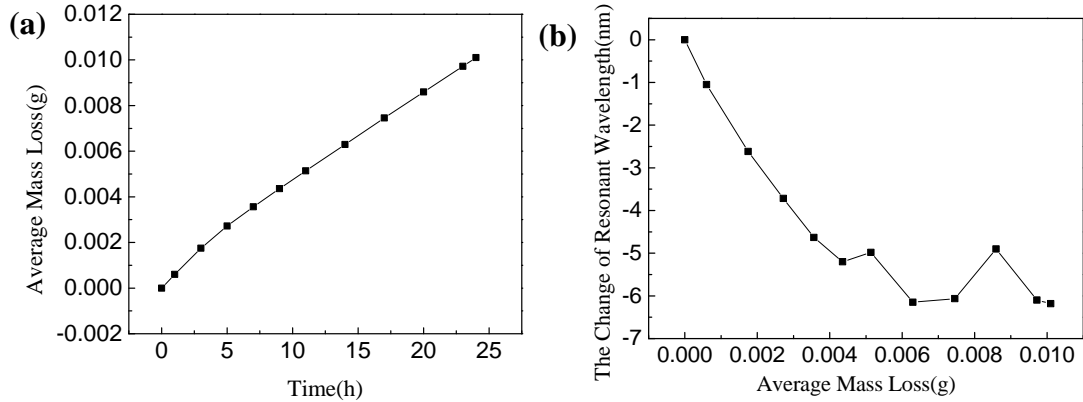
Figure 3.7. The relationship between (a)average mass loss and time; (b)average resonant wavelength change and mass loss.

It can be seen from Figure 3.7(b) that the relationship between the change in resonant wavelength and the average mass loss is nearly linear when the average mass loss is less than 0.004. In this range, a linear regression line $= -1300 \; M$ can be developed with a coefficient of determination $R^2=0.98$. Here, M (g) represents the average mass loss and (nm) denotes the change in resonant wavelength. When the average mass loss is greater than 0.004, the change in resonant wavelength fluctuates over time and thus no obvious relationship between them can be developed with high confidence. Since the Fe-C coating is quite thin, the total corrosion time is only 24 hours. The linear regression line for monotonic decrease of the change in resonant wavelength is valid for the first 8 hours only. Therefore, the corrosion sensor is applicable for early corrosion monitoring with high sensitivity. Thicker Fe-C coating can be used to increase the time of corrosion or stainless steel coating can be applied to the surface of an LPFG to delay the corrosion process at a reduced corrosion rate.

3.4. CONCLUSIONS

In this study, the Fe-C coated LPFG corrosion sensor was attached on a steel bar. Both were immersed in the NaCl solution over time in order to correlate the corrosion processes of the Fe-C and steel bar to each other. This approach can be applied for accurate corrosion monitoring based on the variation in ambient refractive index of the LPFG caused by the corrosion process of the Fe-C coating on the LPFG. The following conclusions can be drawn on the basis of the tests and analysis:

(1) Due to the change in ambient refractive index in corrosive environment, a Fe-C coated LPFG sensor can be used to accurately and sensitively monitor the corrosion of the Fe-C material and thus the early-age corrosion of a nearby steel bar based on the change in resonant wavelength of the LPFG sensor. Longer-duration corrosion may be achieved by increasing the thickness of Fe-C coating or using corrosion retard metals such as stainless steel coating.

(2) In the 3.5wt. % NaCl solution, the resonant wavelength decreases linearly with time within the first 8 hours and shows no clear trend after 8 hours of immersion. For the linear portion, the change in resonant wavelength   (nm) can be strongly related to time t (h) by   = -0.625t with a coefficient of determination of 0.97.

(3) The mass loss follows the similar trend over time as the resonant wavelength. In the first 8 hours, the relationship between the mass loss M (g) and time t (h) can be strongly represented by $M = 0.00048t$ with a coefficient of determination of 0.99.

(4) The change in resonant wavelength   (nm) and the mass loss M (g) can be closely correlated by   = -1300 M in the first 8 hours of tests. The sensitivity of the Fe-C coated LPFG sensor is high and sufficient in engineering applications.

4. CORROSION MONITORING OF STEEL BARS IN MORTAR USING Fe-C COATED LONG PERIOD FIBER GRATINGS

4.1. INTRODUCTION

In this study, the corrosion process of steel bars embedded in mortar cylinder and immersed in 3.5 wt. % NaCl solution was monitored with long period fiber grating (LPFG) sensors. Each LPFG was first deposited with a thin layer of silver (600 nm or 1000 nm thick) and then electroplated with a thick layer of Fe-C film (6 um or 10 um thick). The coated LPFGs were attached to the surface of a steel bar that is then embedded in mortar cylinder. Twelve mortar cylinders were cast, cured for 28 days, and tested in 3.5 wt. % NaCl solution for 105 days. The corrosion evolution of steel bars in mortar cylinder was monitored with electrochemical impedance spectroscopy (EIS). The wavelength change of the corresponding LPFGs was measured with an optical spectrum analyzer (OSA). Results showed that the effects of both silver and Fe-C film thickness on the change of resonant wavelength were insignificant in the test range. The wavelength of a coated LPFG sensor was first observed to drop suddenly in the first 7 days due to penetration of NaCl solution through mortar cover and the Fe-C and silver layers, corresponding to a passive state of the steel bar. The slow increase over time after 7 days was due to the initiation of corrosion and buildup of corrosion products. A linear relationship was observed between the corrosion mass loss and the increase of resonant wavelength, indicating Fe-C coated LPFG sensors can effectively monitor the corrosion evolution of steel in mortar.

4.2. EXPERIMENTAL PROCEDURE

Single-mode optical fiber (Coring, SMF-28e) with core and cladding diameters of 8.2 µm and 125 µm, respectively, were used in this study. The refractive index of core and cladding are 1.4691 and 1.4628, respectively. Each optical fiber was cleansed with 20% NaOH solution for 10 minutes to get rid of oil on the surface, and then cleansed with distilled water for 3 minutes using an ultrasonic cleaner, and dried in an oven at 100 °C for 5 minutes.

Since the optical fiber is not conductive, a thin layer of silver was deposited on the surface of the fiber prior to electroplating of the Fe-C layer. To ensure that the fiber

was straight and the coating had a consistent thickness, all the cleaned optical fibers were fixed on a copper frame before they were moved and placed inside the Discovery-18 Deposition System. Two thicknesses of silver layer were considered, 600 nm and 1000 nm, corresponding to a deposition time of 1.5 and 2.5 minutes, respectively.

After silver coating, a layer of Fe-C was electroplated directly on the silver film. The composition of the electroplating solution and the operation parameters of the electroplating process are listed in Table 4.1. The mixture of this solution is intended to produce a Fe-C layer with the same mass ratio of Fe to C as that in steel reinforcement bars. For the electroplating process, the silver coated optical fiber was connected with the negative end of an external power supply with a constant current of 5 mA. The positive end of the power supply was connected with a graphite rod. To protect the fiber from mechanical damage and have a good electrical connection, a conductive rubber was placed between an alligator clip and the optical fiber. The electroplating process lasted for 1.5 and 2.0 hours to produce different thicknesses. Therefore, four conditions were considered including two silver thicknesses and two Fe-C film thicknesses as listed in Table 4.2. To ensure the repeatability of test results, three specimens were prepared for each condition. Therefore, a total of 12 specimens were prepared and tested in this study. Both the average (Avg.) and the coefficient of variation (COV) of the silver and Fe-C layer thickness are given in Table 2. The microstructure of Fe-C coated optical fiber is schematically shown in Figure 4.1.

To have a better understanding about the surface microstructure after silver deposition and Fe-C electroplating, two additional small pieces of fibers after silver deposition and electroplating were prepared and observed using a scanning electron microscopy (SEM S4700, Hitachi, Kyoto, Japan).

Table 4.1. Bath composition and electroplating conditions [67]

$FeSO_4 \cdot 7H_2O$ (g/L)	Citric Acid (g/L)	L-ascorbic acid (g/L)	pH	I (mA/cm^2)	Temperature
40	1.2	3.0	2.5	6	25°C

Table 4.2. Deposition and electroplating time of specimens

Specimens	Silver layer			Fe-C layer		
	Deposition Time (minutes)	Thickness Avg. (nm)	COV	Electroplating Time (hours)	Thickness Avg. (µm)	COV
#1 - #3	1.5	650	0.13	1.5	6.1	0.08
#4 - #6	1.5	650	0.13	2.0	10.5	0.12
#7 - #9	2.5	1100	0.15	1.5	6.0	0.10
#10 - #12	2.5	1100	0.15	2.0	9.8	0.15
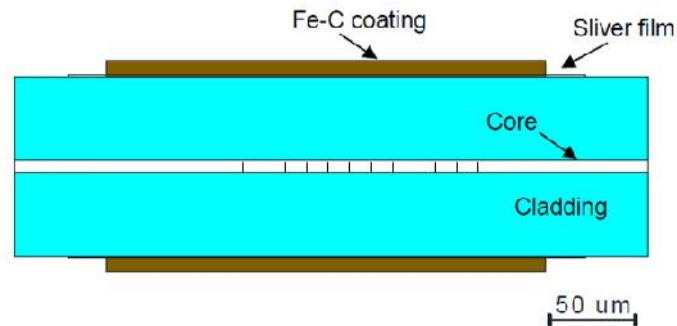
Figure 4.1. Schematic illustration of the structure of a Fe-C coated LPFG.

Any variation in surface condition of the optical fiber can alter the resonant wavelength of the LPFG sensor. Therefore, the change of resonant wavelength after each process was measured with an optical spectrum analyzer (OSA, Yokogawa AQ6370C). The measured results are presented in Table 4.3.

Table 4.3. Resonant wavelength of four representative specimens under different conditions

Specimens	Coating Thickness		Resonant Wavelength		
	Silver (nm)	Fe-C (um)	Initial (nm)	After Coating (nm)	After Casting in Mortar (nm)
#3	650	5.8	1529.9	1562.7	1550.7
#6	650	10.2	1535.1	1569.9	1557.3
#7	1100	6.5	1544.3	1576.8	1564.7
#12	1100	9.6	1547.2	1572.0	1559.7

After electroplating, the Fe-C coated LPFGs were attached to the surface of steel bars. The steel bars used in this study were ASTM A615 Grade 60 #3 steel bars with a diameter of 9.50 mm (0.38 in), and its chemical composition is shown in Table 4.4. To

avoid interference of steel bar, an insulating adhesive strip was attached between the Fe-C coated LPFG and the steel bar surface. A copper wire was welded on one end of the steel bar for corrosion test as shown in Figure 4.2. To limit the corrosion occurred in the middle portion of steel bar, the exposed steel bar out of mortar cylinder was coated with a layer of epoxy.

Table 4.4. Chemical composition of steel bar

Element	C	Si	Mn	P	S	Cr	Mo	Ni	Co	Cu	V	Sn	Fe
wt. %	0.43	0.22	0.95	0.15	0.07	0.17	0.03	0.10	0.01	0.46	0.02	0.02	97.37

The mortar was prepared using cement, tap water, and sand with a weight ratio of 1:0.5:1. The cement was Portland Type and its chemical composition was determined and listed in Table 4.5. The Missouri River sand was used with the maximum diameter of 500 um. All the steel bars were cut to a length of 80 mm (3.15 in). Before mortar casting, all the mill scale on the steel bar surface was cleansed following the ASTM standard [79].

Table 4.5. Chemical composition of type-I Portland cement (wt. %)

Loss on ignition	SiO_2	Al_2O_3	CaO	MgO	SO_3	Na_2O	K_2O	Cl	TiO_2	Fe_2O_3	P_2O_5	Total
3.98	19.48	6.80	55.35	3.32	4.35	2.39	1.00	0.02	0.20	2.18	0.19	99.27

For the casting of mortar, a PVC pipe with a diameter of 20 mm (0.79 in) was used as a mold. To ensure the steel bar placed along the centerline of the mortar cylinder, a groove was firstly precut in a piece of plywood to fix the PVC pipe, and then a hole with a diameter of 13 mm (0.50 in) was drilled at the location of steel bar. Figure 4.2(a) shows the dimensions of the steel bar and the mortar cylinder. The mortar cover is 5.2 mm (0.20 in) thick, and the length of the bar exposed to the corrosive environment is 103 mm (4.10 in) with an exposure surface area of 30 cm^2 (4.65 in^2). After 24 hours, the mortar cylinders were de-molded from the PVC pipe and cured in a curing room at 20 °C temperature and 100% humidity for 28 days before corrosion tests. Figure 4.2(b) shows one mortar specimen ready for corrosion test after curing. A total of 12 mortar specimens were prepared and tested with two silver layer thicknesses, two Fe-C layer thicknesses, and three identical specimens prepared for each condition.
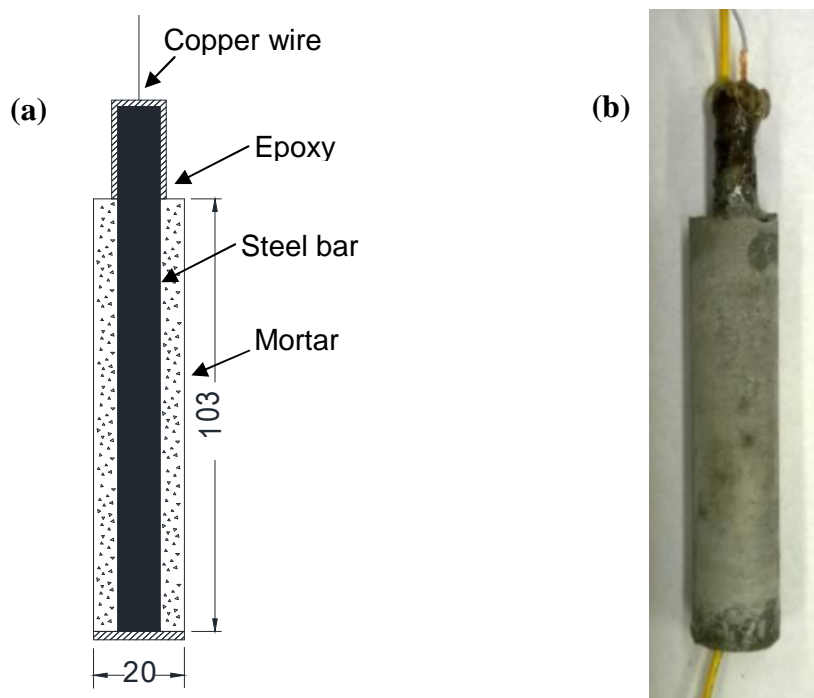
Figure 4.2. Design of test specimen: (a) schematic view with dimensions, and (b) finished mortar cylinder. (unit: mm, 1 mm=0.04 in.).

After curing for 28 days, all mortar specimens were placed in a container filled with 3.5 wt. % NaCl solution, which was prepared by dissolving purified sodium chloride into distilled water. The corrosion tests lasted for 105 days, and electrochemical impedance spectroscopy (EIS) was conducted to monitor the evolution of corrosion over time. As schematically shown in Figure 4.3, EIS was conducted with a typical three-electrode setup that consists of a 25.4 mm (1.0 in) × 25.4 mm (1.0 in) × 0.254 mm (0.01 in) platinum sheet as a counter electrode, a saturated calomel electrode (SCE) as a reference electrode, and a steel bar as a working electrode. These electrodes were connected to a Gamry, Reference 600 potentiostat/galvanostat/ZRA for data acquisition. EIS measurements were taken at 5 points per decade when a sinusoidal potential of 10 mV with a frequency range 5 mHz to 100 kHz was applied around the open-circuit potential. The change in resonant wavelength of optical fibers was also measured using the OSA after each corrosion test.
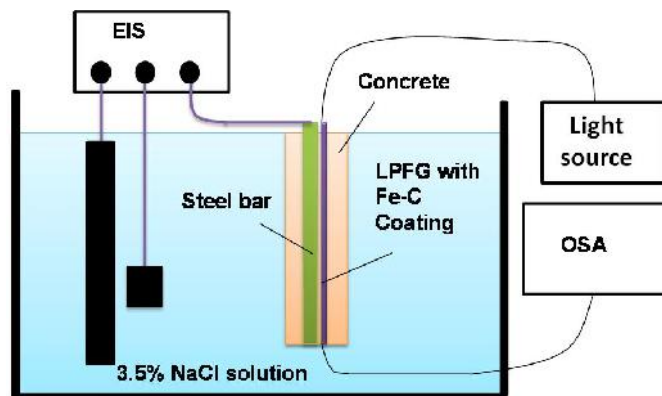
Figure 4.3. Optical and electrochemical measurements.

4.3. TEST RESULTS AND DISCUSSION

In this section, the spectrum of three LPFGs over time was measured by an optical spectrum analyzer (OSA, Yokagawa AQ6370C) and the resonant wavelength at different time was obtained through curve fitting. The spectrum and EIS results of steel bar were measured simultaneously to establish the relationship between the resonant wavelength of LPFG and the corrosion mass of steel bar.

4.3.1. Changes of Resonant Wavelength. Figures 4.4(a-1) to 4.4(d-1) show the transmission spectra of various Fe-C coated LPFG sensors measured at different times and under different coating conditions. Figures 4.4(a-2) to 4.4(d-2) show the changes of the resonant wavelength as a function of corrosion test time for various specimens. The resonant wavelength was obtained by curve fitting of the transmission spectrum. All Fe-C coated LPFGs tested in this study showed the same trend over time. Therefore, only the results of four specimens were demonstrated. The resonant wavelength decreased suddenly in the first 7 days of corrosion test, and then increased slowly till 105 days. The sudden drop of resonant wavelength was attributed to the penetration of NaCl solution through mortar cover and Fe-C film into silver deposition layer. The silver deposition layer is porous as observed in Figure 4.4(a-2). The arrival of NaCl solution at the cladding surface changed the refractive index of the interface and resulted in the change of resonant wavelength. The increase of resonant wavelength over time after 7 days was attributed to corrosion initiation and generation of corrosion products due to the breakdown of passive film.
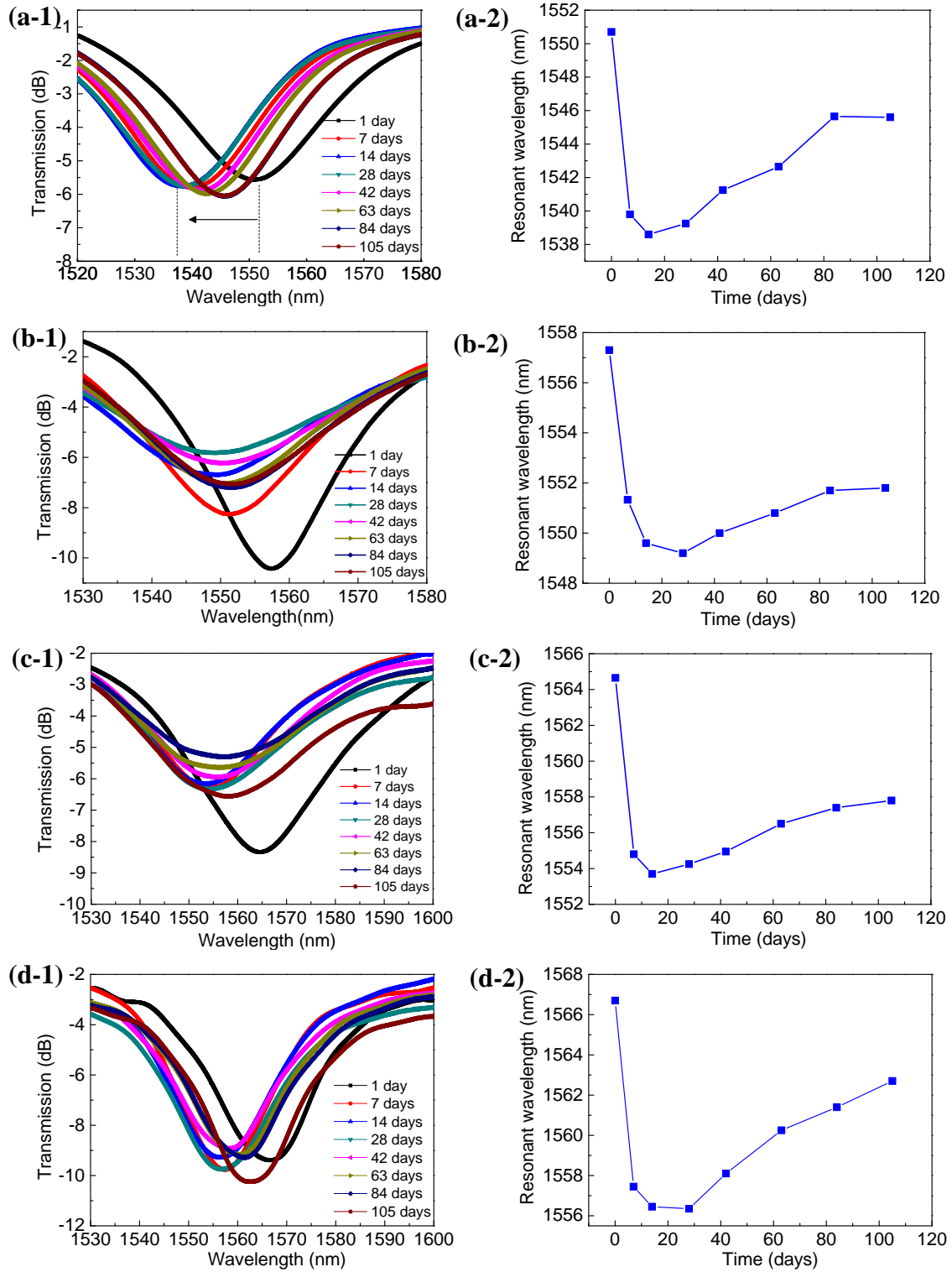
Figure 4.4. (1) Transmission spectra, and (2) resonant wavelength over time for: (a) specimen #3, (b) specimen #6, (c) specimen #7, and (d) specimen #12.

4.3.2. Changes of Corrosion Properties over Time. All twelve mortar cylinder specimens showed similar EIS results. Therefore, only the results of four representative specimens were presented in Figure 4.5. Two depressed semi-circles were observed from the Nyquist plots. The large semi-circle is related to the dielectric properties of electrolyte-steel interface: charge transfer resistance and double layer capacitance. The small semi-circle (shown in inserts) is associated with the mortar cover properties: mortar resistance and mortar capacitance. The phenomena can also be reflected by the two time constants displayed in the phase angle-frequency plots. The first time constant in the frequency higher than 10 Hz corresponds to the electrolyte-steel interface, and the second time constant in the frequency range lower than 10 Hz corresponds to the mortar properties.
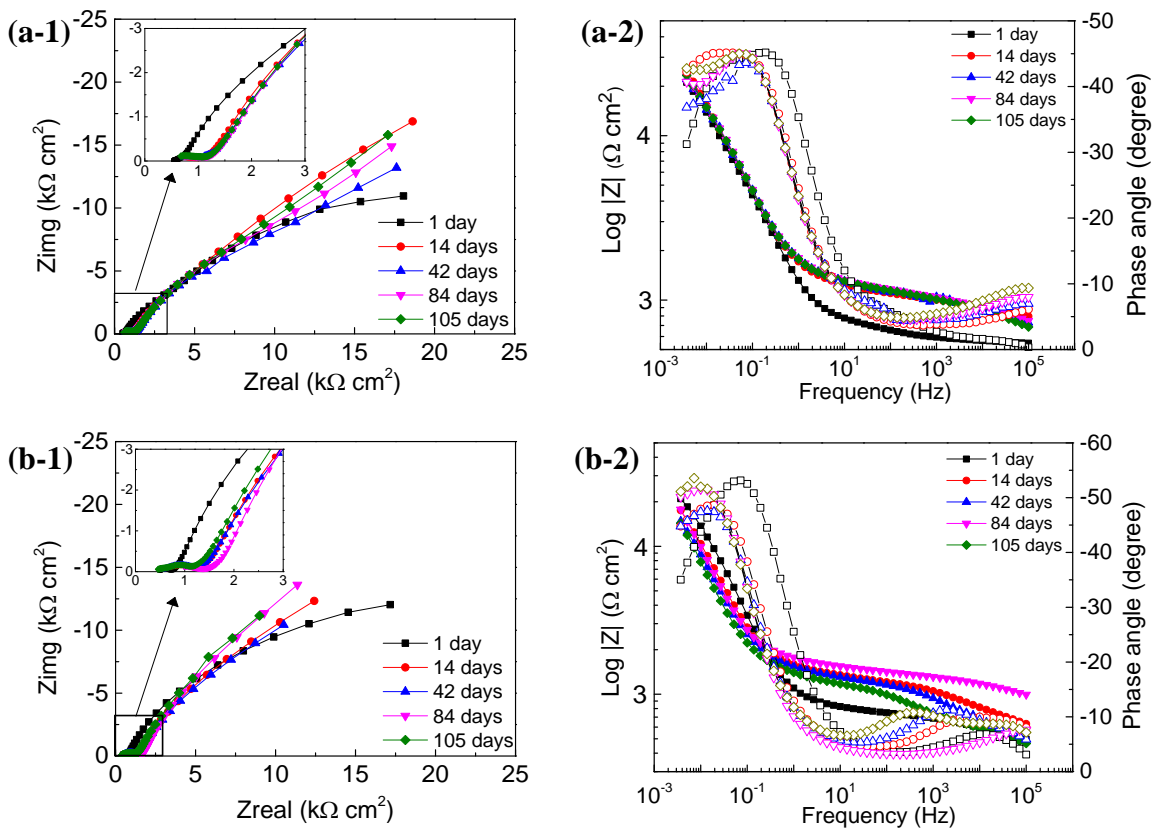
Figure 4.5. Representative EIS results in terms of (1) Nyquist plots, and (2) Bode plots for: (a) specimen #3, (b) specimen #6, (c) specimen #7, and (d) specimen #12.
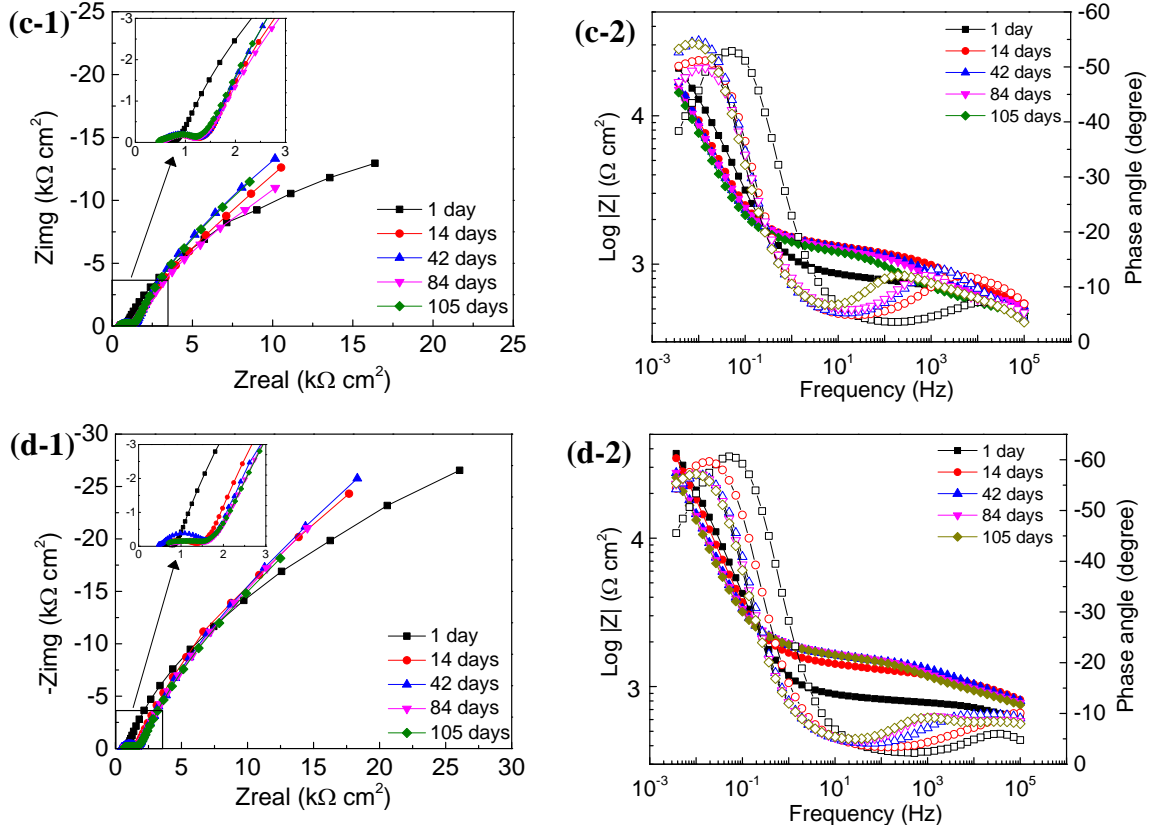
Figure 4.5. Representative EIS results in terms of (1) Nyquist plots, and (2) Bode plots for: (a) specimen #3, (b) specimen #6, (c) specimen #7, and (d) specimen #12. (cont.)

Equivalent electrical circuit (EEC) is usually used to fit the EIS results. In this study, one EEC model was proposed based on the characteristics of impedance spectrum as shown in Figure 4.6. This model was also used by other researchers to study stainless steel corrosion in activated fly ash concrete [125]. In the EEC model, R_s represent the pore solution resistance inside the mortar cover, R_m and CPE_m represent the resistance and capacitance of mortar cover, R_{ct} and CPE_{dl} represent the charge transfer resistance and double layer capacitance at the electrolyte-steel interface. The constant phase element (CPE) instead of capacitance was used to take into account the effect of non-homogeneity. The non-homogeneity mainly comes from the irregularities on the steel surface, surface roughness, and certain processes associated with the irregular distribution of the applied potential [126]. The CPE is defined by two parameters Y and n, and its admittance representation is:

$$Y_{CPE} = Y(j\check{S})^n \qquad\qquad (4.1)$$

where Y is a parameter directly proportional to the capacitance of pure capacitive electrode,   is the angular frequency in rad/sec, and n represents the deviated degree of the capacitance of the electrode form the ideal condition of a pure capacitor.
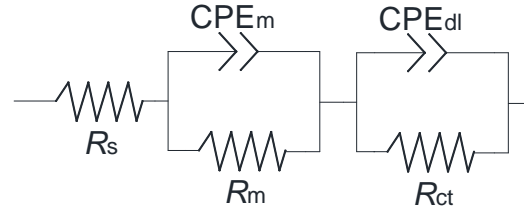
Figure 4.6. Equivalent electrical circuit for mortar cylinders.

Figure 4.7 shows the evolution of mortar pore solution resistance over time for four representative specimens in Figure 4.5. The pore solution resistance is related to the microstructure of mortar cylinder, which depends on the water cement ratio and electrolyte inside the pores. Therefore, no effect of the Fe-C coated LPFG sensors on the solution resistance was observed. The average mortar pore solution resistance is approximately 460   cm2.
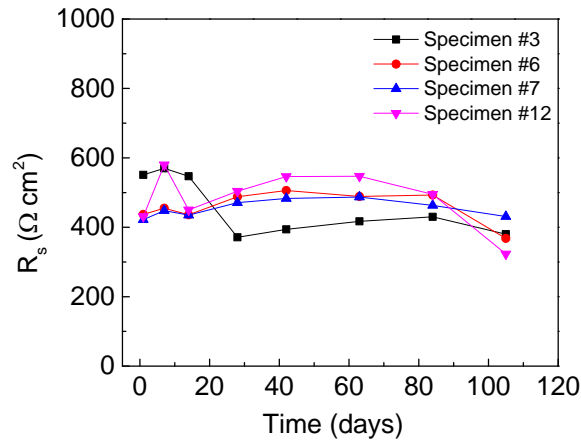
Figure 4.7. Change of pore solution resistance over time.

Figure 4.8 shows the evolution of mortar cover properties and electrolyte-steel interfacial properties over time in terms of resistance and capacitance. There is no general trend observed within the test period since corrosion is a slow process and an immersion of 105 days in 3.5 wt. % NaCl solution is not long enough to display notable differences.

The average mortar cover resistance is 930 Ω cm^2, and the average mortar cover capacitance is 3.0×10^{-8} F/cm^2. Similar to mortar properties, there is also no trend observed for the charge transfer resistance and double layer capacitance over time. The average charge transfer resistance is around 64 kΩ cm^2, and the average double layer capacitance is 5.7×10^{-4} F/cm^2.
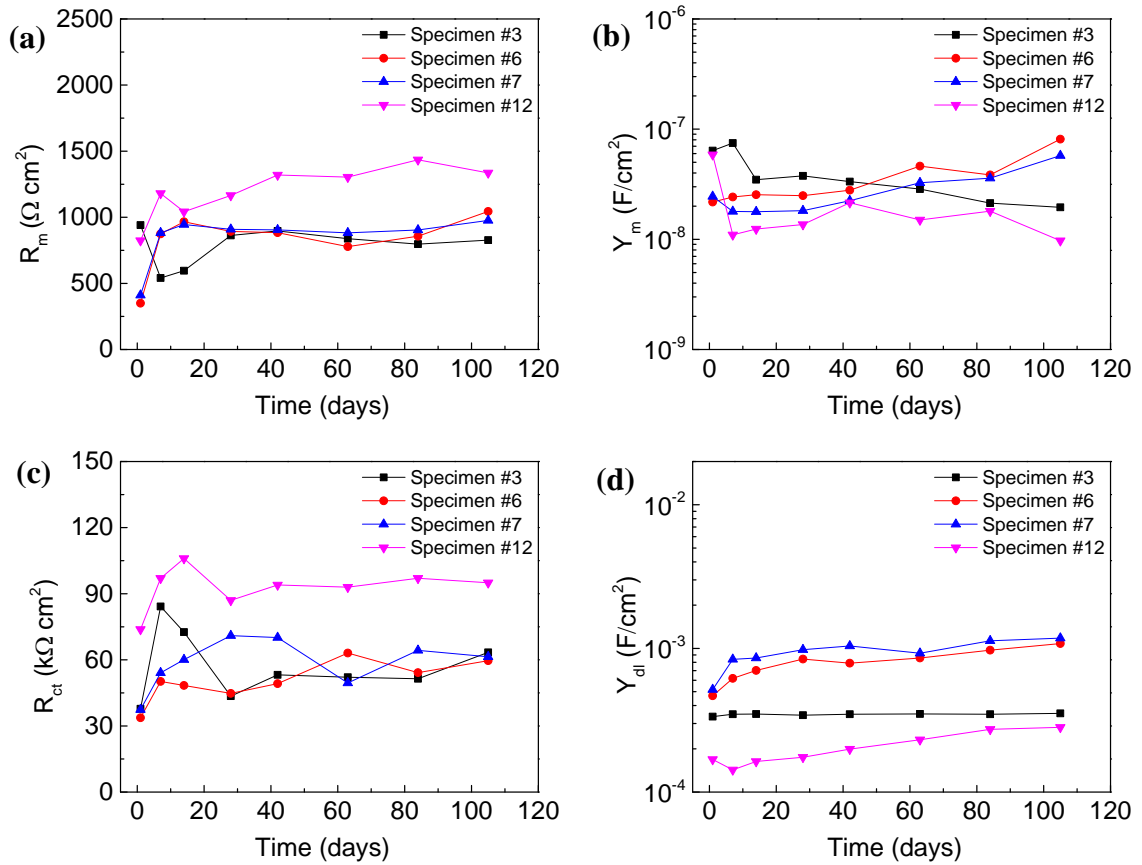
Figure 4.8. Change of corrosion properties over time: (a) mortar resistance, (b) mortar capacitance, (c) charge transfer resistance, and (d) double layer capacitance.

Charge transfer resistance is inversely proportional to the corrosion rate that was calculated based on the following equation [124]:

$$i = \frac{B}{R_{ct}} \tag{4.2}$$

where i is the corrosion rate, R_{ct} is the charge transfer resistance from EIS results, B is a constant related to the Tafle slopes of a polarization curve. A value of B=26 mV was used

in this study. The corrosion mass loss of steel bars over time was calculated based on the corrosion rate, the steel bar surface, and time.

4.3.3. Relationship Between Wavelength Change and Mass Loss. Figure 4.9 shows the change of resonant wavelength as a function of the corrosion mass loss of steel bar embedded in a mortar cylinder. A general trend could be observed. The resonant wavelength displayed a sudden drop in the first 7 days, which was attributed to the penetration of NaCl solution inside the Fe-C coating and silver deposition layer and resulted in a change of refractive index at the cladding and solution interface. After 7 days, the resonant wavelength increased slowly with an increase of corrosion mass loss. A linear regression analysis was performed and the linear equations for each representative specimen and their adjusted R^2 values were shown in Figure 4.9. In comparison with nano iron/silicate particle coating [24], the Fe-C coated LPFG sensor is more sensitive and can thus be used to monitor the corrosion mass loss of steel bar in mortar. Overall, the R^2 is high, indicating a strong correlation between the wavelength change and mass loss.
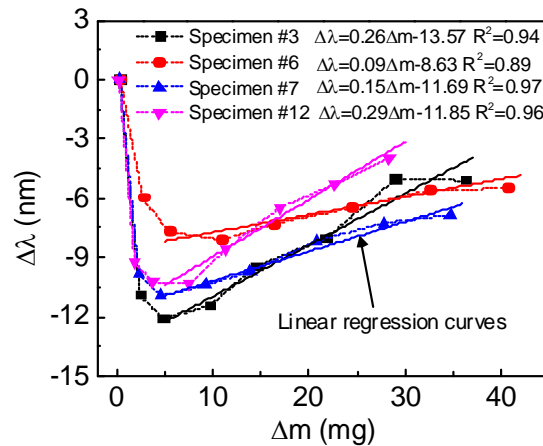
Figure 4.9. Change of resonant wavelength as a function of corrosion-induced mass loss of steel bars.

After 105 days of corrosion test, all mortar cylinders were taken out of glass beakers and dried at room temperature for 3 days. A small steel hammer was then used to break down the mortar specimens for visual observation. Figure 4.10 shows the surface condition of the retrieved steel bars after 105 days of corrosion test. It can be observed from Figure 4.10(a) that pitting corrosion occurred on the surface. The surface of the Fe-

C coated optical fiber showed some rusts and a part of the white silver layer was completely exposed due to dissolution of the Fe-C film.
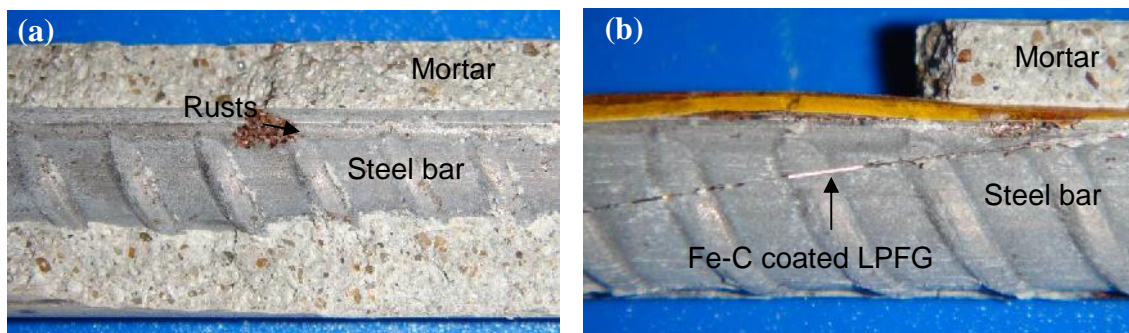
Figure 4.10. Surface conditions after 105 days of corrosion test: (a) corrosion pit and (b) Fe-C coated LPFG sensor.

4.4. CONCLUSIONS

In this study, an LPFG corrosion sensor was developed and its application to monitor the corrosion of steel bars embedded in mortar cylinder was investigated. The optical fiber corrosion sensor was fabricated by depositing an inner thin silver layer and then electroplating an outer thick Fe-C layer. Two silver film thicknesses and two Fe-C coating thicknesses were considered. The fabricated Fe-C coated optical fiber sensor was attached to the surface of a steel bar and then embedded in mortar cylinder, which was subjected to corrosion test in 3.5 wt. % NaCl solution for 105 days. The evolution of steel bar corrosion over time was monitored with EIS. Based on the test results and discussion, the following conclusions can be drawn:

(1) Effect of both silver and Fe-C film thickness on the change of resonant wavelength is insignificant in the test range. This is because both silver and Fe-C films are very thin and permeable, and NaCl solution can penetrate through them to arrive at the cladding surface rapidly.

(2) Two stages of resonant wavelength change were observed: a sudden drop in the first 7 days of immersion in salt solution, and a slow increase due to corrosion initiation and loss of Fe-C film. The sudden drop was attributed to the penetration of NaCl solution through mortar cover and coating layers, a stage that the steel bar was in passive state. The slow increase was attributed to corrosion initiation and the generation of corrosion products, a stage that the steel bar was in active state.

(3) A linear relationship was observed between the change of resonant wavelength of a Fe-C coated LPFG and the corrosion mass loss of a steel bar embedded in mortar cylinder immersed in 3.5 wt. % NaCl solution for 105 days. Therefore, Fe-C coated LPFG sensors can effectively monitor the corrosion evolution of steel bars in mortar.

5. MONITORING OF CORROSION IN STEEL TUBES BASED ON THE LIGHT REFLECTION AT THE FLAT END OF OPTICAL PROBES

5.1. INTRODUCTION

Many methods have been developed for corrosion monitoring of metals or alloys such as electrical resistance (ER) probe, field signature method (FSM), ultrasonic thickness measurement (UTM), acoustic emission (AE), and electrochemistry-based methods. Each method, however, has its advantages and limitations. Most of the monitoring techniques are useful for corrosion monitoring of pipeline steel or stainless steel. They have limitations for corrosion monitoring of steel bars in reinforced concrete (RC) structures. In this study, a corrosion threshold-based, optical probe (OP) is proposed for the long-term monitoring of pitting corrosion in steel bars. Its principle and performance are validated experimentally.

5.2. WORKING PRINCIPLE OF OPTICAL PROBES

An OP is simply a commercial optical fiber ended and encapsulated in a steel tube that is made of the same material as steel rebar to be monitored. The end of the fiber is a flat surface acting like a mirror, reflecting light efficiently. Once in contact with water that could penetrate through a completely-corroded wall of the steel tube in moisture or wet environment, the flat surface changes its light reflection intensity. Therefore, the light reflection intensity can be related to the wall thickness of the steel tube and used to monitor the onset of a certain corrosion level in the steel tube or a nearby steel rebar. The thickness of the steel tube can be related to the time of water penetration or the onset of corrosion.

As illustrated in Figure 5.1, an OP for corrosion detection is based on light reflection at the end of an optical fiber with a core refractive index n_1. The fiber is stripped and cut with a cleaver to produce a flat surface that is perpendicular to the fiber axis. When light is sent through the optical fiber, a significant part of the light is reflected as a function of the refractive index n_2 of the ambient environment to which the flat surface is directly exposed. When n_2 is changed to n_2' due to change of the ambient condition (e.g. from air to water), the intensity of the reflected light changes accordingly and thus is a function of the environmental condition.
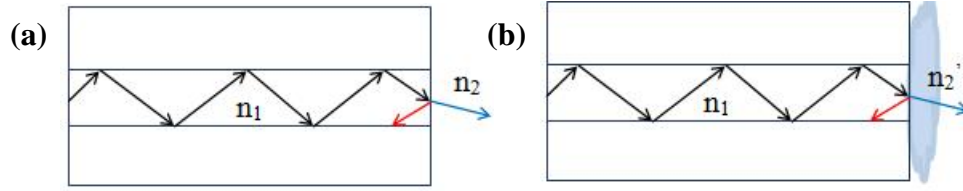
Figure 5.1. Illustration of the working principle of an OP.

According to the Fresnel equation theory [127], when light propagates through an optical fiber and encounters a discontinuity between two media of different refractive indices, a certain amount of light is reflected backward. The Fresnel reflectance at the interface of fiber (n_1 1.5) and air (n_2 1.0) can be expressed into:

$$R = \frac{1}{2}\left[\left|\frac{n_1 \cos\theta_i - n_2\sqrt{1-(\frac{n_1}{n_2}\sin\theta_i)^2}}{n_1 \cos\theta_i + n_2\sqrt{1-(\frac{n_1}{n_2}\sin\theta_i)^2}}\right|^2 + \left|\frac{n_1\sqrt{1-(\frac{n_1}{n_2}\sin\theta_i)^2} - n_2 \cos\theta_i}{n_1\sqrt{1-(\frac{n_1}{n_2}\sin\theta_i)^2} + n_2 \cos\theta_i}\right|^2\right] \tag{5.1}$$

where R is the total reflectance of s-polarized and p-polarized light and θ_i is the angle of the incident light. The return loss can be written by [128]:

$$\text{Return loss (dB)} = -10\log(1-R) \tag{5.2}$$

When a portion of optical fiber and its end flat surface are encapsulated in a steel tube, the flat surface is initially exposed to air, acts like a mirror, and reflects all or most of the light travelling along the fiber. As the steel tube is corroded to the point that its thin wall is punched through, the corrosion products or solution flows into the encapsulated space and exposes the flat end of the optical fiber to a different ambient condition. Correspondingly, the reflected light intensity changes.

In theory, many corrosion pits could occur on the wall of the steel tube at the same time with different corrosion rates. The one with the highest corrosion rate penetrates through the wall first, corresponding to the time when the light intensity changes. By employing a series of steel tubes with different wall thicknesses, the evolution of various corrosion pits can be monitored over time. As such, only several discrete levels of corrosion can be detected in practice. The proposed OP is thus referred to as a corrosion threshold-based sensor.

5.3. CORROSION DETECTABILITY OF THE PROPOSED PROBE

A steel disc of 10 mm thick was cut from a Grade 60, #8 steel bar with a diameter of 25.4 mm. Its cross section was abraded with silicate carbide papers with grit up to 600. After abrading, the end portion of an optical fiber with a flat end surface was attached onto the polished smooth surface of the steel disc with two pieces of adhesive tapes as shown in Figure 5.2. Then, the steel disc and the optical fiber were immersed in 3.5 wt. % NaCl solution up to 24 hours.
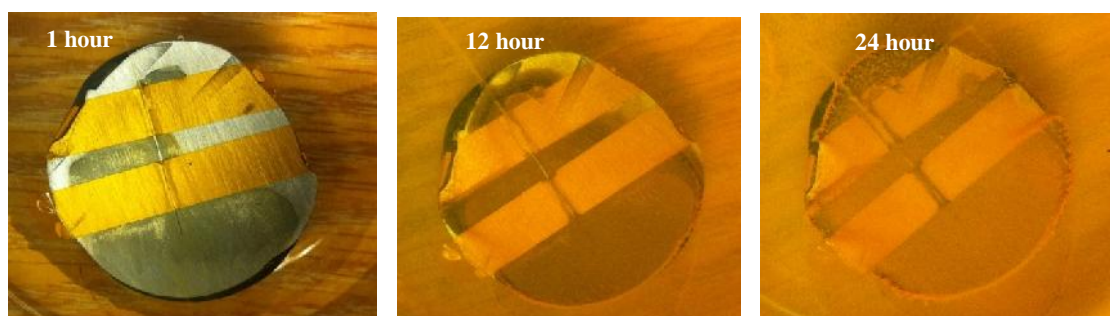
Figure 5.2. Change of reflectivity over time in 3.5 wt. % NaCl solution.

Figure 5.2 shows the surface conditions of the steel disc after immersion in 3.5 wt. % NaCl solution for 1, 12 and 24 hours. It can be seen that, after 1 hour, the smooth white mirror-like steel surface became dark due to the generation of corrosion products. After 12 hours, the overall surface was covered with corrosion products. Especially after 24 hours, a relative thick layer of corrosion products covered on the steel surface and the flat end surface of the optical fiber.

Figure 5.3(a) shows the evolution of the reflectivity of the optical fiber over time. Once immersed in the salt water, the reflectivity suddenly reduced to -12 dB. This is because the ambient environment changed from air to water, and the refractive index of air and water are 1.00 and 1.33, respectively. Figure 5.3(b) shows the zoom-in change of the reflectivity in the salt solution as a function of time. The reflectivity exponentially decreased over time from -12.2 dB at the beginning to -13.7 dB after 24 hours. This is because the generation of corrosion products surrounding the end of the optical fiber. In comparison with the measurement resolution of the optical spectrum analyzer (OSA, Yokagawa AQ6370C), the range of reflection change is significant and promising in applications.
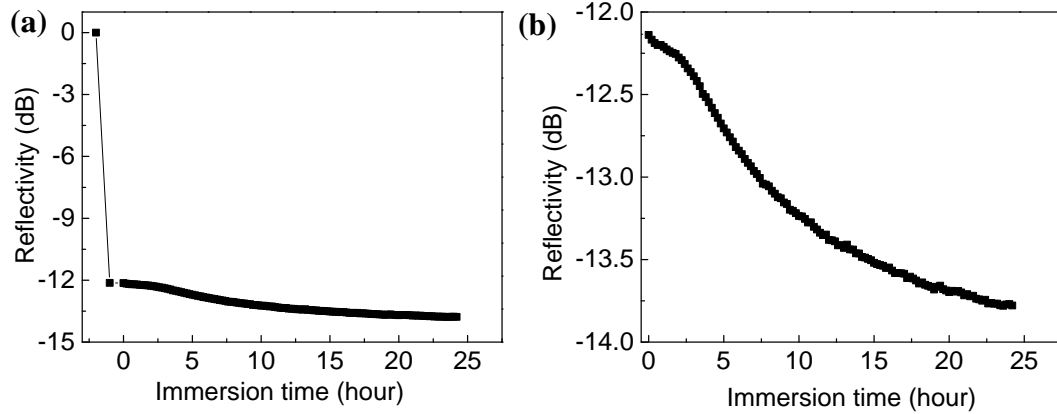
Figure 5.3. Change of reflectivity over time: (a) from air to 3.5 wt. % NaCl solution and (b) in the solution only.

5.4. EXPERIMENTAL DETAILS

Steel tubes were made from Grade 60 steel rebar. Their chemical composition was determined and listed in Table 5.1. The inside diameter of these steel tubes was 300 µm, which is larger than the diameter of the optical fiber (125 µm). Four wall thicknesses were considered, including 500 µm, 750 µm, 1000 µm and 1250 µm. They are all 50 mm in length, which is greater than the grating part of a long period fiber grating (LPFG) sensor for temperature compensation as needed. The inside of these steel tubes was cleansed by first injecting NaOH solution by pressure and then distilled water. The tubes were then put in an oven to keep them dry. A total of 12 steel tubes were fabricated and tested.

Table 5.1. Chemical composition of steel bar

Element	C	Si	Mn	P	S	Cr	Ni	Cu	Fe
Wt. %	0.383	0.184	1.000	0.115	0.064	0.103	0.198	0.373	97.40

Single mode optical fiber with core and cladding diameters of 8 µm and 125 µm, respectively, was used in this study. One end of the optical fiber was cleaved using an optical fiber cleaver, and then passed through a steel tube. Marine epoxy resin was used to seal the two ends of the steel tube to protect the end surface of the optical fiber as shown in Figure 5.4(a). After curing for 12 hours, a copper wire was connected with the steel tube close to one end for electrochemical tests as shown in Figure 5.4(b).

Figure 5.4. Steel tube encapsulated OP: (a) before and (b) after copper wire connection.

The steel tubes were first immersed in saturated $Ca(OH)_2$ for three days to have a stable passive film formed on their surface. The saturated $Ca(OH)_2$ was made by mixing purified $Ca(OH)_2$ powder with distilled water. The saturated condition was ensured by observing the undissolved $Ca(OH)_2$ residue at the bottom of the solution. After three days, sodium chloride was added into the saturated $Ca(OH)_2$ solution to reach a concentration of 3.5 wt. %. The addition of sodium chloride was used to generate pitting corrosion on the passive film. The steel tubes immersed in the solution are shown in Figure 5.5(a).

Electrochemical impedance spectroscopy was used to monitor the pitting corrosion evolution including the formation of passive film, the initiation of pitting corrosion, and the propagation of pitting corrosion. The EIS test was conducted with a typical three-electrode setup that consisted of a $25.4 \times 25.4 \times 2.54$ mm platinum sheet as the counter electrode, a saturated calomel electrode (SCE) as a working electrode, and the steel tube as a working electrode. These electrodes were connected to a Gamry, Reference 600 potentiostat/galvanostat/ZRA for data acquisition. The EIS test was carried out at a scanning rate of 5 points per decade from 100 kHz to 5 mHz with a sinusoidal potential of 10 mV around the open circuit potential. Before each EIS test, a stable open circuit potential was obtained.

To monitor the formation of passive film, OCP was measured every 3 hours, and EIS was performed at the immersion time of beginning, 12 hours and 48 hours. After addition of NaCl, the OCP and EIS were performed every month until a dramatic change of light spectrum was observed. The optical fiber inside each steel tube was connected to a broadband source (BBS) on one end and to the optical spectrum analyzer (OSA) on the other end for spectra as shown in Figure 5.5(b).
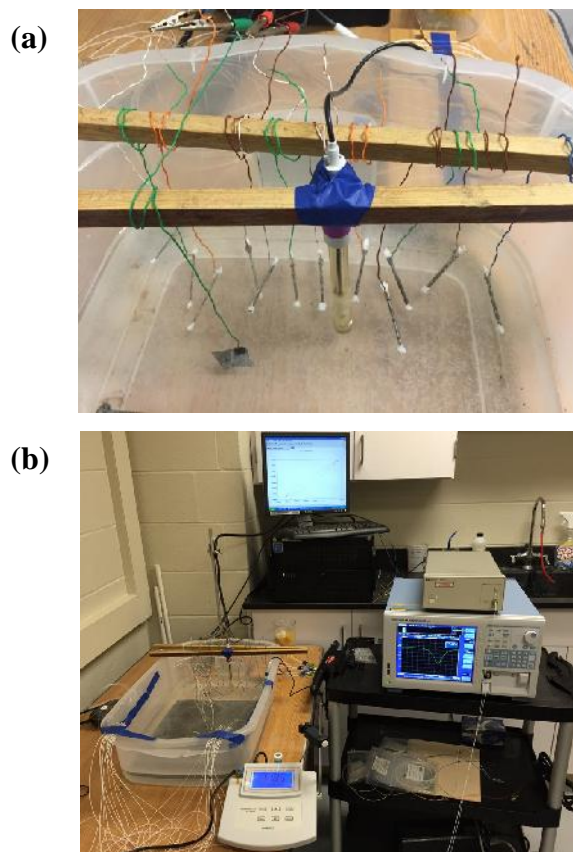
Figure 5.5. Specimens and test setup.

5.5. TEST RESULTS AND DISCUSSION

In this section, the characteristics of pitting corrosion was determined through the corrosion measurement and the average pitting corrosion rate was obtained. The change time of reflectivity of optical fiber inside the tube with different wall thicknesses was measured though an optical spectrum analyzer (OSA, Yokagawa AQ6370C). Then, the relationship between pitting penetration and corrosion time was established.

5.5.1. Passivation and Initiation of Pitting Corrosion. Figure 5.6(a) shows the change of open circuit potential (OCP) in four representative steel tubes with different wall thicknesses when immersed in saturated $Ca(OH)_2$ without NaCl. The OCP increased dramatically from 380 mV to -240 mV in the first 3 hours, which was attributed to the formation of a stable passive film on the surface. Figure 5.6(b) shows the OCP evolution after addition of the NaCl powder. A dramatic decrease from -250 mV to -500 mV can be observed, which was associated with the breakdown of passive film and the initiation of pitting corrosion. No significant change in the OCP was observed till the end of the tests.
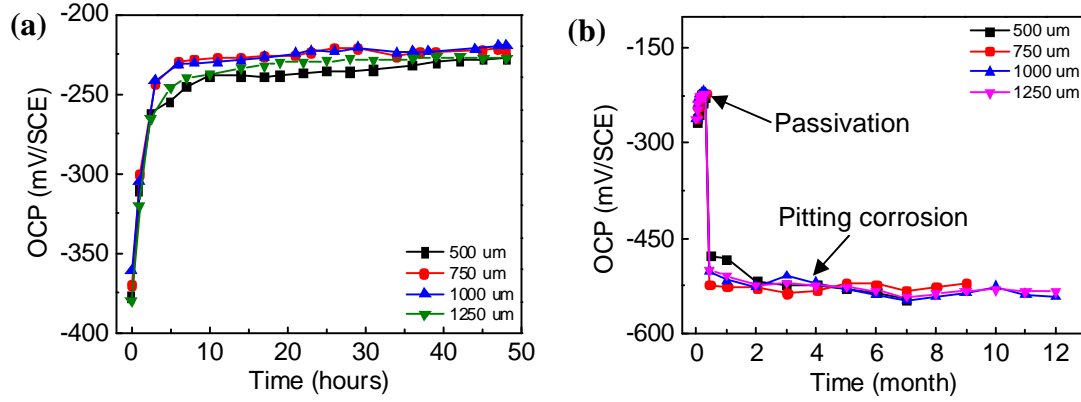
Figure 5.6. OCP in saturated Ca(OH)$_2$ solution: (a) without NaCl and (b) with NaCl.

5.5.2. Linear Polarization Resistance and Pitting Corrosion Rate. Figure 5.7 shows the change of linear polarization resistance (LPR) curves over time for four representative steel tubes with different wall thicknesses. The polarization resistance, R_p, can be calculated by:

$$R_p = \frac{\Delta E}{\Delta I} \tag{5.3}$$

where ΔE and ΔI represent the potential and current increments in the linear portion of the LPR curve at $I = 0$. The polarization resistance was used to calculate the pitting corrosion current density using:

$$i_{corr} = \frac{B}{AR_p} \tag{5.4}$$

where A is the pitting corrosion area that was determined using software Image, i_{corr} is the corrosion current density, R_p is the polarization resistance from LPR results, $B = 26\ mV$ is a constant related to the Tafle slopes of a polarization curve.

The corrosion current density at the active pitting corrosion sites was calculated using Equation (5.3) and listed in Table 5.2. The pitting corrosion rates on all three steel tubes with the same wall thickness are quite different. This is because the areas of the active pitting corrosion are different. It is noted that with an increase of wall thickness, the average pitting corrosion rate increased. It is because the ratio of cathodic and anodic areas of a thick-wall steel tube is higher than that of a thin-wall steel tube, resulting in higher corrosion rates.
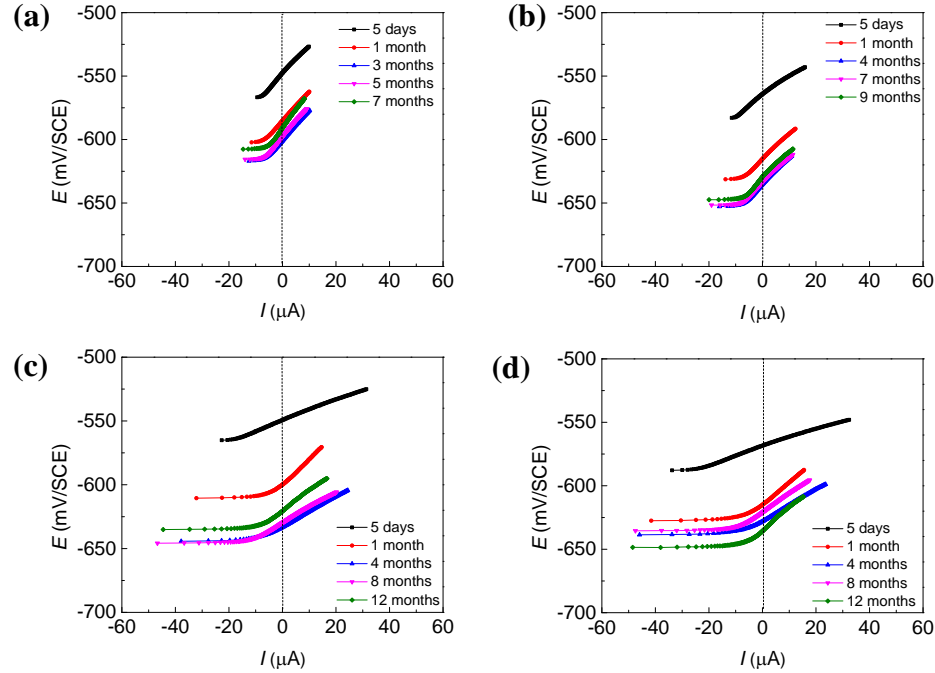
Figure 5.7. LPR of four steel tubes with wall thickness of: (a) 500 µm, (b) 750 µm, (c) 1000 µm, and (d) 1250 µm.

The corrosion current density at the active pitting corrosion sites was calculated using Equation (5.3) and listed in Table 5.2. The pitting corrosion rates on all three steel tubes with the same wall thickness are quite different. This is because the areas of the active pitting corrosion are different. It is noted that with an increase of wall thickness, the average pitting corrosion rate increased. It is because the ratio of cathodic and anodic areas of a thick-wall steel tube is higher than that of a thin-wall steel tube, resulting in higher corrosion rates.

Table 5.2. Average pitting corrosion rate

Specimen	500 µm			750 µm			1000 µm			1250 µm		
	#1	#2	#3	#1	#2	#3	#1	#2	#3	#1	#2	#3
Average i_{corr} ($\mu A/cm^2$)	102	67	126	156	133	97	163	137	152	244	171	320

5.5.3. Changes of Reflectivity. Figure 5.8 shows the reflectivity of optical fiber over a wavelength range of 1500 nm and 1600 nm for four representative optical fibers encased in steel tubes with different wall thicknesses. With a wall thickness of 500

µm, a dramatic decrease of reflectivity was present after 5 months of immersion, indicating the penetration of pitting corrosion through the wall. Prior to 5 months, the reflectivity fluctuated around -1 dB, which is likely attributed to the disturbance during connection to the OSA for every test. The variation of the reflectivity between 1500 nm and 1600 nm is very small. However, it increases once corrosion penetrates through the steel tube. The increase of the reflectivity is due to the non-uniform distribution of corrosion products on the flat end of the optical fiber. With a wall thickness of 1250 µm as shown in Figure 5.8(d), a significant decrease of the reflectivity happened when the immersion time reached around 12 months.
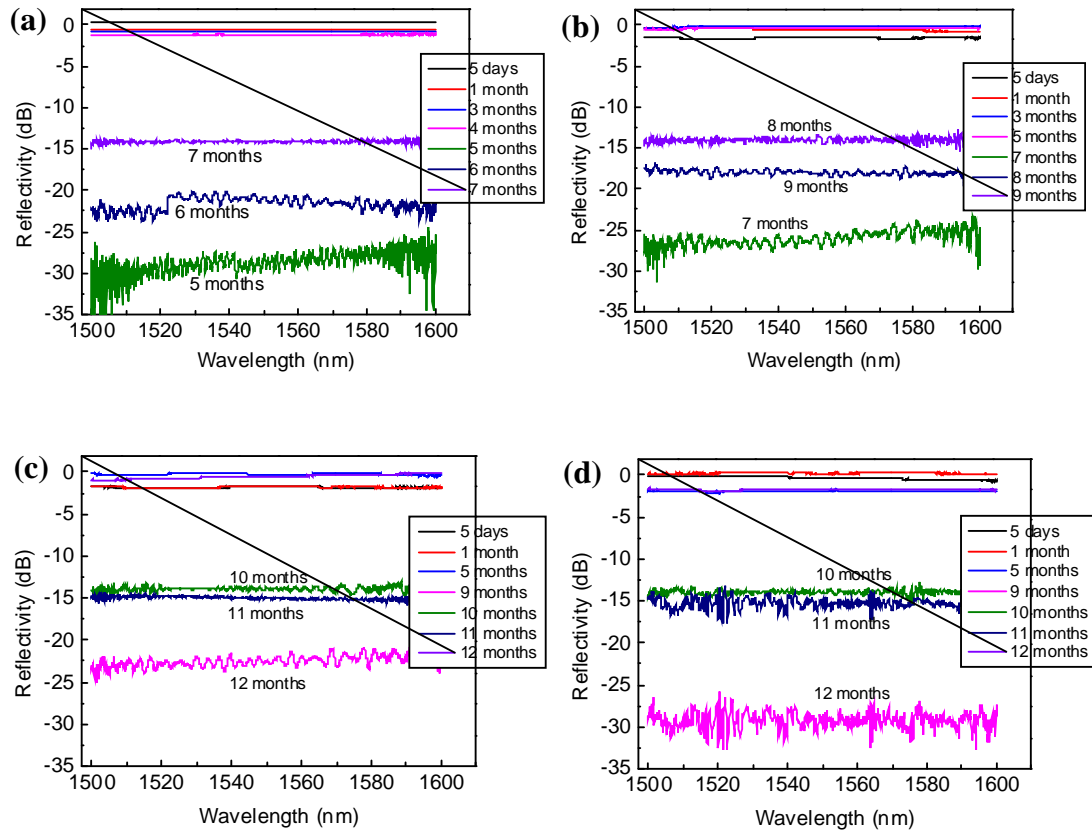
Figure 5.8. Reflectivity of the fibers with encasing steel tubes in 3.5 wt. % NaCl solution with a wall thickness of: (a) 500 µm, (b) 750 µm, (c) 1000 µm, and (d) 1250 µm.

Figure 5.9 presents the reflectivity over time for the optical fibers encased in all tested steel tubes. The time when a dramatic change of the reflectivity of the optical fiber occurs increases with an increase of the wall thickness of the steel tubes.
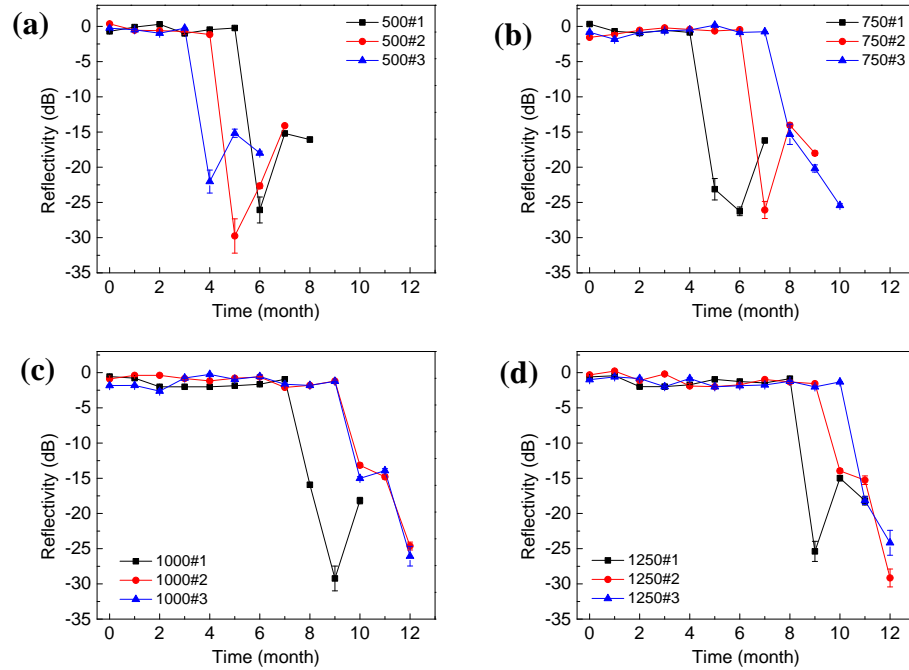
Figure 5.9. Reflectivity of the fibers over time with a wall thickness of: (a) 500 µm, (b) 750 µm, (c) 1000 µm, and (d) 1250 µm.

Figure 5.10 summaries the pitting penetration depth and corresponding time, which are extracted from Figure 5.9. A linear regression analysis was performed and a coefficient of determination 0.89 shows a strong linear relation between the pitting penetration and the corrosion time. With an increase of wall thickness, the time of penetration increases.
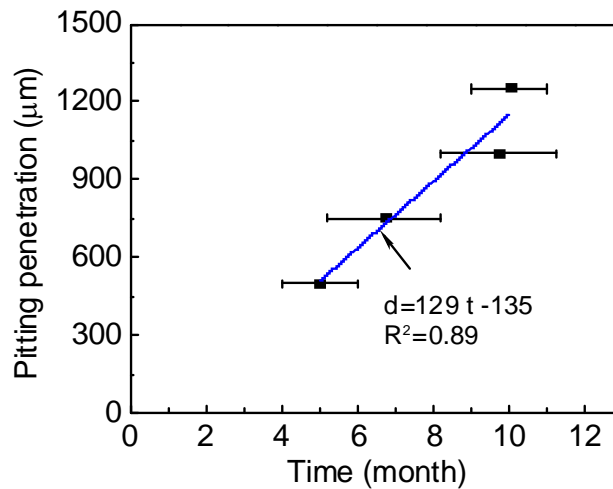
Figure 5.10. Time of penetration as a function of wall thickness.
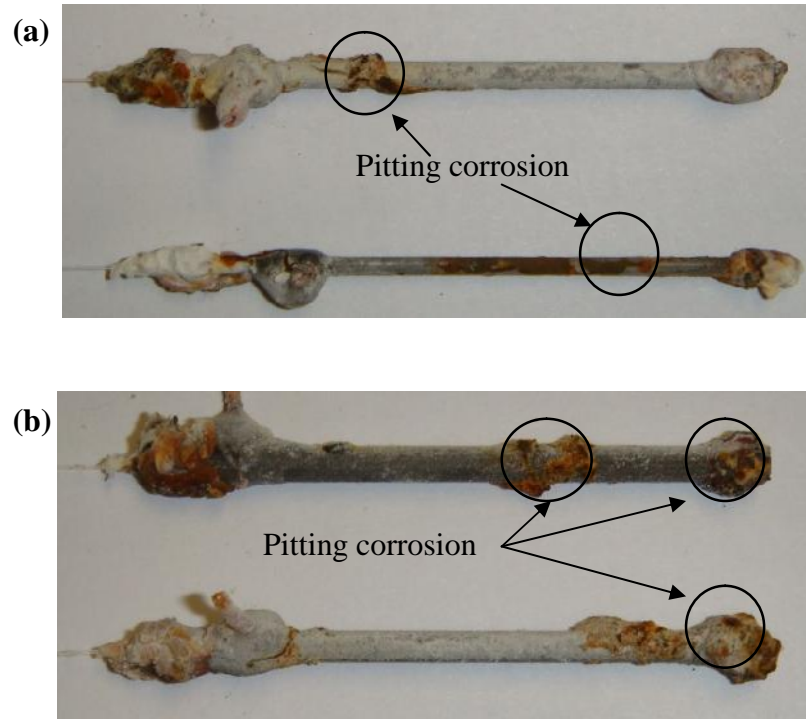
Figure 5.11. Condition of the tested steel tubes after 12 months of immersion in 3.5wt. % NaCl solution.

Figure 5.12 shows cross-sectional images of the two types of localized corrosion. Pitting corrosion occurred most in the middle of the steel tube, far away from epoxy resin. It penetrated through the wall locally as shown in Figure 5.11(a). Crevice corrosion happened at the end of the steel tube with epoxy resin. It penetrated uniformly around the perimeter of the steel tube as indicated in Figure 5.11(b).
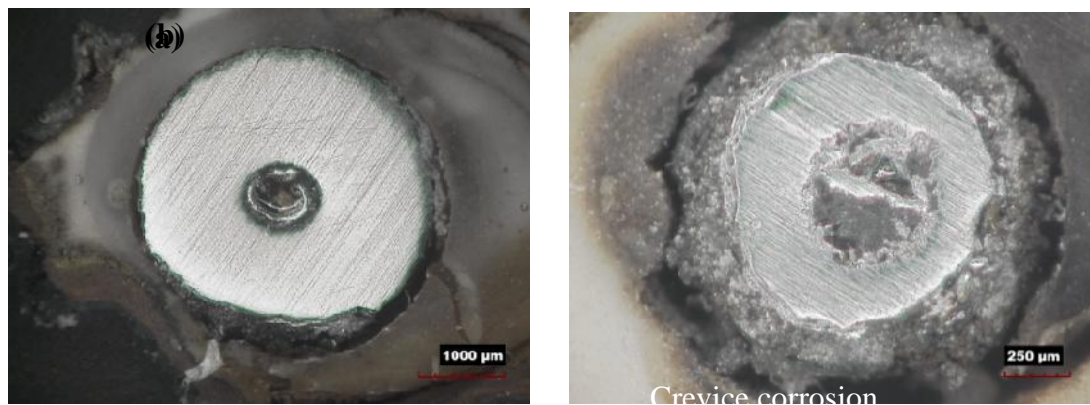
Figure 5.12. Localized corrosion: (a) pitting corrosion and (b) crevice corrosion.

5.6. CONCLUSIONS

In this study, the flat end surface of an optical fiber acting like a mirror was used as a sensor to measure the change of ambient refractive index, which results from the contamination of corrosion products and solution. Based on the test results, the following conclusions can be drawn:

(1) The pitting corrosion rate depends on the surface area of a steel tube. With an increase of the wall thickness, the average pitting corrosion rate increases due to area effects.

(2) Corrosion occurred in two regions of a steel tube: pitting corrosion in the middle and crevice corrosion at the two ends with epoxy resin. Pitting corrosion is non-uniform and penetrates through the wall thickness of the tube locally, while crevice corrosion attacks the perimeter of the steel tube evenly.

(3) The corrosion pit penetration depth can be linearly related to the time when the reflectivity of optical fiber changes suddenly. Therefore, the fiber optic sensor can be used for long-term monitoring of critical pitting corrosion in steel.

6. LONG PERIOD FIBER GRATINGS ENCAPSULATED IN A STEEL TUBE FOR CORROSION MONITORING IN CONCRETE SLAB

6.1. INTRODUCTION

A long period fiber grating (LPFG) sensor will be encapsulated in a steel tube. The encapsulated LPFG sensor will be embedded into a small mortar slab for corrosion monitoring of the steel tube in saturated $Ca(OH)_2$ and 3.5wt. %NaCl solution. The sensor will also determinate the penetration time, T_c, when the test solution flows through the corroded wall of the steel tube and fills the gap between the bare LPFG sensor and the steel tube. With accelerated corrosion test, the mass loss of the steel tube can be related to the penetration time, T_c. The effect of wall thickness of the steel tube on the penetration time will be investigated. The wall thickness of the tube will be related to the time of penetration and the time of sudden change in resonant wavelength of the LPFG.

6.2. SENSING PRINCIPLE

Long period gratings are inscribed on the core of an optical fiber to form a periodic modulation of refractive index over a grating length of a few centimeters. The grating period in the order of 100~1000 µm can considerably exceed the wavelength of radiation propagating in the fiber. The gratings enable coupling of incident light from the propagating core mode to co-propagating cladding modes, producing a series of attenuation bands in a transmission spectrum. The central (resonant) wavelength of each spectral attenuation band can be expressed by,

$$\}_0 = \left(n_{eff}^{co} - n_{eff}^{cl,m} \right) \cdot \Lambda \tag{6.1}$$

where $\}_0$ is the resonant wavelength, n_{eff}^{co} is the effective refractive index of core, $n_{eff}^{cl,m}$ is the effective refractive index of cladding mode LP_{0m} which is associated with the refractive indexes of core n_1, cladding n_2, and environment n_3, and Λ is the grating period. The environmental refractive index n_3 is a reflection of the overall optical property of the surrounding environment, which depends on the type and concentration of different chemical species. Therefore, it has been applied for physical, chemical and bio-chemical sensing.

Figure 6.1 shows the schematic view of an LPFG corrosion sensor encapsulated in a steel tube. The LPFG fiber passes through the steel tube so that all the gratings are enclosed. The two end of the steel tube are sealed with Marine Epoxy. The steel tube was made from a Grade 60 steel bar; it has the same material as the steel bar used as reinforcement in concrete structures. Once the wall of the steel tube is completely corroded away and corrosion products or solution is flowed through the wall, contaminating the environment around the cladding, the ambient refractive index would change, resulting in the shift in resonant wavelength. Therefore, the corrosion-induced mass loss of steel tube can be determined by monitoring the shift of resonant wavelength.
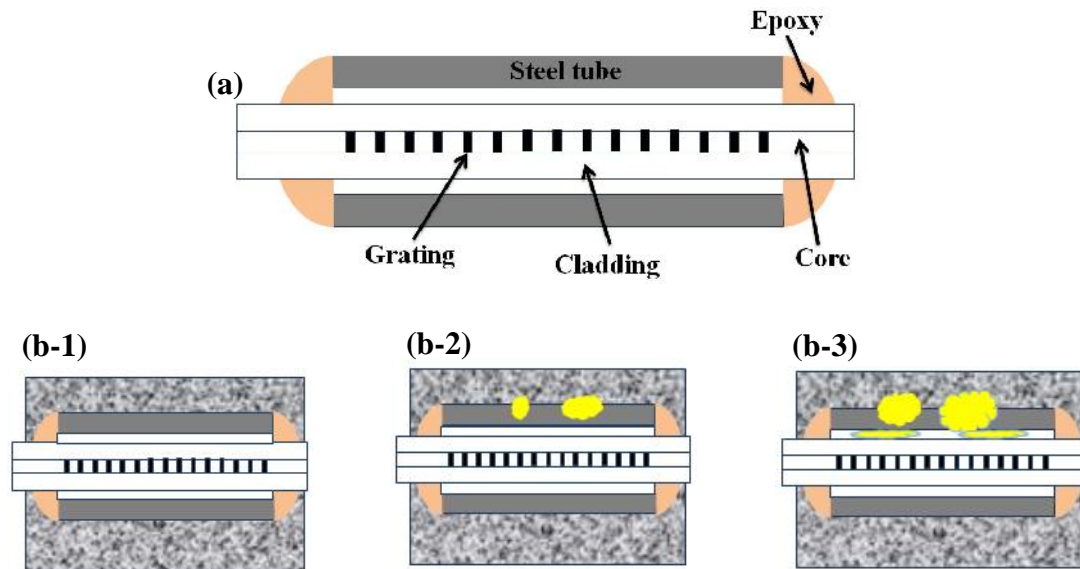
Figure 6.1. A schematic view of the LPFG sensor encapsulated in a steel tube.

6.3. CORROSION DETECTABILITY TEST

To validate the sensitivity of an LPFG corrosion sensor, a steel bar was polished to have a smooth surface. Then, the gratings of an LPFG sensor were directly attached on the smooth surface. The steel bar and the LPFG were immersed in 3.5 wt. % NaCl solution for 12 hours. The change of the light spectrum was recorded every hour.

Figure 6.2 shows the surface conditions of the LPFG sensor after 0 hour, 3 hours, and 12 hours of immersion in 3.5 wt. % NaCl solution. It can be observed that the LPFG was surrounded with pure NaCl solution at the beginning of tests. After 3 hours,

corrosion occurred as indicated by the change in surface color from shinning white to dark, and some corrosion products could be observed. After 12 hours, the LPFG was completely surrounded by brown corrosion products, and the color of salt water changed into brown due to the generation of corrosion products like Fe(OH).
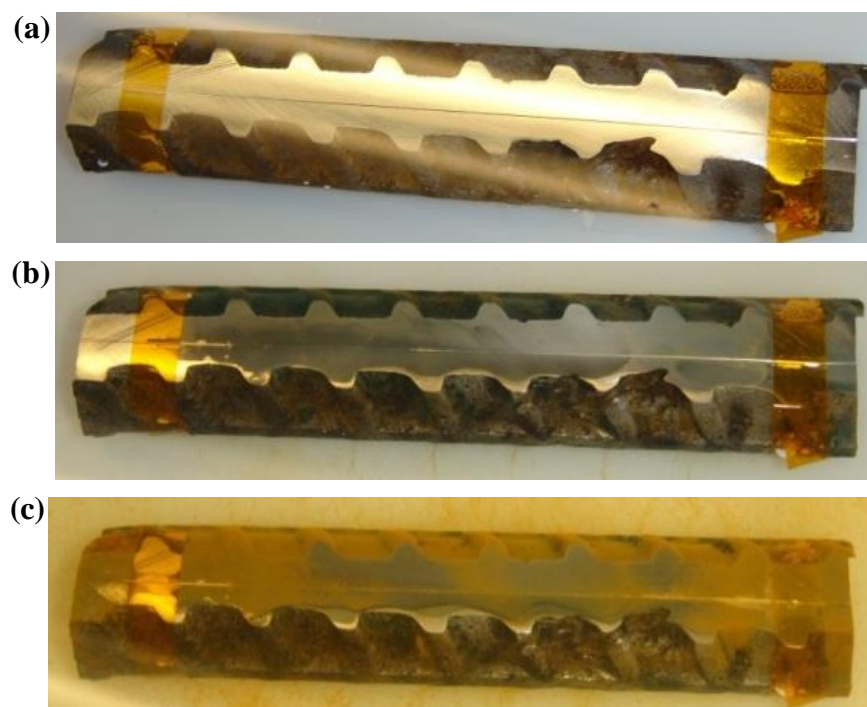
Figure 6.2. Visual observations of the LPFG sensor attached to a steel bar in 3.5 wt. % NaCl solution after (a) 0 hour, (b) 3 hours, and (c) 12 hours.

Figure 6.3 shows the change of the light spectrum over time before and after immersion in 3.5 wt. % NaCl solution. Once immersed in the solution, the resonant wavelength decreased from 1563.0 nm to 1553.0 nm due to the change in the refractive index from the air (n_3 1.0) to salt water (n_3 1.34). After 12 hours of immersion, the resonant wavelength was blue shifted to 1545.0 nm and the transmission increased to -15 dB. The change of the spectrum is attributed to the change in effective refractive index of the NaCl solution due to the generation of corrosion products. After 24 hours, the resonant wavelength increased to 1547.0 nm and became stabilized. The significant change in wavelength and transmission ensures that the LPFG sensor encapsulated in a steel tube can be used as a corrosion sensor.
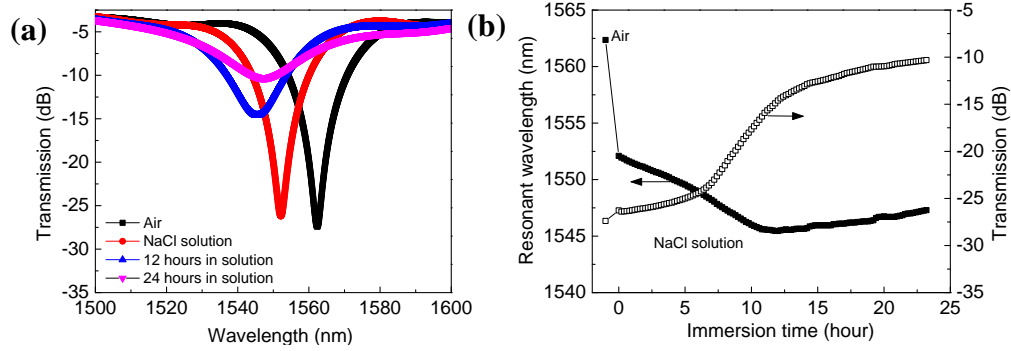
Figure 6.3. Transmission spectra of the steel encapsulated fibers immersed in 3.5 wt. % NaCl solution for different durations.

6.4. APPLICATION IN CONCRETE SLAB

In this section, the used LPFG and steel tube with different wall thicknesses were selected, prepared and described in detail for application in concrete slab. The performance of corrosion test was provided to finally obtain the relation of corrosion attack over time.

6.4.1. Materials and Specimens. Single mode fiber (Corning SMF-28) was used in this study. The refractive indices of its core and cladding are $n_1=1.469$ and $n_2=1.463$. The diameters of the core and the cladding are 8.2 µm and 125 µm. Long period gratings were first inscribed on the optical fiber by a transverse focused beam from a CO_2 laser (SYNRAD, Inc.) with a free-space wavelength of 10.6 µm and an output power of ~7.8 W when the fiber was placed on a computer-controlled motorized translation stage and moved at fixed steps for laser exposure. In particular, the cladding mode LP08 was considered with a grating period of 387±0.1 µm and a total length of approximately 40 mm. The optical fiber with gratings was then cleansed with 20% NaOH solution and distilled water.

Steel tubes were fabricated from Grade 60 steel bars (ASTM C) with a chemical composition listed in Table 6.1. The length of the steel tube was 50 mm with a fixed inner diameter of approximately 300 µm to make sure that the optical fiber can go through easily. A total of five steel tubes were considered with an outer diameter of 400 µm, 800 µm, 1000 µm, 1200 µm and 1500 µm, corresponding to a wall thickness of 50 µm, 250 µm, 350 µm, 450 µm and 600 µm, respectively. For each thickness, three

identical steel tubes were prepared, making a total of 15 steel tube specimens as exemplified in Figure 6.4(a).

Table 6.1. Chemical composition of steel tube

C	Si	Mn	P	S	Cr	Ni	Cu	Fe
0.383	0.184	1.000	0.115	0.064	0.103	0.198	0.373	Balance
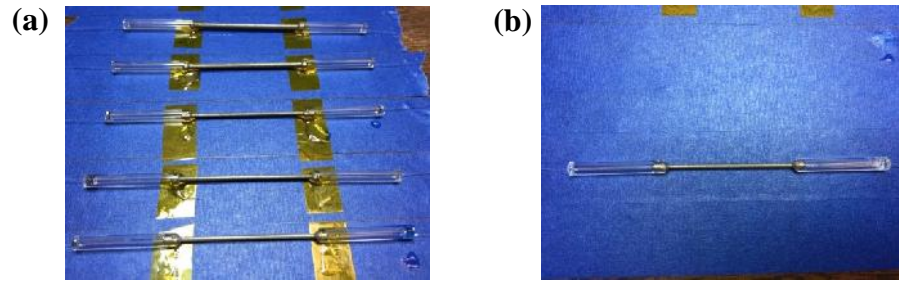
Figure 6.4. Preparation of LPFG sensors encapsulated in steel tubes.

An LPFG sensor and its transmission fiber pass through each steel tube with the long period gratings covered completely. After that, epoxy resin was used to seal the two ends of the steel tube. To protect the optical fiber from bending, two glass tubes were used to shore the two ends of the optical fiber.

The prepared LPFG sensors were embedded into a concrete slab with a dimension of 400 mm ×400 mm ×15 mm. Type I Portland cement was used to fabricate the slab and its chemical composition is given in Table 6.2. To make sure that the concrete cover is 5 mm as designed, dents were cut on two plastic bars to mark the location of steel tubes. The plastic bars are 5 mm in diameter. For corrosion tests, a copper wire was connected with the steel tube prior to concrete casting. The spacing of the steel tubes was approximately 20 mm. The concrete slab and corrosion test setup are displayed in Figure 6.5.

Table 6.2. Chemical composition of Type I Portland cement

SiO_2	Al_2O_3	CaO	MgO	SO_3	Na_2O	K_2O	TiO_2	Fe_2O_3	P_2O_5	Loss on ignition
19.48	6.80	55.35	3.32	4.35	2.39	1.00	0.20	2.18	0.19	3.98
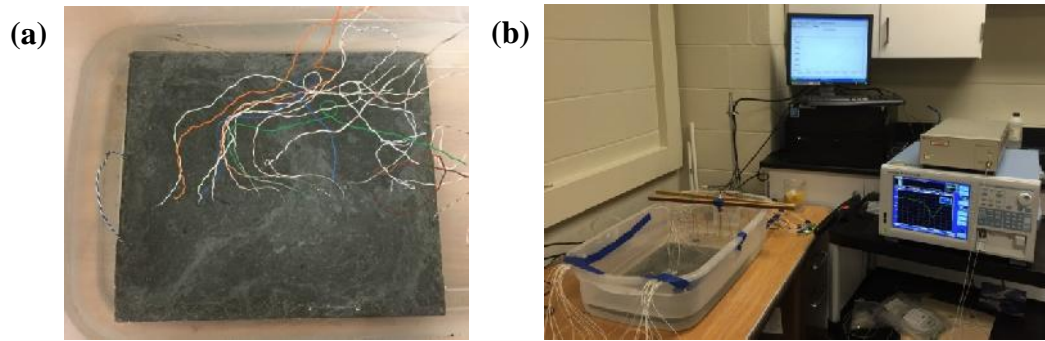
Figure 6.5. Concrete slab and corrosion test setup.

6.4.2. Corrosion Tests. Corrosion of steel bars in concrete is a slow process even in a severe corrosive environment. It may take many years for steel bars to get corroded to a level that results in the onset of concrete cracking. Therefore, accelerated corrosion tests were used in the laboratory to investigate corrosion-induced RC deterioration. After curing for 28 days, the concrete slab was immersed in 3.5 wt. % NaCl solution. A constant current was applied to all steel tubes with the same wall thickness, and five different currents were applied for steel tubes with five different wall thicknesses. The average corrosion current density for all tubes was set to be $100 \, \mu A/cm^2$. The steel tubes and a graphite rod were connected to the positive and negative ends of a power supply, respectively, as schematically shown in Figure 6.6.
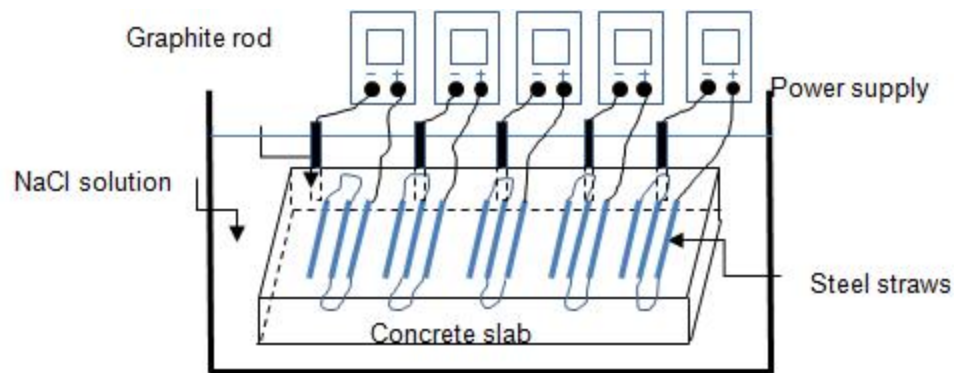
Figure 6.6. Accelerated corrosion test setup.

Although accelerated corrosion tests were performed at a pre-determined corrosion rate of $100 \, \mu A/cm^2$, it is useful to measure the actual corrosion rate without external current. Therefore, approximately at the end of each month, the power supply

was set off for 3 days, and the corrosion rate of each steel tube was measured using linear polarization resistance (LPR) as shown in Figure 6.5(b). The LPR test was conducted using a three-electrode test setup that consists of a 25.4 mm (1.0 in) × 25.4 mm (1.0 in) × 0.254 mm (0.01 in) platinum sheet as a counter electrode, a saturated calomel electrode (SCE) as a reference electrode, and a steel tube as a working electrode. These electrodes were connected to a Gamry, Reference 600 potentiostat/galvanostat/ZRA for data acquisition. The LPR curves were measured within the open circuit potential of 20 mV at a scanning rate of 0.167 mV/s. The polarization resistance can be calculated by,

$$R_p = \Delta E / \Delta I \tag{6.2}$$

where ΔE and ΔI represent the voltage and current increments, respectively, in the linear portion of the polarization curve at $I = 0$. LPR measurement was used to calculate the corrosion current density using the Stern-Geary equation,

$$i_{corr} = B / (A R_p) \tag{6.3}$$

where i_{corr} is the corrosion current density, A is the surface area of steel tube, and B is a constant. In this study, $B = 26$ mV. The changes in resonant wavelength of the optical fibers were measured using the OSA after each corrosion test.

6.5. RESULTS AND DISCUSSION

In this section, the corrosion rate of steel tube embedded in mortar was obtained before and after the application of external power supply. The corrosion penetration depth was determined though the change time of resonant wavelength by measuring the spectrum of LPFG.

6.5.1. Corrosion Test Results. Figure 6.7 shows the LPR curves of five representative steel tubes with different wall thicknesses as a function of test time. Prior to the application of external current (1 day), the steel tubes have a corrosion potential of approximately -220 mV, and the slopes of the LPR curves are high. After the application of external current, the corrosion potential was reduced to around -650 mV, indicating an active corrosion state.
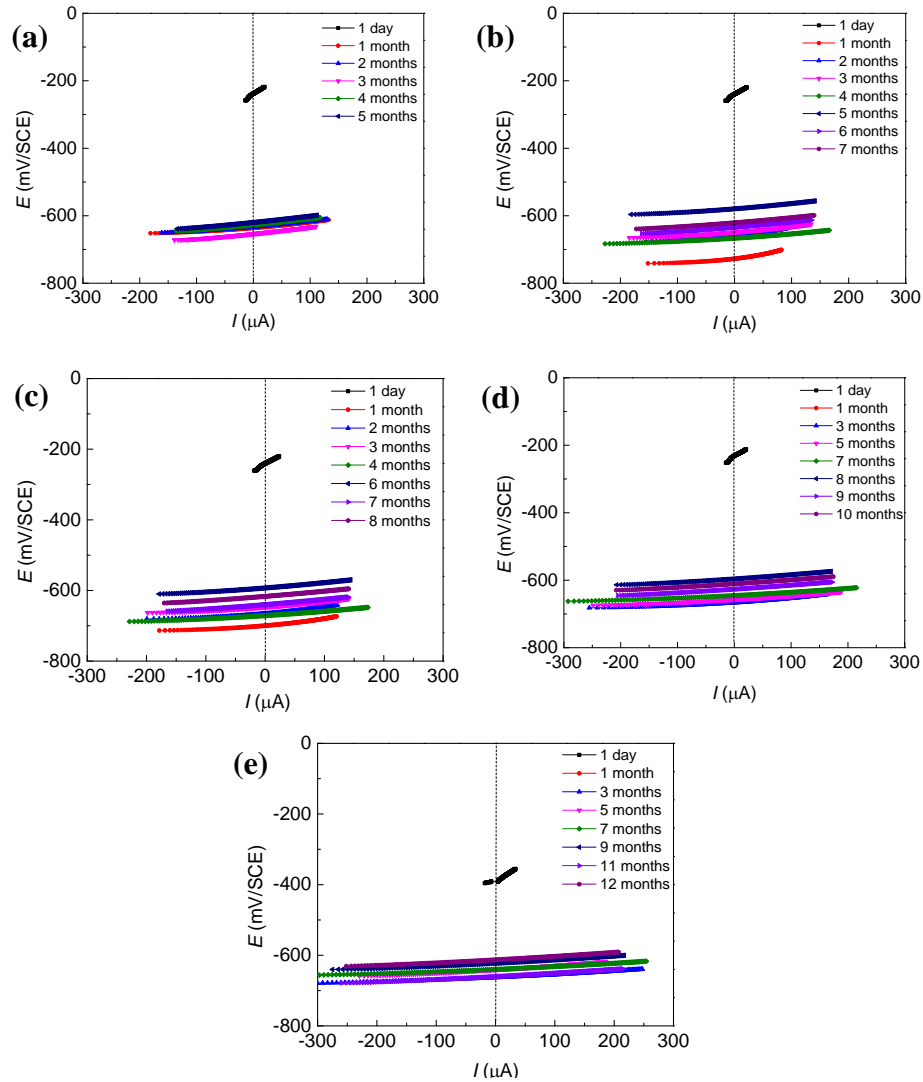
Figure 6.7. LPR curves for steel tubes with a wall thickness of: (a) 400 µm, (b) 800 µm, (c) 1000 µm, (d) 1200 µm, and (e) 1500 µm.

Figure 6.8(a) shows the variation of polarization resistance over time for five representative steel tubes with different wall thicknesses. In the passive state before the application of external power for accelerated corrosion tests, the polarization resistances are greater than 1 k . After the application of external power supply, the polarization resistances vary around 100   regardless of wall thickness. The polarization resistance can be transformed into a corrosion current density as shown in Figure 6.8(b). In addition to the corrosion current densities from LPR tests, the corrosion current densities from external power supplies were also displayed for comparison. It can be seen that, the

corrosion rates of steel tubes in natural state (LPR tests) range from 40 to 60 $\mu A/cm^2$, which is lower than the accelerated corrosion rate 100 $\mu A/cm^2$.
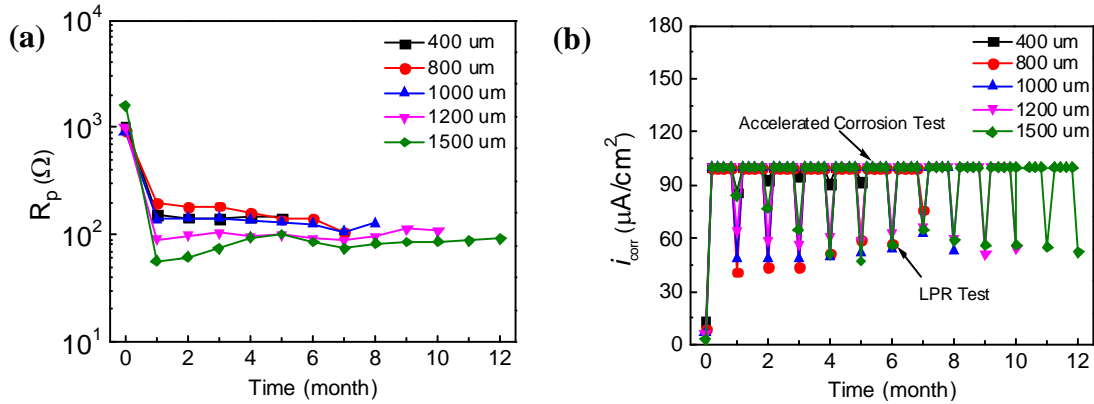
Figure 6.8. Change of (a) polarization resistance and (b) corrosion rate over time.

6.5.2. Transmission Spectra. Figure 6.9 shows the change of light spectra over time for five representative LPFGs encased in steel tubes with different wall thicknesses. Two stages can be observed: the stable stage and the stage that a sudden change in light spectrum happened. In the stable stage, the resonant wavelength did not change significantly, which means no corrosion penetration through the wall thickness of steel tubes. However, the transmission density varied slightly after each test, which was due to potential change in the input energy from the power source. The sudden change in the transmission spectrum is due to the penetration of corrosion products through the hole on the wall of the steel tubes, resulting in change in the effective refractive index of the ambient environment. After a significant change was observed for each LPFG, the spectrum was measured continuously for additional two months. It is noted that, with an increase of the wall thickness, the time that is needed for spectral change increased. For example, the time of sudden spectral change was 3 months with a wall thickness of 400 μm, and was increased to 5, 6, 8, 11 months with a wall thickness of 800 μm, 1000 μm, 1200 μm, 1500μm, respectively. The resonant wavelength was reduced once the corrosion products penetrated through the wall due to an increase of the effective refractive index from air to a mixture of corrosion products and salt solution.
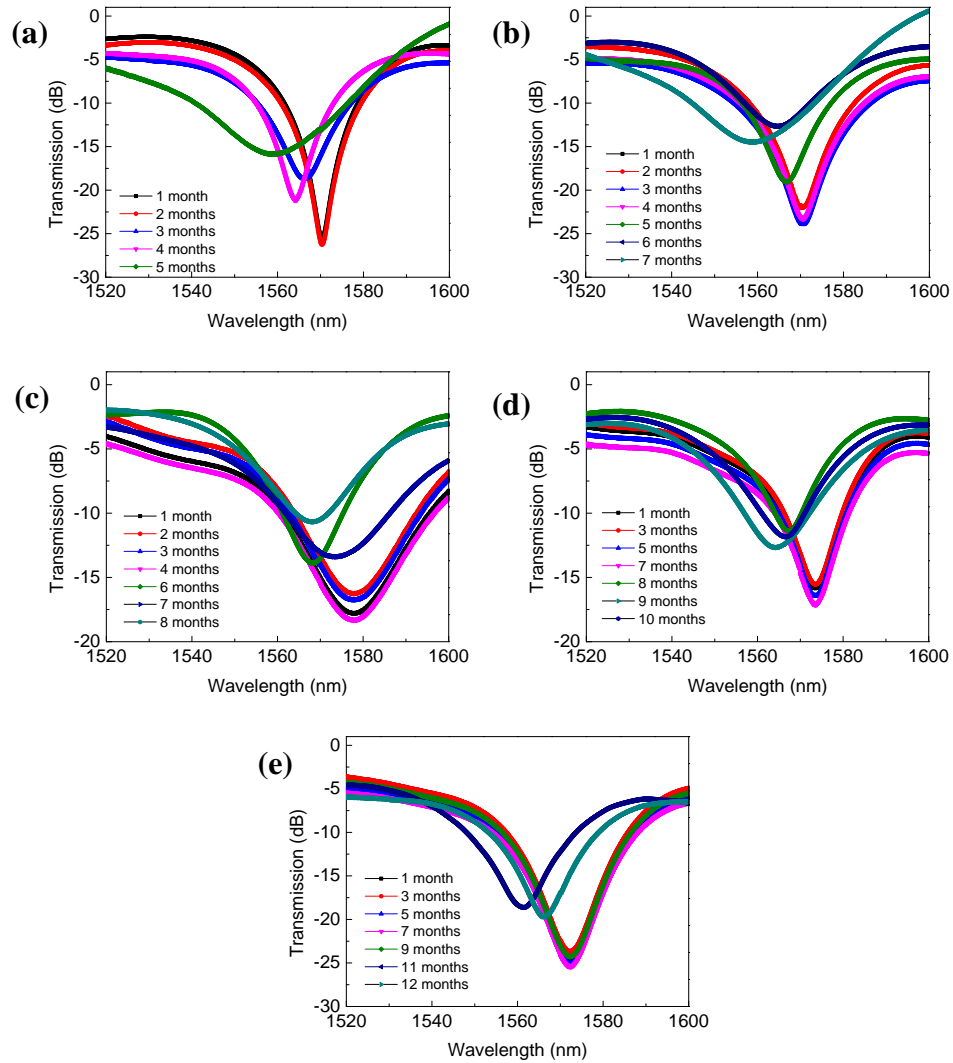
Figure 6.9. Spectrum change over time for LPFGs encased in steel tubes with a wall thickness of: (a) 400 µm, (b) 800 µm, (c) 1000 µm, (d) 1200 µm, and (e) 1500 µm.

Figure 6.10 shows the change in resonant wavelength of all LPFGs encased in the steel tubes over time. For all three LPFGs encased in the steel tubes with the same wall thickness, the time for change in the resonant wavelength varied. Take the three LPFGs in steel tubes with a wall thickness of 1000 µm for example, as shown in Figure 6.10(c), the sudden decrease of resonant wavelength occurred at 5 months, 6 months and 7 months. The variation is attributed to the non-uniform distribution of corrosion rates over the entire steel tube surface. Although a constant external electrical current was applied for all three tubes with the same wall thickness, the distribution of corrosion current was

random, which was affected by the non-homogeneity of concrete slab cover and by the distance to the graphite rod.
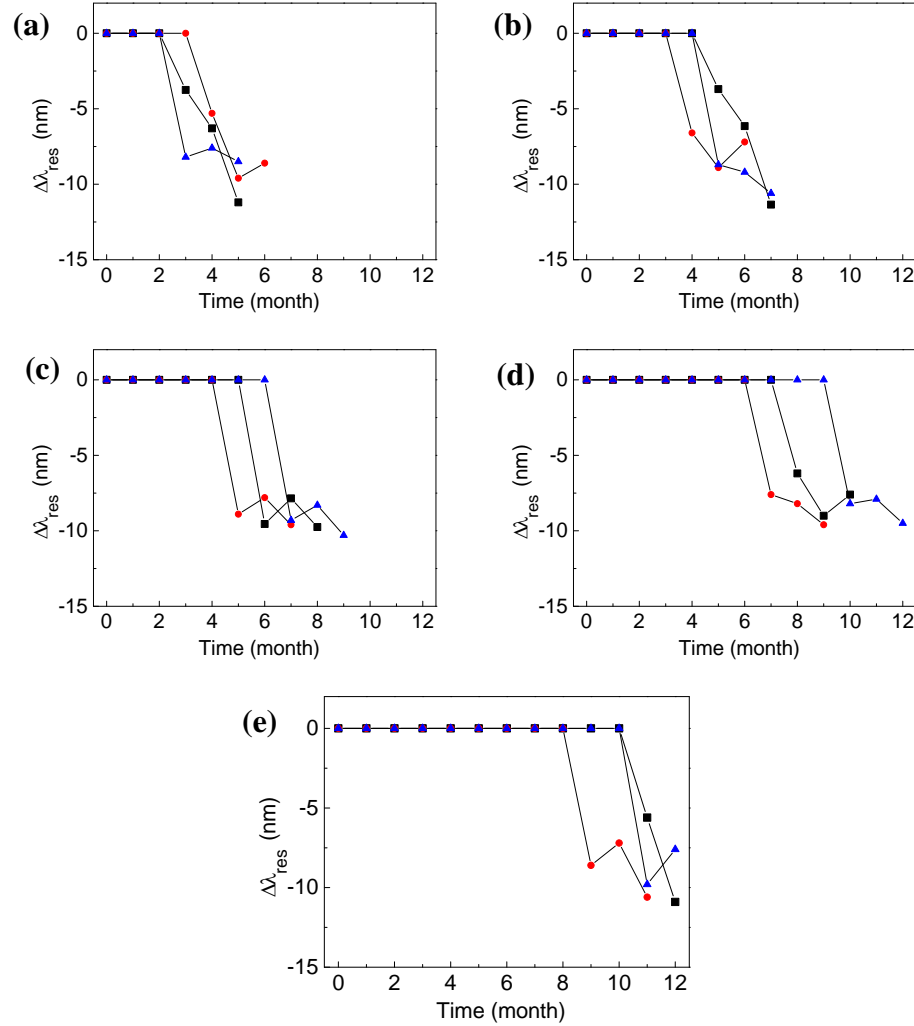
Figure 6.10. Change of resonant wavelength over time for LPFGs encased in steel tubes with a wall thickness of: (a) 400 µm, (b) 800 µm, (c) 1000 µm, (d) 1200 µm, and (e) 1500 µm.

Figure 6.11 shows the corrosion penetration depth as a function of time. The corrosion penetration depth was equal to the wall thickness of steel tubes once corroded completely. It can be observed from Figure 6.11 that the corrosion penetration depth on the steel increased over time. A linear regression analysis was performed with a coefficient of determination of 0.96, indicating a strong linear correlation between the corrosion penetration depth and time. Note that the corrosion penetration depth was based

on the corrosion rate from external currents ($100 \ \mu A/cm^2$) instead of the corrosion rates in natural state (LPR results). The coefficient of the linear equation depends on the corrosion rate of steel. If no external current was applied, the time required to reach the same corrosion penetration depth may increase by 1.5 to 2.5 times, as the corrosion rate in natural state is 1.5 to 2.5 times lower than the external current as shown in Figure 6.8(b).
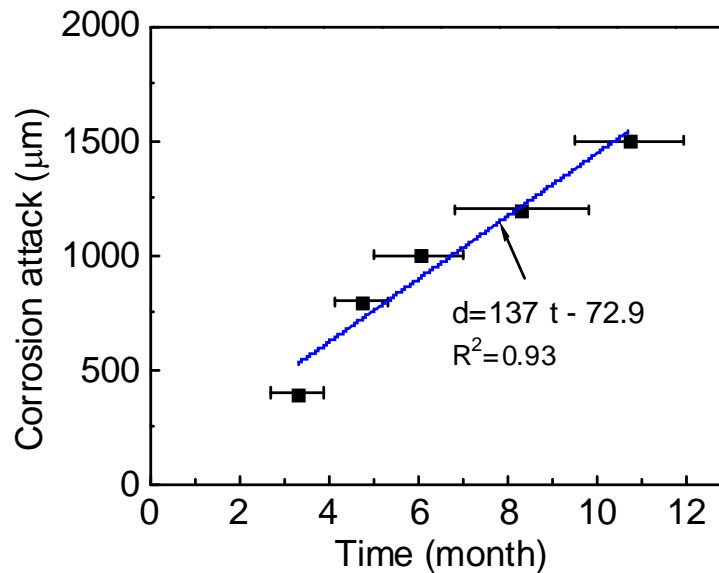
Figure 6.11. Corrosion penetration depth as a function of wall thickness.

6.5.3. Visual Observations. For thin-wall steel tubes, their corrosion tests were terminated at early time. To avoid any potential disturbance on the remaining tests, they were not taken out of the concrete slab until the other steel tubes had been corroded completely. Figure 6.12 shows the surface conditions of four corroded steel tubes retrieved from the concrete slab after 12 months of corrosion test. Brown corrosion products can be seen on the surface of steel tubes. They had penetrated through the concrete cover. In particular, as shown in Figure 6.12(c), the optical fiber can be seen clearly as the other part of the steel tube was corroded off completely. To examine the corrosion-induced damage, the retrieved steel tubes were cast in epoxy resin and abraded with carbide silicate papers for optical microscopic inspection.
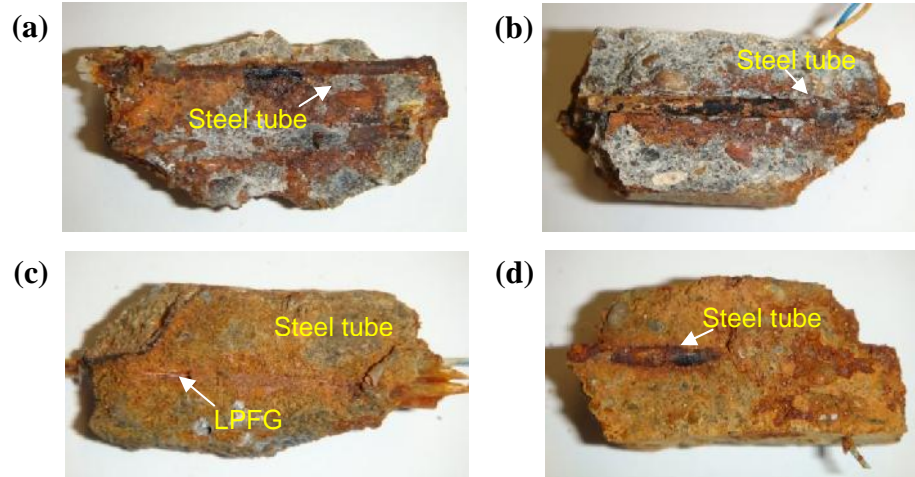
Figure 6.12. Surface condition of steel tubes retrieved from the tested concrete slab.

Figure 6.13 shows the microscopic images of the cross sections of steel tubes with traces of the LPFG sensors. In particular, the sensors can be clearly observed in Figures 6.13(b) and 6.13(c). However, no LPFGs were present in Figures 6.13(a) and 6.13(d) likely because they were damaged when the slab was broken using a hammer. It can be seen from Figure 6.13 that the corrosion penetration depth was not uniform around the perimeter of the steel tubes and only parts of the steel tubes remained. The LPFG was surrounded with corrosion products as shown in Figure 6.13(c), which is in good agreement with the results of light spectra.
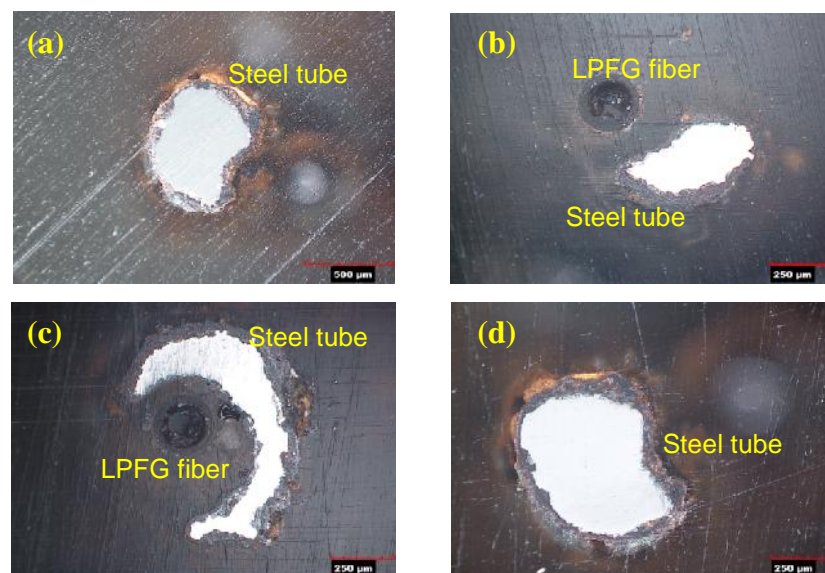
Figure 6.13. Microscopic image of cross sections of steel straws after test.

6.6. CONCLUSIONS

In this study, LPFG sensors were encapsulated in steel tubes, embedded in a small mortar slab, and tested in saturated $Ca(OH)_2$ and 3.5wt. % NaCl solution to monitor the corrosion of the steel tubes and determine the time required to penetrate through the wall of the tubes. Based on the test results, the following conclusions can be drawn:

(1) The corrosion rates of steel tubes in active natural state ranged from 40 to 60 $\mu A/cm^2$, which is 1.5 to 2.5 times lower than the external current density applied during the accelerated corrosion tests.

(2) The resonant wavelength remained constant before corrosion penetration depth penetrated through the wall thickness of steel tubes so that the LPFG sensor was still surrounded by air. It was suddenly reduced significantly once corrosion products replaced the air inside the steel tubes. The time required for the arrival of sudden change in resonant wavelength increased with an increase of the wall thickness.

(3) The corrosion penetration depth can be linearly related to the test time with a sensitivity of 128 µm/month. The LPFG sensor encased in a steel tube can be used for long-term monitoring of the corrosion of steel bars in RC structures.

7. CORROSION MONITORING AND ASSESSMENT OF
REINFORCED CONCRETE BEAMS

7.1. INTRODUCTION

In this study, both Fe-C coated and steel tube encapsulated LPFG sensors will be applied for the life-cycle monitoring and assessment of reinforced concrete (RC) beams subjected to accelerated corrosion tests in salt solution. The objectives of this study are to demonstrate an example application of the developed LPFG sensors and evaluate the capacity reduction of RC beams due to corrosion of reinforcement steel determined from the LPFG sensor. The corrosion-induced reduction in the stiffness of RC beams will be obtained from load-deflection curves at various corrosion stages.

7.2. EXPERIMENTAL PROCEDURE

Three identical RC beams with a length of 3.0 ft (0.914 m) and a cross section of 6.0 in. × 6.0 in. (152 mm × 152 mm) were cast as schematically illustrated in Figure 7.1(a). Each square beam was reinforced with four #3 longitudinal reinforcement bars (a diameter of 0.375 in. or 9.525 mm) with a reinforcement ratio of 0.61%, which were placed at four corners, and one #2 transverse stirrup every 6 in. (15.2 cm) as shown in Figure 7.1(b). Four corrosion sensors were attached to the middle portion of two bottom longitudinal steel bars in each specimen. They are one Fe-C coated LPFG and three steel tube encapsulated LPFG sensors with a wall thickness of 0.50 mm, 1.75 mm, and 1.00 mm, respectively. The Fe-C coated LPFG sensor and the encapsulated sensor with a wall thickness of 0.50 mm were attached on the same steel bar. The remaining two sensors with a wall thickness of 0.75 mm and 1.00 mm were connected together and attached to the other steel bar. For the Fe-C coated LPFG corrosion sensor, the sputtering time of inner silver was 1.5 minutes and the electroplating time of outer Fe-C layer was 90 minutes. The resonant wavelengths of the two steel tube encapsulated LFPGs in series can be determined from two valleys/peaks in a transmission spectrum. It is noted that two LPFGs should have quite different resonant wavelengths in order to separate them from the spectrum.

(a)

2 #3

#2@6" (#2@15.2 cm)

2 #3

6" (15.2 cm)

(b)

Sensor1: Light in ⟶   Fe-C coated LPFG   Light out ⟶

0.50 mm thickness tube

Sensor2: Light in ⟶   Light out ⟶

0.75 mm thickness tube   1.00 mm thickness tube

Sensor3: Light in ⟶   Light out ⟶

#2@6" (#2@15.2 cm)

3"   30"   3"

7.6 cm   76 cm   7.6 cm
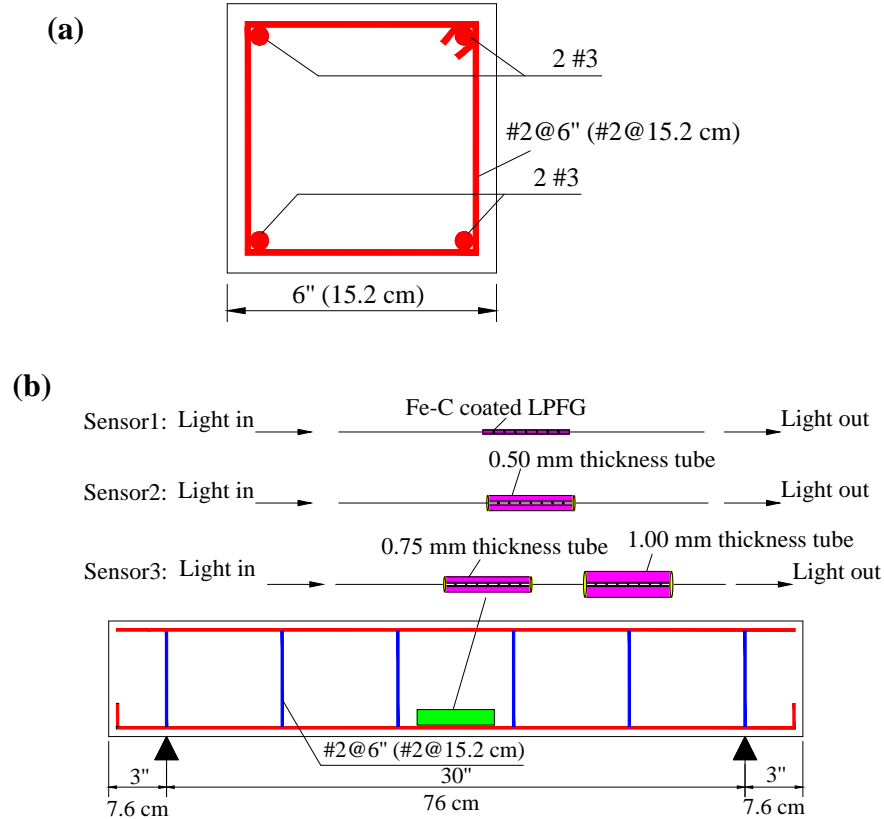
Figure 7.1. RC beam specimen and instrumentation:(a) cross section (b) reinforcement detail and instrumentation plan.

The location of these sensors in the RC beam is shown in Figure 7.2. The contact between stirrups and steel rebar was insulated using a plastic tape to ensure the current only going through the steel bar located at the bottom. The Fe-C coated LPFG was attached to the steel bar surface using a plastic tape to make sure it straight. The steel straw was attached onto the steel bar surface using a copper wire to ensure a good electrical connection. The current density of Fe-C layer and steel straw was assumed to be identical with that of steel bar, as they were in the same environment. Before casting concrete, a thin layer of mortar was first used to cover Fe-C coated LPFG to prevent potential damage during concrete casting. Coper wire was also connected to the bottom two longitudinal steel bars for accelerated corrosion test. After curing for six hours, concrete was cast and the RC beams after casting is shown in Figure 7.3. The concrete was made of tap water, Portland type I cement, Missouri river sand and gravel, which a proportion shown in Table 7.1. After air curing for 28 days, the RC beams were immersed in 3.5% wt. NaCl solution in a tank for accelerated corrosion test. The bottom

steel bars were connected to the positive end of an external power supply, and a graphite rod was immersed in the salt water and connected with the negative end of the power supply.

(a)

(b)
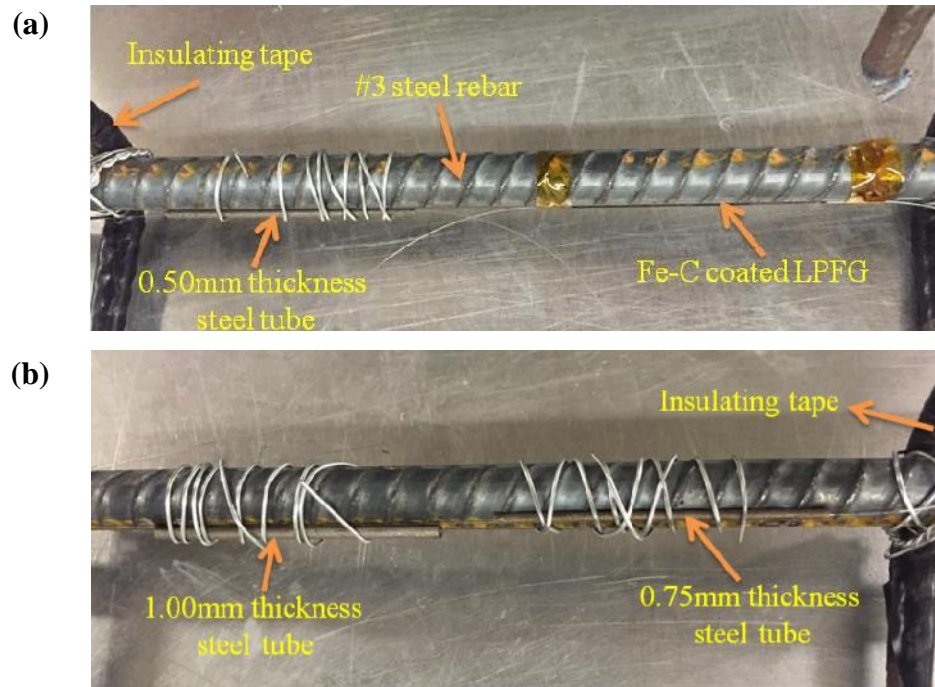
Figure 7.2. (a) Fe-C coated LPFG sensor and the LPFG sensor encased in 0.5 mm steel tube, and (b) the LPFG sensors encased in 0.75 mm and 1.00 mm steel tubes.

Table 7.1. The composition of concrete

Element	Cement	Water	Sand	Gravel
Wt. %	1	0.5	2.05	3.05

Figure 7.3. RC beams and cylinders for corrosion test.

The applied external current was determined by the corrosion-induced mass loss of steel bars, which was 5% per month. The 5% of the weight (997 g) of the two steel bars is approximately 50 g. According to the Faraday's Law,

$$m = \frac{Q}{F}\frac{M}{z} \tag{7.1}$$

where m is the mass of substance liberated at an electrode in grams, Q is the total electric charge passed through the substance in Coulombs, F is the Faraday constant (96485 C/mol), M is the molar mass of substance in gram per mol, and z is the valence number of ions of the substance, which is 2 for iron.

The design total electrical current calculated by the Faraday's Law was around 60.0 mA with an electrical current density was 0.223 mA/cm^2. The average corrosion depth d over time t of the steel bar, the Fe-C coating and the steel tube can be determined using

$$d \approx 7.43 \sim m / day \tag{7.2}$$

Therefore, the mass loss rate of the two steel bars is 1.5 g/day.

Under certain circumstances, repair is required on deteriorated RC structures. To investigate the effect of repair on the corrosion resistance of RC beams, a 15.0 cm long, 1.0 cm wide, and 0.5 cm deep groove was precut on the bottom surface and in the middle portion of the RC beams. A Fe-C coated LPFG was placed in the groove as shown in Figure 7.4(a). To keep it straight, the LPFG sensor was attached onto a stainless steel bar using plastic adhesive tapes as shown in Figure 7.4(a). Once placed in the groove, the Fe-C coated LPFG sensor was covered with mortar following the mix proportion as shown in Table 7.2. The thickness of the mortar cover was about 0.3 cm. It is assumed that the corrosion time of Fe-C coated LPFG sensor in the groove was the same as that of the Fe-C coated LPFG sensor close to the steel bar. The difference between them was that corrosion near the steel bar was accelerated by external current as indicated in Figure 7.4(b) and the corrosion in the Fe-C coating of the LPFG sensor in the groove occurred naturally. The spectra of the Fe-C coated LPFG attached to the steel bar were recorded every hour and the spectra of LPFG sensors encased in steel tubes were measured every day. The spectra of the Fe-C coated LPFG sensor placed in the mortar was also monitored periodically.

Table 7.2. The composition of mortar

Element	Cement	Water	Sand
Wt. %	1	0.5	2.81

(a)

(b)
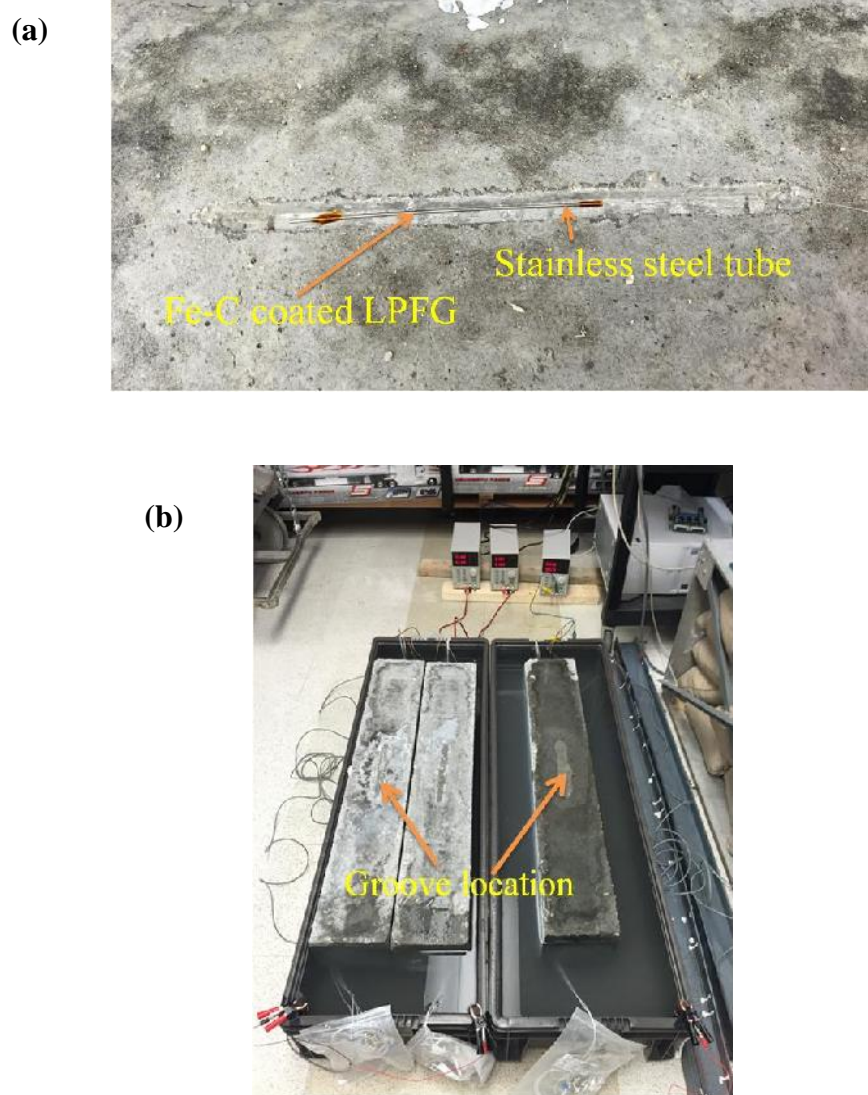
Figure 7.4. (a) Fe-C coated LPFG placed in the groove of the RC beam and (b) accelerated corrosion test setup.

When the steel reinforcement bars in a RC beam reached to each of five pre-determined corrosion stages, a four-point bending test was performed to investigate the load-deflection curve and the stiffness of the RC beam. The five stages correspond to no corrosion, a complete corrosion of the Fe-C coating, and a complete corrosion of three wall thicknesses of the steel tubes that were determined by a rapid change of resonant

wavelength of the LPFG sensors. Figure 7.5(a) illustrates the test setup of a RC beam in 30 in (75.0 cm) span length. The two loads are spaced 10.0 in (25.0 cm) apart. Figures 7.5(b) and 7.5(c) show the load test setup before and after the corrosion test, respectively. To prevent any stress concentration potentially caused by the uneven concrete surface, two rubber plates were placed at the two load points of the RC beam. A total of six steel plates with approximately 110 lbs each were applied to the beam one by one. The displacement at mid-point was recorded with a linear variable differential transformer (LVDT).
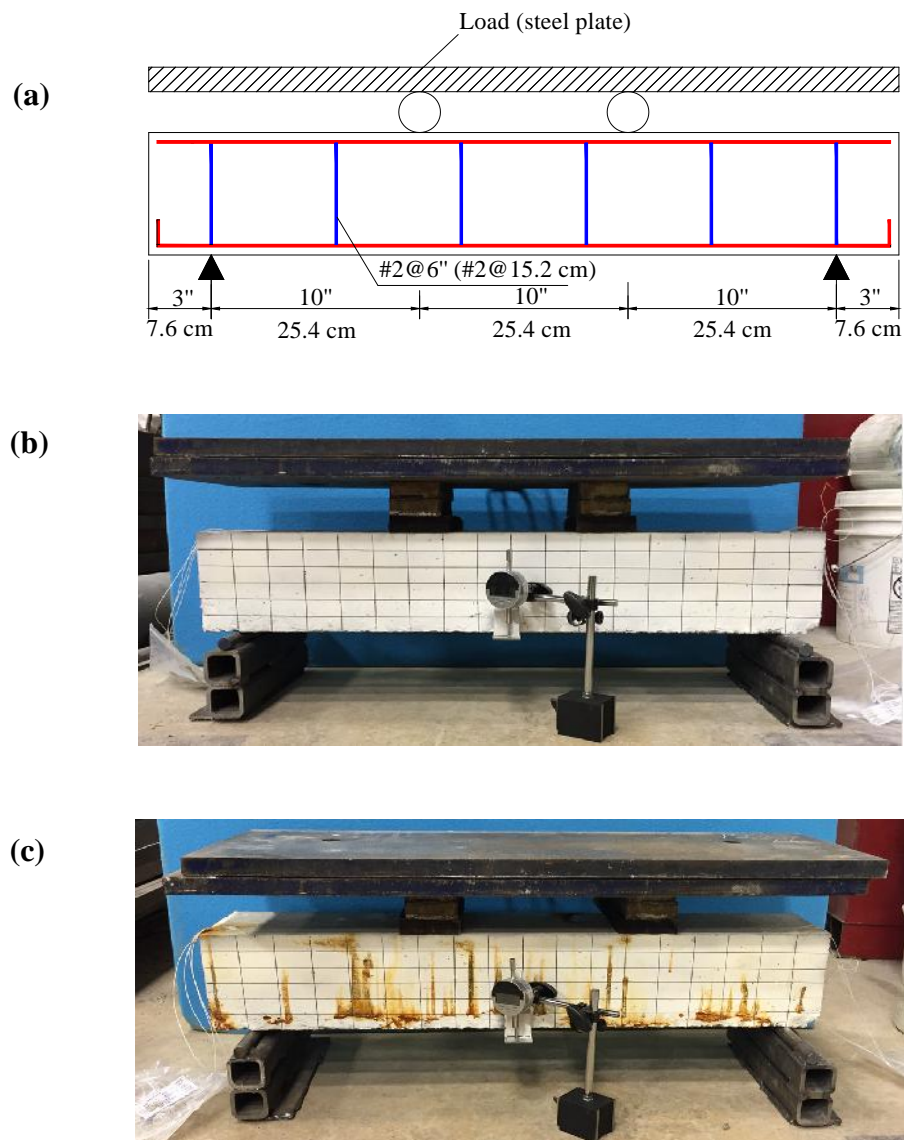
Figure 7.5. Four-point bending test setup: (a) schematic view, (b) prior to corrosion, and (c) after each level of corrosion.

7.3. RESULTS AND DISCUSSION

In this section, the change in resonant wavelength of Fe-C coated LPFG installed along the longitudinal steel bar and in the groove was obtained. The resonant wavelength over time of the steel tube encasing an bare LPFG was determined. Also, the effect of corrosion on the elastic flexural stiffness of the tested RC beams was investigated through the mechanical test.

7.3.1. Spectral Change of the Fe-C Coated LPFG Sensor. The transmission spectra of Fe-C coated LPFG sensors attached to steel bars in three RC beams, taken at various immersion durations, are presented in Figure 7.6. The resonant wavelengths over time of three beams and their average are shown in Figure 7.7. It can be observed from Figure 7.7 that the resonant wavelength of each beam was reduced for approximately 10 nm in the first 24 hours of test. With curve fitting, the average resonant wavelength of the three beams can be expressed as a function of time:

$$\Delta\}_{res} = -0.49t \ \ (0 \le t \le 24 \, \text{hours}) \tag{7.3}$$
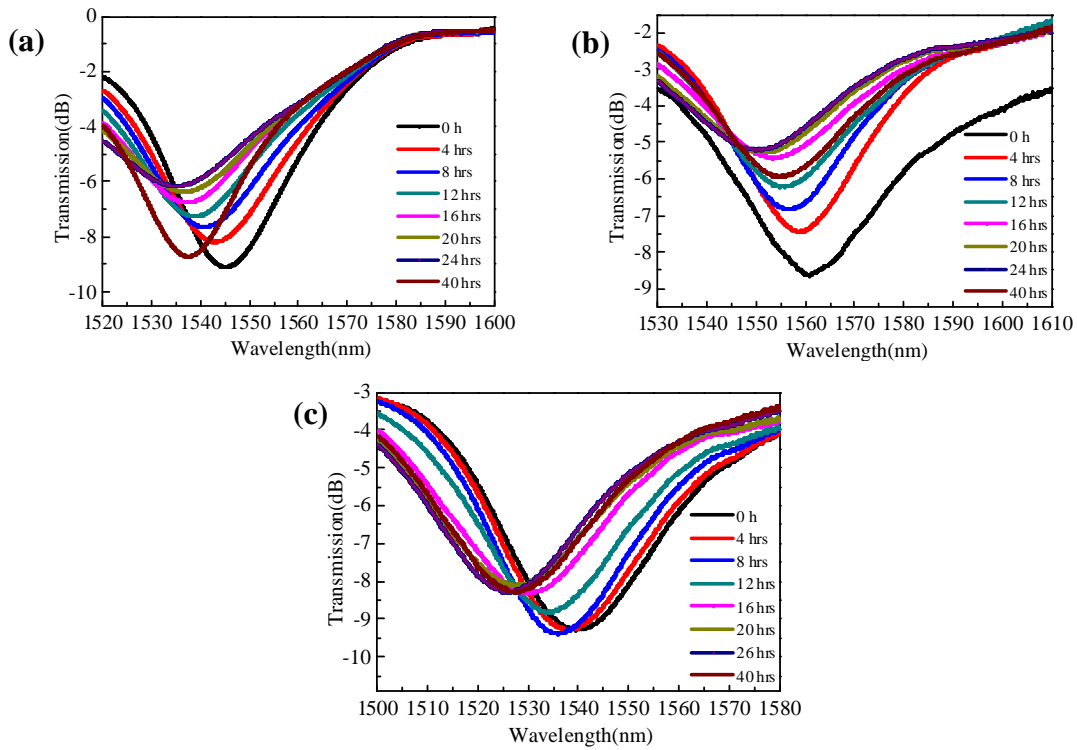
Figure 7.6. The transmission spectra of Fe-C coated LPFG sensors in: (a) Beam #1, (b) Beam #2, and (c) Beam #3.
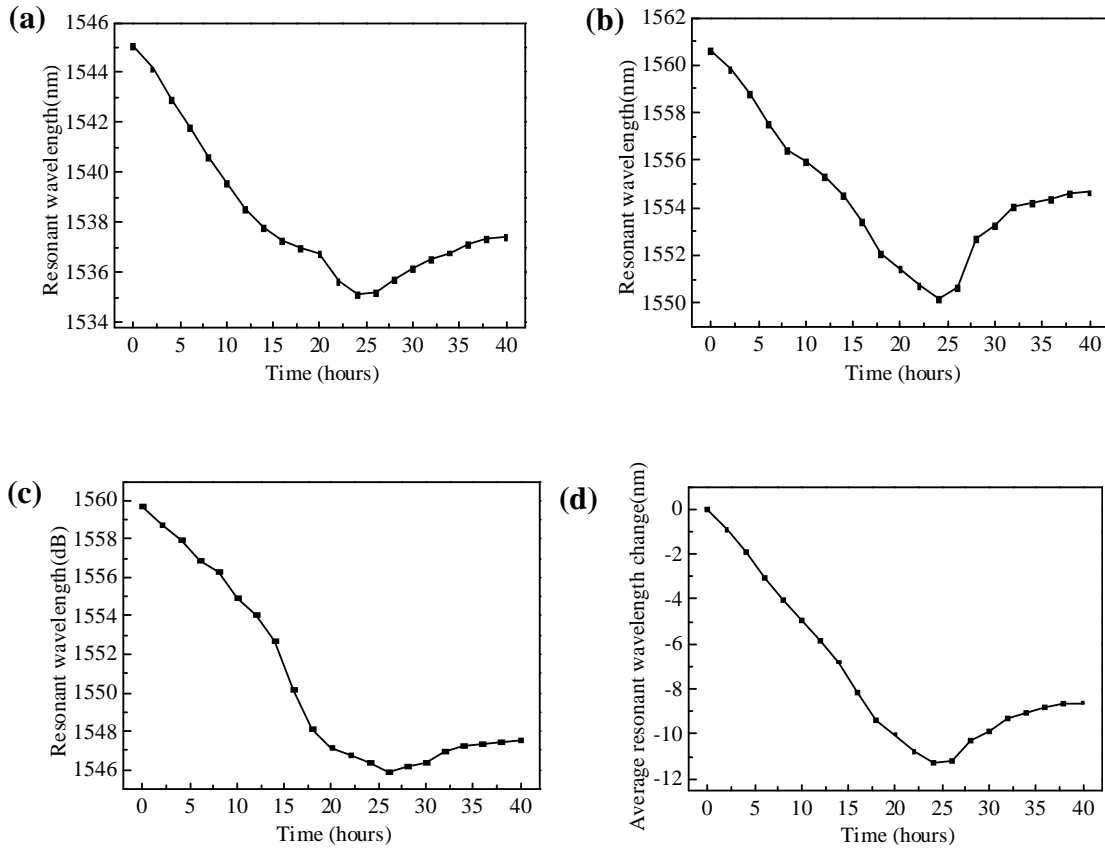
Figure 7.7. The resonant wavelength of Fe-C coated LPFG sensors in: (a) Beam #1, (b) Beam #2, and (c) Beam #3, and (d) the average of the three wavelengths.

7.3.2. LPFG Sensor Encased in a Steel Tube with Various Wall Thickness.

The spectra of LPFG sensors encased in steel tubes with a wall thickness of 0.50 mm, 0.75 mm and 1.00 mm were presented in Figures 7.8, 7.9 and 7.10, respectively. The time when the spectrum of each LPFG sensor was blue shifted rapidly is presented in Table 7.3 for all sensors installed in the three beams. Each rapid change in resonant wavelength corresponded to the complete penetration of a steel tube wall, which is simply referred to as the corrosion penetration depth. The corrosion penetration depth d (μm) and the time t (*days*) are presented in Figure 7.11 and, through linear regression with a coefficient of determination of 0.95, their relationship can be represented by:

$$d = 8.57t + 150 \quad (t > 40 \, \text{days}) \tag{7.4}$$
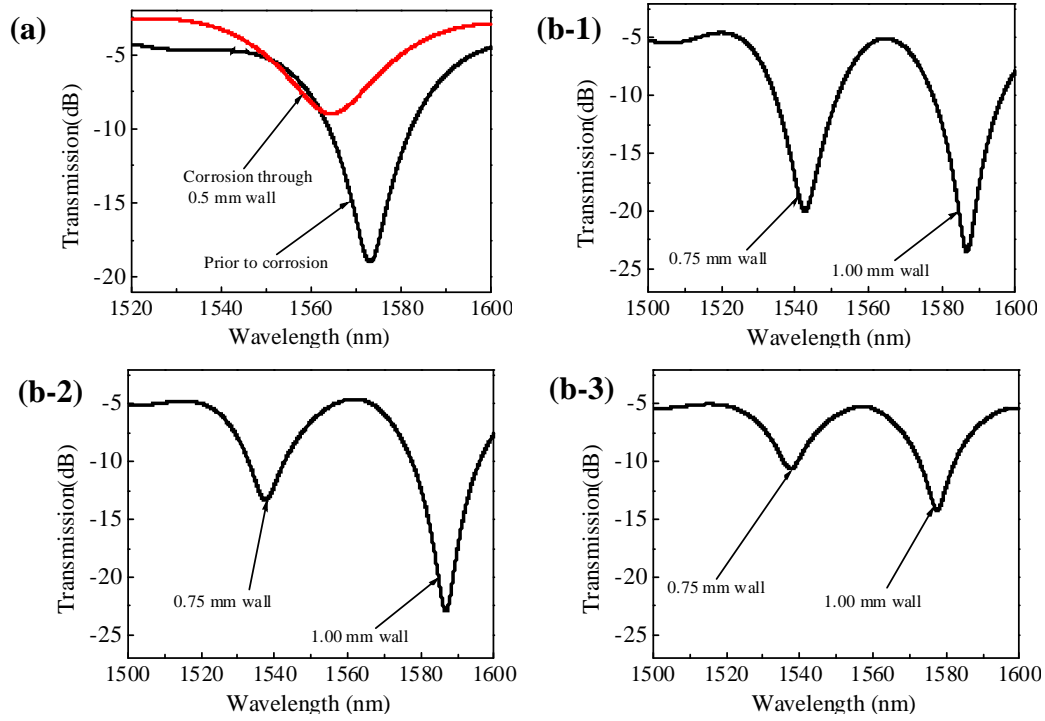
Figure 7.8. Spectra of the encapsulated LPFG sensors in Beam #1 with a wall thickness of: (a) 0.5 mm, and (b) 0.75 and 1.00 mm: (1) prior to corrosion, (2) 0.75 mm wall corroded, and (3) 1.00 mm wall corroded.
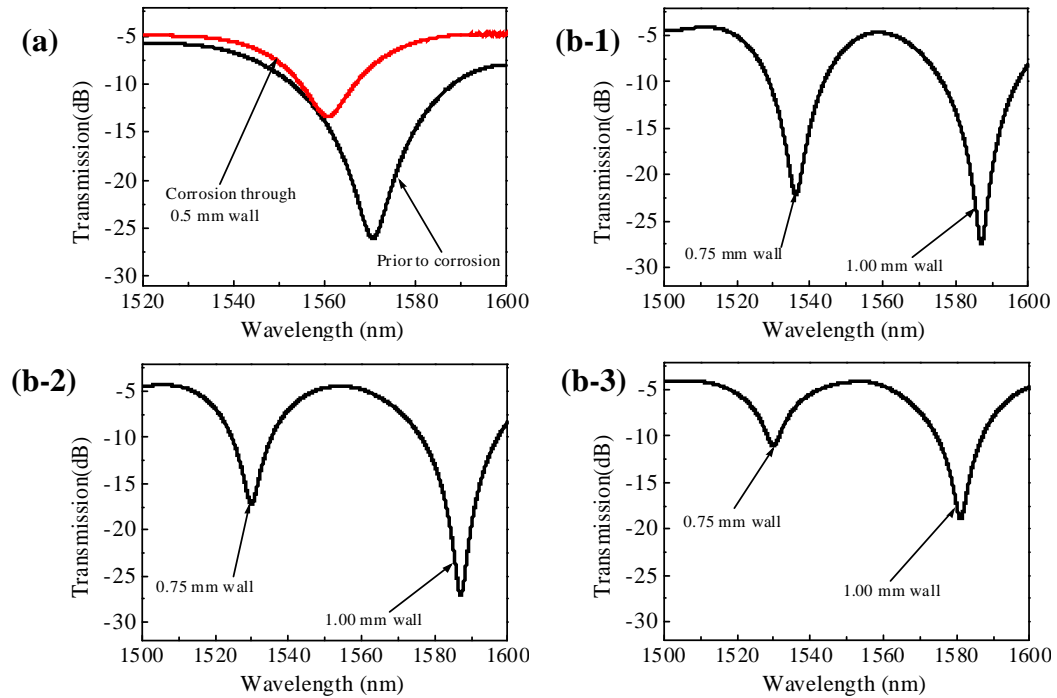
Figure 7.9. Spectra of the encapsulated LPFG sensors in Beam #2 with a wall thickness of: (a) 0.5 mm, and (b) 0.75 and 1.00 mm: (1) prior to corrosion, (2) 0.75 mm wall corroded, and (3) 1.00 mm wall corroded.
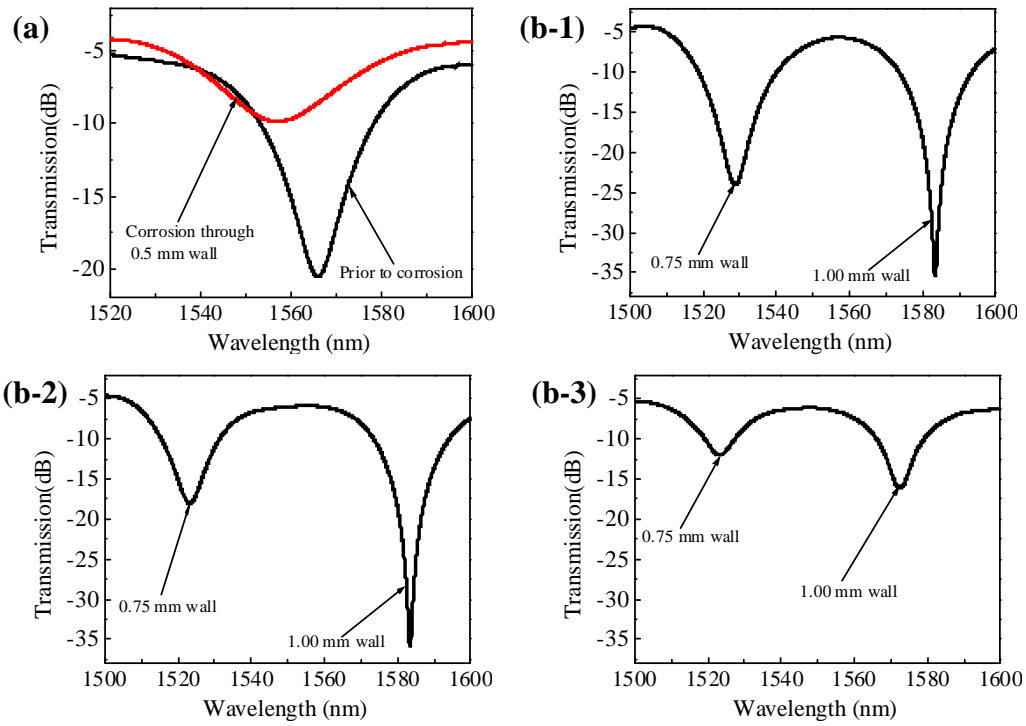
Figure 7.10. Spectra of the encapsulated LPFG sensors in Beam #3 with a wall thickness of: (a) 0.5 mm, and (b) 0.75 and 1.00 mm: (1) prior to corrosion, (2) 0.75 mm wall corroded, and (3) 1.00 mm wall corroded.

Table 7.3. Corrosion time (days) at complete penetration of Fe-C layer and steel tubes

Specimen	Fe-C (µm)	0.50 mm	0.75 mm	1.00 mm
Beam 1	20.3	49	58	90
Beam 2	19.4	40	67	110
Beam 3	21.0	43	73	102
Avg.	20.2	44	65	101
Mass loss of steel bar (%)	0.30	6.62	9.78	15.20
Actual mass loss of steel bar (%)	NA	NA	NA	14.76
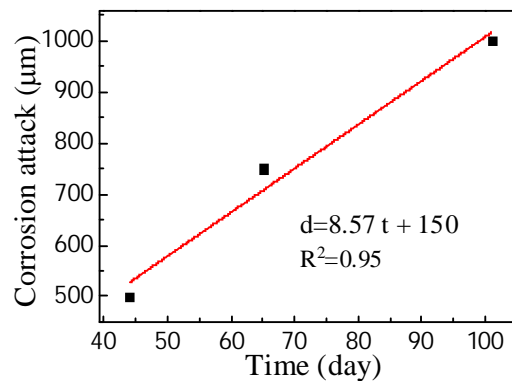
Figure 7.11. Corrosion penetration depth as a function of average corrosion time.

7.3.3. Fe-C Coated LPFG in the Groove. Figure 7.12 shows the transmission spectra of three Fe-C coated LPFG sensors embedded in the mortar grout of three RC beams. For these LPFG sensors, the deposition time of Ag film was 1.5 minutes and the electroplating time of Fe-C coating was 90 minutes. The spectra of the LPFG sensors were measured every day and changed over time as shown in Figure 7.12. The change of their resonant wavelengths as a function of time is presented in Figure 7.13 for individual specimens. The average of the three wavelengths is included in Figure 7.13(d). It can be observed from Figure 7.13 that the resonant wavelength is monotonically reduced in the first 11 days of test. The change in resonant wavelength over time can be linearly fitted by:

$$\Delta\}_{res} = -0.95\,t\,(0 \le t \le 11\,\text{days}) \tag{7.5}$$
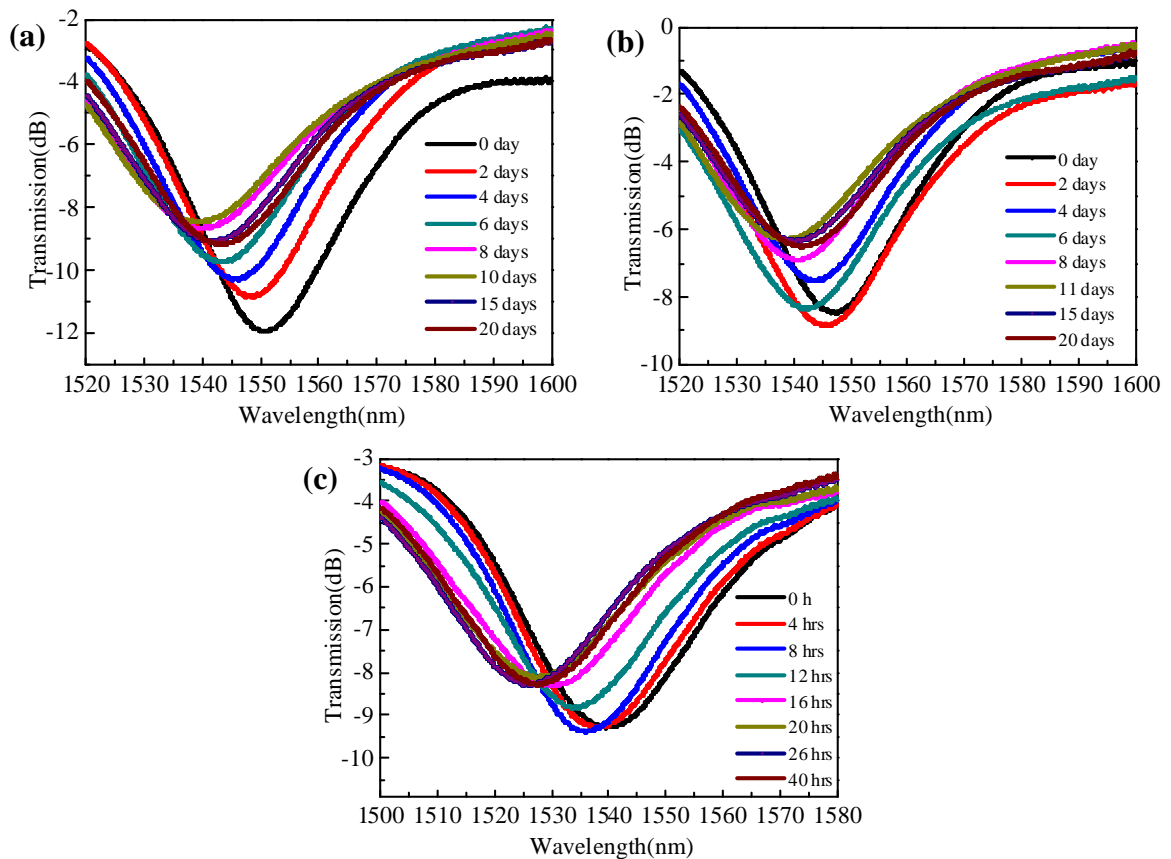
Figure 7.12. The transmission spectra of three Fe-C coated LPFG sensors embedded in the groove of: (a) Beam #1, (b) Beam #2, and (c) Beam #3.
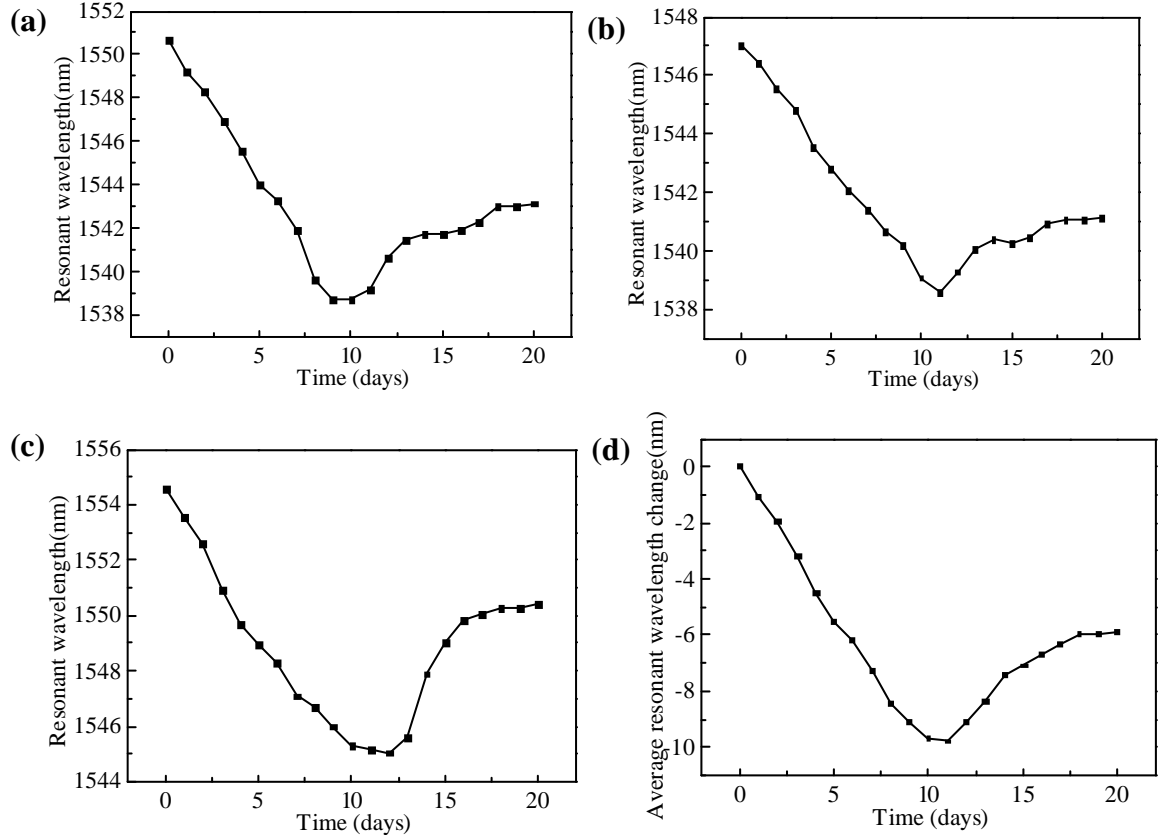
Figure 7.13. Resonant wavelengths of three Fe-C coated LPFG sensors embedded in the groove of: (a) Beam #1, (b) Beam #2, and (c) Beam #3, and (d) the average of the three wavelengths.

7.3.4. Capacity Reduction of RC Beams. The compressive strengths of three concrete cylinders were 26.3, 30.2 and 32.5 MPa, respectively. Their average compressive strength was approximately 30 MPa. Prior to concrete cracking, the stiffness of a RC beam was determined by the overall cross section dimension and concrete properties since the reinforcement ratio is small. Using 10% of the average compressive strength as the tensile strength of plain concrete, which is 3 MPa, the crack moment of the beam was calculated from the bending stress in the extreme fiber as follows:

$$\frac{0.076\,M}{\frac{1}{12}\times 0.152^4} = 3\times 10^6 \ \text{ or } \ M = 1756\,Nm \tag{7.6}$$

Since the RC beam was tested in the four-point bending setup, the load applied at 1/3 and 2/3 span corresponding to concrete cracking was estimated to be 6.9 kN (1.6 kips). The total load applied on the beam was approximately 13.8 kN (3.2 kips). A total

of eight steel plates were placed one by one on top of the RC beam, each weighing approximately 1.1 kN (220 lbs). Thus, the total load 2*F* gradually applied on the beam was 0, 2.2 kN, 4.4 kN, 6.6 kN and 8.8 kN in each step. The maximum applied load 2*F* of 8.8 kN (1.76 kips) was significantly smaller than 13.8 kN, the load 2*F* corresponding to concrete cracking. The stiffness of the beam in elastic state can be calculated by dividing the single applied load *F* by the mid-span deflection. Under two concentrated loads applied at 1/3 and 2/3 span or the total load of 2*F*, the mid-span deflection can be determined by:

$$\Delta = \frac{Fa}{24EI}\left(3l^2 - 4a^2\right) \tag{7.7}$$

where Δ is the mid-span deflection, *F* is the single load applied at 1/3 and 2/3 span, *E* is the modulus of elasticity, *I* is the moment of inertia, *l* is the span length of the beam between two supports, and *a* is the distance between the two loads.

Figure 7.14 illustrates the experimental load-deflection curves of three RC beams at five corrosion stages corresponding to no corrosion, a complete penetration of Fe-C coating, and a complete penetration of three steel tube walls that are 0.5 mm, 0.75 mm, and 1.00 mm thick, respectively. The stiffness of the beams was obtained by calculating the slope of load-deflection curves in Figure 7.14. Figure 7.15 shows the calculated EI values of the three beams at various corrosion stages from Eq. (7.7). The calculated EI value of each beam as shown in Figure 7.15 was normalized by the initial EI value prior to corrosion tests. The average of the three normalized EI values is presented in Figure 7.16 at various corrosion stages, which is simply referred to as a stiffness reduction coefficient.

It can be observed from Figure 7.16 that the stiffness reduction factor of the RC beams changed little over time. This is because there is only one corrosion-induced longitudinal crack in each beam so that the change in overall moment of inertia of the cross section is negligible. Figure 17(a) shows a crack appeared on the bottom face of Beam #1. In parallel with the longitudinal steel bars, the crack is wider than 1.0 mm when the maximum corrosion depth reached 0.75 mm. At the end of corrosion tests, the corroded steel bar was exposed as shown in Figure 7.17(b) and its surface condition was

examined. Corrosion products were observed on the inside surface of the crack as displayed in Figure 7.17(c).
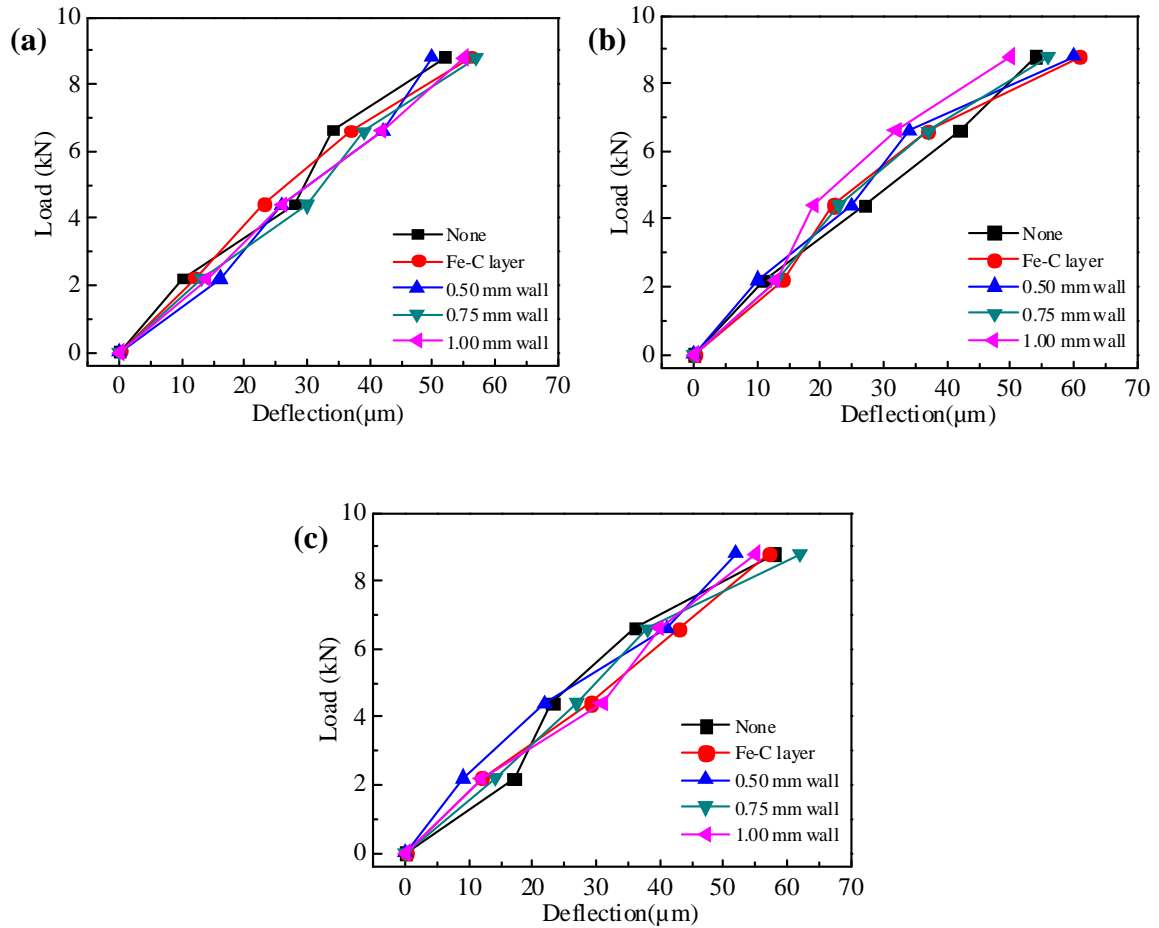
Figure 7.14. Load-deflection curves of: (a) Beam #1, (b) Beam #2 and (c) Beam #3.
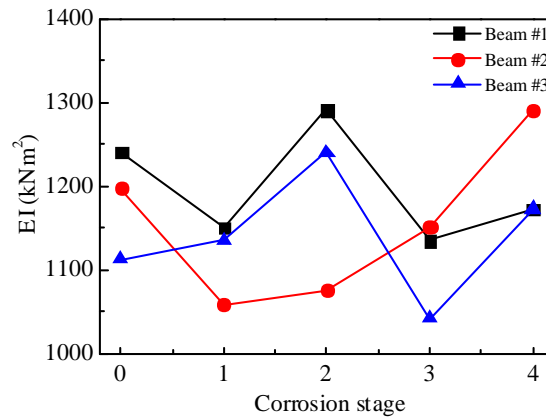
Figure 7.15. The EI of three RC beams at various corrosion stages.
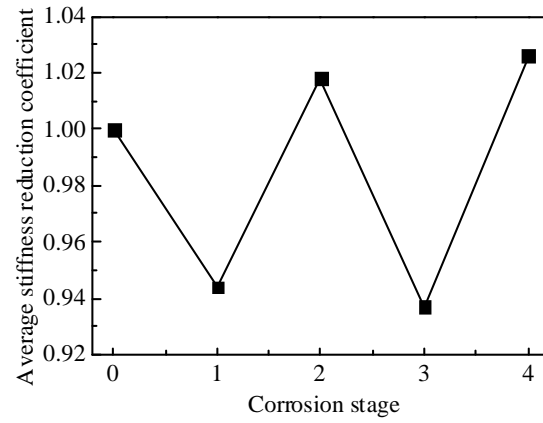
Figure 7.16. A stiffness reduction factor of three beams at various corrosion stages.
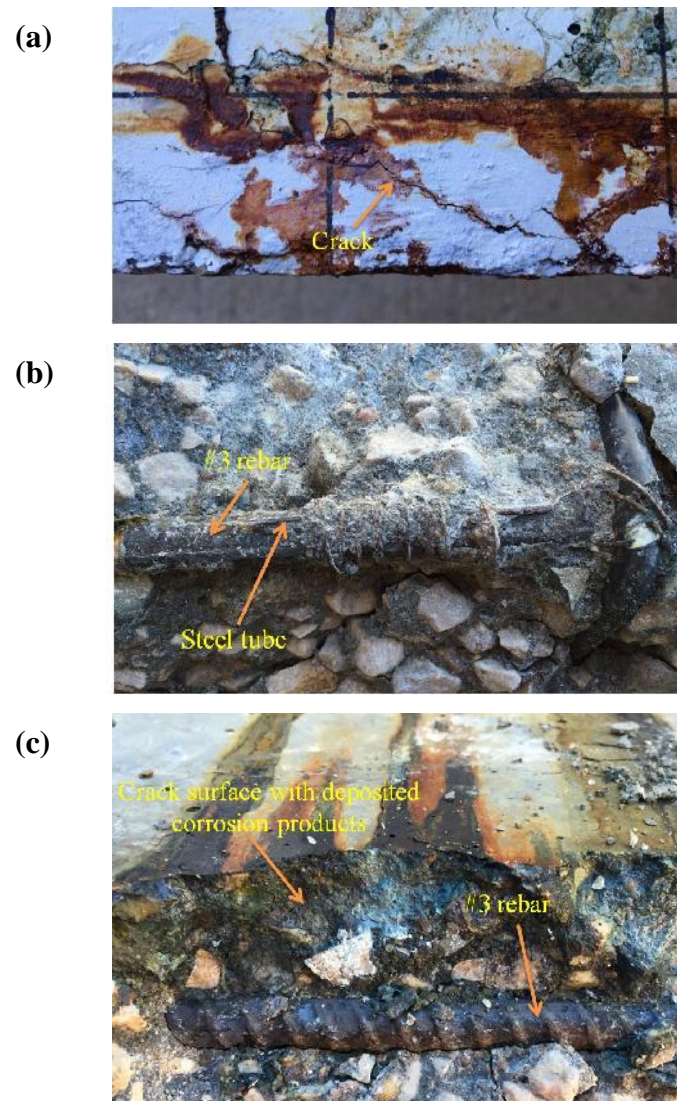
Figure 7.17. One corrosion-induced crack and corroded steel bar in each beam.

7.4. CONCLUSIONS

In this study, both the Fe-C coated and steel tube encapsulated LPFG corrosion sensors were embedded in RC beams along steel bars during casting to test their applicability for new construction or in a groove covered with mortar grout to test their applicability for existing structures. After each of five stages of accelerated corrosion, the RC beams were subjected to four-point bending tests. The effect of corrosion on the mechanical behavior of the RC beams was evaluated. At the end of corrosion tests, visual inspections were performed to investigate the sign of corrosion both in the steel bars and the corrosion sensors. Based on the test results, the following conclusions can be drawn:

(1) The change in resonant wavelength (nm) of the Fe-C coated sensor can be linearly related to the immersion time (hour) by $\Delta\}_{res} = -0.49\,t$ in the first 24 hours, when installed along the longitudinal steel bar, and by $\Delta\}_{res} = -0.95\,t$ in the first 11 days, when installed in the groove and covered with mortar grout. This sensor is appropriate for short-term monitoring of corrosion in application.

(2) The wall thickness d (μm) of the steel tube encasing an LPFG sensor can be related to the immersion time t (day) when the resonant wavelength is rapidly changed by $d = 8.57\,t + 150$ after more than 40 days of corrosion tests. This sensor is appropriate for long-term monitoring of corrosion in application.

(3) The effect of corrosion on the elastic flexural stiffness of the tested RC beams is negligible since there is only one corrosion-induced crack in longitudinal direction parallel to the longitudinal reinforcement bars.

8. CONCLUSIONS AND FUTURE WORK

8.1. MAIN CONCLUSIONS FROM THE OVERALL DISSERTATION

In this dissertation, long period fiber grating (LPFG) sensors and optical probes (OPs) were investigated to monitor and assess the life-cycle corrosion condition of RC structures with accelerated corrosion tests. Based on extensive tests and analysis, the main findings and results are summarized in three main components: short-term monitoring, long-term monitoring, and life-cycle performance evaluation.

8.1.1. Short-term Monitoring. LPFG sensors with an inner layer of Ag film and an outer layer of Fe-C coating can be applied for short-term corrosion monitoring of the Fe-C coating and the steel bars placed nearby in the same corrosive environment. The performance and specifications of the sensors are briefly described below:

(1) Given a Ag film of 0.8 µm thick, the change in resonant wavelength of the sensors decreases from 0.23 nm to approximately 0.15 nm per 1% corrosion-induced mass loss of the Fe-C coating that is originally set to be 8 µm to 20 µm thick. When the Ag film becomes 1.2 µm thick, the effect of the Fe-C thickness on the LPFG sensitivity is negligible. Therefore, the evanescent field depth around an LPFG sensor likely ranges from 0.8 µm to 1.2 µm.

(2) The change in resonant wavelength of the sensors is linearly related to the loss of Fe-C mass. Therefore, the sensors can be used to predict the corrosion mass loss of the Fe-C coating up to 60~90% by measuring the change in resonant wavelength.

(3) When the Fe-C coated LPFG sensors are embedded in mortar, two stages of resonant wavelength change are observed: a rapid drop in the first 7 days of immersion in salt solution and a slow increase due to corrosion initiation and the loss of Fe-C film. The rapid drop is attributed to the penetration of NaCl solution through the mortar cover, the Ag film, and the Fe-C coating, corresponding to a stage that the nearby steel bar is in passive state. The slow increase is attributed to corrosion initiation and the generation of corrosion products, corresponding to a stage that the steel bar is in active state.

8.1.2. Long-term Monitoring. OPs or LPFG sensors can be encapsulated in steel tubes for long-term corrosion monitoring of the steel tubes and the steel bars placed

nearby in the same corrosive environment. The performance and specifications of the OPs and LPFG sensors are briefly described below:

(1) Pitting corrosion occurs in the middle of a steel tube in $Ca(OH)_2$ and 3.5wt. % NaCl solution and crevice corrosion at the two ends with epoxy resin. The non-uniform pitting corrosion penetrates through the wall thickness of the tube locally, while crevice corrosion penetration depths the perimeter of the steel tube evenly.

(2) The corrosion pit penetration depth of the steel tube in $Ca(OH)_2$ and 3.5wt. % NaCl solution can be linearly related to the time when the reflectivity of the OP changes suddenly. Therefore, the OP can be used for long-term monitoring of critical pitting corrosion in steel.

(3) The corrosion environment of steel tubes in saturated $Ca(OH)_2$ and 3.5 wt. % NaCl solution is similar to steel bars corroded in concrete. The time of penetration t (month) as a function of wall thickness d (μm) is represented by $d = 129\,t - 135$.

(4) In saturated $Ca(OH)_2$ and 3.5 wt. % NaCl solution, the average pitting corrosion rate of a steel tube encapsulated LPFG sensor depends on the surface area of the steel tube. As the wall of the steel tube becomes thicker, the average pitting corrosion rate increases due to the increased surface area.

(5) When the LPFG sensors embedded in mortar are subjected to accelerated corrosion test in 3.5wt. % NaCl solution at a corrosion rate of 100 $\mu A/cm^2$, the time of penetration t (month) as a function of wall thickness d (μm) is $d = 137\,t - 72.9$.

8.1.3. Life-Cycle Performance Evaluation. The Fe-C coated LPFG sensors and the LPFG sensors encased in steel tubes were validated for their performance in three RC beams. Both the transmission spectra of sensors and the load strengths of RC beams were measured in five corrosion stages.

(1) For the Fe-C coated LPFG sensor installed during casting of the RC beams to simulate its application in new construction, the change in resonant wavelength $\Delta\}_{res}$ (nm) can be linearly related to the time t (hour) in the first 24 hours of corrosion test. Their relationship can be expressed into $\Delta\}_{res} = -0.49\,t\ (0 \le t \le 24\,\text{hours})$.

(2) For the Fe-C coated LPFG sensor installed after casting of the RC beams to simulate its application in existing structure. The change in resonant wavelength (nm)

over time (hour) in the first 11 days can be represented by

$\Delta\}_{res} = -0.95\,t \;\; (0 \le t \le 11\,\text{days}\,)$.

 (3) For the steel tube encapsulated LPFG sensor installed during casting of the RC beams, the thickness of the steel tube d (µm) can be linearly related to the time t (day). Their relation can be expressed into $d = 8.57\,t + 150\;\;(t > 40\,\text{days})$.

 (4) The effect of corrosion on the flexural stiffness of RC beams is negligible in the test range when the applied load is much lower than that corresponding to concrete cracking. However, the corrosion sensor can be used to monitor the long-term corrosion-induced mass loss of steel bars in RC structures.

8.2. FUTURE WORK

 The proof-of-concept study has successfully demonstrated the promising features and viability of the proposed LPFG sensors and OPs for short- and long-term corrosion monitoring and condition assessment of RC structures. However, the performance of the LPFG sensors and probes may be influenced by temperature, humidity, and strain. The Fe-C coated sensor is also fragile and difficult to transport. The Fe-C coating is easy to be oxidized. Future efforts should be directed to address the following topics:

 8.2.1. Temperature, Strain and Corrosion Sensors in Series. The temperature, strain and corrosion sensors can be multiplexed in series to measure multiple parameters in one measurement through one optical fiber. For example, two fiber Bragg grating (FBG) sensors are applied for temperature and strain measurements and one LPFG sensor for corrosion monitoring. The temperature and strain measurements by the FBG sensors can be used to compensate their effect on the corrosion monitoring results by the LPFG sensor.

 8.2.2. Packaging of Corrosion Sensor. The Fe-C coated LPFG corrosion sensor in this proof-of-concept study was just operated in the laboratory due to its fragile nature. In order to apply the sensor into engineering structures, the sensor must be further packaged to increase its protection from damage during transportation, prevent the Fe-C coating from direct contact with other materials, and prevent the Fe-C coating from being oxidized by storing it in a vacuum container.

BIBLIOGRAPHY

[1]   J. L. Briaud, P. Gardoni, C. Yao, "Bridge Scour Risk," *Geotechnical News*, Vol. 24, pp. 1193-1210, 2006.

[2]   T. Cheewaket, C. Jaturapitakkul, W. Chalee, "Initial corrosion presented by chloride threshold penetration of concrete up to 10 year-results under marine site," *Construction and Building Materials*, Vol. 37, pp. 693-698, 2012.

[3]   H. Yu, X. Shi, W. H. Hartt, B. Lu, "Laboratory investigation of reinforcement corrosion initiation and chloride threshold content for self-compacting concrete," *Cement and Concrete Research*, Vol. 10, pp. 1507-1516, 2010.

[4]   H.Bohni, *Corrosion in reinforced concrete structures*, Cambridge, UK, Woodhead Publishing, 2005.

[5]   A. Poursaee, *Corrosion of Steel in Concrete Structures*, Cambridge, UK, Woodhead Publishing, 2016.

[6]   S. K. Verma, S. S. Bhadauria, and S. Akhtar, "Monitoring Corrosion of Steel Bars in Reinforced Concrete Structures," *The Scientific World Journal*, Vol. 2014, pp. 1-9, 2014.

[7]   P. Ghods, O.B. Isgor, G. McRae, T. Miller, "The effect of concrete pore solution composition on the quality of passive oxide films on black steel reinforcement," *Cement Concrete Comp.*, Vol. 31, pp. 1507-1516, 2010.

[8]   X. Feng, Y. Zuo, Y. Tang, X. Zhao, X. Lu, "The degradation of passive film on carbon steel in concrete pore solution under compressive and tensile stresses," *Electrochim. Acta*, Vol. 58, pp. 258-263, 2011.

[9]   H. Yu, X. Shi, W. H. Hartt, B. Lu, "Three-dimensional corrosion pit measurement and statistical mechanical degradation analysis of deformed steel bars subjected to accelerated corrosion," *Constr. Build. Mater.*, Vol. 70, pp. 104-117, 2014.

[10]   R. Zhang, A. Castel, R. Francois, "Concrete cover cracking with reinforcement corrosion of RC beam during chloride-induced corrosion process," *Cement and Concrete Research*, Vol. 40, pp. 415-425, 2010.

[11]   M.J. Shannag, S.A. Al-Ateek, "Flexural behavior of strengthened concrete beams with corroding reinforcement," *Constr. Build. Mater.*, Vol. 20, pp. 834-840, 2006.

[12]   G.H. Koch, M.P.H. Brongers, N.G. Thompson, Y.P. Virmani, J.H. Payer, "Corrosion costs and preventive strategies in the United States," *Publication No. FHWA-RD-01-156, NACE International*, Houston, TX, USA, 2002.

[13]   A. Brenna, L. Lazzari, M. Ormellese, B. Lu, "Monitoring chloride-induced corrosion of carbon steel tendons in concrete using a multi-electrode system," *Constr. Build. Mater.*, Vol. 96, pp. 434-441, 2015.

[14]   S.P. Karthick, S. Muralidharan, V. Saraswathy, K. Thangavel, B. Lu, "Long-term relative performance of embedded sensor and surface mounted electrode for corrosion monitoring of steel in concrete structures," *Sensor Actuat B: Chem.*, Vol. 192, pp. 303-309, 2014.

[15]   A. Legat, "Monitoring of steel corrosion in concrete by electrode arrays and electrical resistance probes," *Electrochim. Acta*, Vol. 52, pp. 7590-7598, 2007.

[16]   P. Castro, A.A. Sagues, E.I. Moreno, L. Maldonado, J. Genesca, "Characterization of activated titanium solid reference electrodes for corrosion testing of steel in concrete," *Corrosion*, Vol. 52, pp. 609-617, 1996.

[17]   G.S. Duffo, S.B. Farina, C.M. Giordano, "Characterization of solid embeddable reference electrodes for corrosion monitoring in reinforced concrete structures," *Electrochim. Acta*, Vol. 54, pp. 1010-1020, 2009.

[18]   S. Patil, B. Karkare, S. Goyal, "Accoustic emission via-a-vis electrochemical techniques for corrosion monitoring of reinforced concrete element," *Constr. Build. Mater.*, Vol. 68, pp. 326-332, 2014.

[19]   A. Sharma, S. Sharma, S. Sharma, A. Mukherjee, "Altrasonic guided waves for monitoring corrosion of FRP wrapped concrete structures," *Constr. Build. Mater.*, Vol. 96, pp. 690-702, 2015.

[20]   H. Kim, "Chloride penetration monitoring in reinforced concrete structrure using carbon nanostraw/cement composte," *Constr. Build. Mater.*, Vol. 96, pp. 29-36, 2015.

[21]   J.M. Gandia-Romero, R. Bataller, P. Monzon, I. Campos, E. Garcia-Breijo, M. Valcuende, J. Soto, "Characterization of embeddable potentiometeric thick-film sensors for monitoring chloride penetration in concrete," *Sensor Actuat. B: Chem.*, Vol. 222, pp. 408-417, 2016.

[22]   M.J. Correia, E.V. Pereira, M.M. Salta, I.T.E. Fonseca, "Sensor for oxygen evaluation in concrete," *Cement Concrete Comp.*, Vol. 28, pp. 226-232, 2006.

[23]   S. Dong, C. Lin, R. Hu, L. Li, R. Du, "Effective monitoring of corrosion in reinforced steel in concrete constructions by a multifunctional sensor," *Electrochim. Acta*, Vol. 56, pp. 1881-1888, 2011.

[24]   Y. Huang, F. Tang, X. Liang, G. Chen, H. Xiao, and F. Azarmi, "Steel Bar Corrosion Monitoring with Long Period Fiber Grating Sensors Coated with Nano Iron/Silica Particles and Polyurethane," *Struct. Health Mon.*, Vol. 14, pp. 178-189, 2015.

[25]   Ying Huang, Zhan Gao, Genda Chen, and Hai Xiao, "Long Period Fiber Grating Sensors Coated with Nano Iron/Silica Particles for Corrosion Monitoring," *Smart Materials and Structures*, Vol. 22, pp. 964-1001, 2013.

[26]   Genda Chen, Brandon Schafer, Zhibin Lin, Ying Huang, Oscar Suaznabar, Jerry Shen, and Kornel Kerenyi, "Maximum Scour Depth Based on Magnetic Field Change of Smart Rocks for Foundation Stability Evaluation of Bridges," *Structural Health Monitoring*, Vol. 14, pp. 86-99, 2015.

[27]   H. Li, D. Li, G. Song, "Recent applications of fiber optic sensors to health monitoring in civil engineering," *Eng. Struct.*, Vol. 26, pp. 1647-1657, 2015.

[28]   A.V. Tregubov, V.V. Svetukhin, S.G. Novikov, A.V. Berintsev and V.V. Prikhodko, "A novel fiber optic distributed temperature and strain sensor for building applications," *Results in Physics*, Vol. 6, pp. 131-132, 2016.

[29]   Cezary Kaczmarek, "Spectral-domain measurement of the strain sensitivity of phase modal birefringence of polarization-maintaining optical fibers," *Optics Communications*, Vol. 375, pp. 43-48, 2016.

[30]   D. Wada, H. Igawa and H. Murayama, "Simultaneous distributed measurement of the strain and temperature for a four-point bending test using polarization-maintaining fiber Bragg grating interrogated by optical frequency domain reflectometry," *Measurement*, Vol. 94, pp. 745-752, 2016.

[31]   H. Sun, S. Yang, X.i Zhang, L. Yuan, Z. Yang and M. Hu, "Simultaneous measurement of temperature and strain or temperature and curvature based on an optical fiber Mach–Zehnder interferometer," *Optics Communications*, Vol. 340, pp. 39-43, 2015.

[32]   T. K. Noh, U. Ryc and Y. W. Lee, "Compact and wide range polarimetric strain sensor based on polarization-maintaining photonic crystal fiber," *Sensors and Actuators A: Physical*, Vol. 213, pp. 89-93, 2014.

[33]   J. Kang , X. Dong, Y. Zhu, S. Jin and S. Zhuang, "A fiber strain and vibration sensor based on high birefringence polarization maintaining fibers," *Optics Communications*, Vol. 322, pp. 105-108, 2014.

[34]   A.A. Jasim, N. Hayashi, S.W. Harun, H. Ahmad, R. Penny, Y. Mizuno and K. Nakamura, "Refractive index and strain sensing using inline Mach–Zehnder interferometer comprising perfluorinated graded-index plastic optical fiber," *Sensors and Actuators A: Physical*, Vol. 219, pp. 94-99, 2014.

[35]   J. Zhenga, P. Yan, Y. Yu, Z. Ou, J. Wang, X. Chen and C. Du, "Temperature and index insensitive strain sensor based on a photonic crystal fiber in line Mach–Zehnder interferometer," *Optics Communications*, Vol. 297, pp. 7-11, 2013.

[36]   H. Sun, M. Hu, Q.u Rong, Y. Du, H. Yang and X. Qiao, "High sensitivity optical fiber temperature sensor based on the temperature cross-sensitivity feature of RI-sensitive device," *Optics Communications*, Vol. 323, pp. 28-31, 2014.

[37]   Qi Wang, Chao Du, Jiaming Zhang, Riqing Lv and Yong Zhao, "Sensitivity-enhanced temperature sensor based on PDMS-coated long period fiber grating," *Optics Communications*, Vol. 377, pp. 89-93, 2016.

[38]   Tao Hu, Yong Zhao and An-ning Song, "Fiber optic SPR sensor for refractive index and temperature measurement based on MMF-FBG-MMF structure," *Sensors and Actuators B: Chemical*, Vol. 237, pp. 521-525, 2016.

[39]   A. Urrutia , J. Goicoechea, A. L. Ricchiuti, D. Barrera and S. Sales, "Simultaneous measurement of humidity and temperature based on a partially coated optical fiber long period grating," *Sensors and Actuators B: Chemical*, Vol. 227, pp. 135-141, 2016.

[40]   F. Wang, H. Zhu, Y. Li, H.i Zhao, X. Wang and Y. Liu, "Comparative study on a core-offset fiber temperature sensor between the faraday rotation mirror structure and the double coupling structure," *Optics Communications*, Vol. 367, pp. 286-291, 2016.

[41]   C. Chu and C. Lin, "Optical fiber sensor for dual sensing of temperature and oxygen based on PtTFPP/CF embedded in sol–gel matrix," *Sensors and Actuators B: Chemical*, Vol. 195, pp. 259-265, 2014.

[42]   P. Rinaudo, I. Paya-Zaforteza , P. Calderón and S. Sales, "Experimental and analytical evaluation of the response time of high temperature fiber optic sensors," *Sensors and Actuators A: Physical*, Vol. 243, pp. 167-174, 2016.

[43]   G. Krishnan, N. Bidin, M. Abdullac, M. F. S. Ahmad, M. A. A. Bakar and M. Yasin, "Liquid refractometer based mirrorless fiber optic displacement sensor," *Sensors and Actuators A: Physical*, Vol. 247, pp. 227-233, 2016.

[44]   S. Tao, X. Dong and B. Lai, "Temperature-insensitive fiber Bragg grating displacement sensor based on a thin-wall ring," *Optics Communications*, Vol. 372, pp. 44-48, 2016.

[45] M. Shan, R. Min, Z. Zhong , Y. Wang and Y. Zhang, "Differential reflective fiber-optic angular displacement sensor," *Optics & Laser Technology*, Vol. 68, pp. 124-128, 2015.

[46] Yuhe Li, Kaisen Guan and Zhaohui Hu, "Fiber optic displacement measurement model based on finite reflective surface," *Optics & Laser Technology*, Vol. 84, pp. 32-39, 2016.

[47] A. Sun, Z. Wu and H. Huang, "Power-compensated displacement sensing based on single mode-multimode fiber Bragg grating structure," *Optics Communications*, Vol. 311, pp. 140-143, 2013.

[48] Y. Zhang, Y. Zhao and Q. Wang, "Improved design of slow light interferometer and its application in FBG displacement sensor," *Sensors and Actuators A: Physical,* Vol. 214, pp. 168-174, 2014.

[49] D. Jauregui-Vazquez , J.M. Estudillo-Ayala, A. Castillo-Guzman, R. Rojas-Laguna, R. Selvas-Aguilar, E. Vargas-Rodriguez, J.M. Sierra-Hernandez, V. Guzman-Ramos and A. Flores-Balderas, "Highly sensitive curvature and displacement sensing setup based on an all fiber micro Fabry–Perot interferometer," *Optics Communications,* Vol. 308, pp. 289-292, 2013.

[50] Y. Wang, C. Shen , W. Lou and F. Shentu, "Polarization-dependent humidity sensor based on an in-fiber Mach-Zehnder interferometer coated with graphene oxide," *Sensors and Actuators B: Chemical,* Vol. 234, pp. 503-509, 2016.

[51] Y. Wang, C. Shen , W. Lou and F. Shentu, "Fiber optic humidity sensor based on the graphene oxide/PVA composite film," *Optics Communications,* Vol. 372, pp. 229-234, 2016.

[52] L. Alwis, T. Sun and K.T.V. Grattan, "Optical fibre-based sensor technology for humidity and moisture measurement: Review of recent progress," *Measurement,* Vol. 46, pp. 4052-4074, 2013.

[53] M.D. Fernández-Ramos , Y. F. Ordóñez, L.F. Capitán-Vallvey, I.M. P. Vargas-Sansalvador and J. Ballesta-Claver, "Optical humidity sensor using methylene blue immobilized on a hydrophilic polymer," *Sensors and Actuators B: Chemical,* Vol. 220, pp. 528-533, 2015.

[54] A. Lokman, H. Arof and S.W. Harun, "Tapered fiber coated with hydroxyethyl cellulose/polyvinylidene fluoride composite for relative humidity sensor," *Sensors and Actuators A: Physical,* Vol. 225, pp. 128-132, 2015.

[55] L. Xia, L. Li, W. Li, T. Kou and D. Liu, "Novel optical fiber humidity sensor based on a no-core fiber structure," *Sensors and Actuators A: Physical,* Vol. 190, pp. 1-5, 2013.

[56] J. Ascorbe , J.M. Corres, I.R. Matias and F.J Arregui, "High sensitivity humidity sensor based on cladding-etched optical fiber and lossy mode resonances," *Sensors and Actuators B: Chemical,* Vol. 233, pp. 7-16, 2016.

[57] P. Zubiate, C.R. Zamarreño, I. Del Villar, I.R. Matias and F.J Arregui, "Tunable optical fiber pH sensors based on TE and TM Lossy Mode Resonances (LMRs)," *Sensors and Actuators B: Chemical,* Vol. 231, pp. 484-490, 2016.

[58] B. Schyrr, S. Pasche, E. Scolan, R. Ischer and D. Ferrario, "Development of a polymer optical fiber pH sensor for on-body monitoring application," *Sensors and Actuators B: Chemical,* Vol. 194, pp. 238-248, 2014.

[59] W. Li , H. Cheng, M. Xia and K. Yang, "An experimental study of pH optical sensor using a section of no-core fiber," *Sensors and Actuators A: Physical,* Vol. 199, pp. 260-264, 2013.

[60] T. H. Nguyen, T. Venugopala, S. Chen, T. Sun, K. T.V. Grattan, S. E. Taylor, P.A. M. Basheer and A. E. Long, "Fluorescence based fibre optic pH sensor for the pH 10–13 range suitable for corrosion monitoring in concrete structures," *Sensors and Actuators B: Chemical,* Vol. 191, pp. 498-507, 2014.

[61] D. Luo, , Y. Yue , P. Li, J. Ma, L. Zhang, Z. Ibrahim and Z. Ismail, "Concrete beam crack detection using tapered polymer optical fiber sensors," *Measurement*, Vol. 88, pp. 96-103, 2016.

[62] Z. Chen, Y. Yang, Y. Xie, B. Guo and Z. Hu, "Non-contact crack detection of high-speed blades based on principal component analysis and Euclidian angles using optical-fiber sensors," *Sensors and Actuators A: Physical*, Vol. 201, pp. 66-72, 2013.

[63] Khalil Al Handawi, Nader Vahdati, Paul Rostron, Lydia Lawand, Oleg Shiryayev, "Strain based FBG sensor for real-time corrosion rate monitoring in pre-stressed structures," *Sensors and Actuators B: Chemical*, Vol. 236, pp. 276-285, 2016.

[64] C.H. Tan, Y.G. Shee, B.K. Yap and F.R. Mahamd Adikan, "Fiber Bragg grating based sensing system: Early corrosion detection for structural health monitoring," *Sensors and Actuators A: Physical*, Vol. 246, pp. 123-128, 2016.

[65] S. Dong, Y. Liao, Q. Tian, Y. Luo, Z. Qiu, S. Song, "Optical and electrochemical measurement for optical fiber corrosion sensing techniques," *Corros. Sci.*, Vol. 48, pp. 1746-1756, 2006.

[66] C.K.Y. Leung, K. Wan, L. Chen, "A novel optical fiber sensor for steel corrosion in concrete structures," *Sensors*, Vol. 8, pp. 1960-1976, 2008.

[67]   W. Hu, H. Cai, M. Yang, X. Tong, C. Zhou, W. Chen, "Fe-C coated fibre bragg grating sensor for steel corrosion monitoring," *Corros. Sci.*, Vol. 53, pp. 1933-1938, 2011.

[68]   J. Gao, J. Wu, J. Li, X. Zhao, "Monitoring of corrosion in reinforced concrete structure using Bragg grating sensing," *NDT&E International*, Vol. 44, pp. 1933-1938, 2015.

[69]   S. W. James, R.P. Tatam, "Optical fiber long period grating sensors: characteristics and application," *Meas. Sci. Technol.*, Vol. 14, pp. 49-61, 2003.

[70]   T. Venugopaplan, T. Sun, K.T.V. Grattan, B. Lu, "Long period grating based humidity sensor for potential structural health monitoring," S*ensor Actuat. A: Phys.*, Vol. 148, pp. 57-62, 2008.

[71]   S. Khaliq, S.W. James, R.P. Tatam, "Fiber optic liquid level sensor using a long period grating," *Opt. Lett.*, Vol. 26, pp. 1224-1226, 2001.

[72]   S.M. Topliss, S.W. James, F. Davis, S.P.J. Higson, R.P. Tatam, "Optical fibre long period grating based selective vapour sensing of volatile organic compounds," *Sensor Actuat. B: Chem.*, Vol. 143, pp. 629-634, 2010.

[73]   T. Wang, S. Korposh, S. James, R. Tatam, S.W. Lee, "Optical fiber long period grating sensor with a polyelectrolyte alternate thin film for gas sensing of amine odors," *Sensor Actuat. B: Chem.*, Vol. 185, pp. 117-124, 2013.

[74]   J. Tang, S. Cheng, W. Hsu, T. Chiang, L. Chau, "Fiber optic biochemical sensing with a colloidal gold-modified long period fiber grating," *Sensor Actuat. B: Chem.*, Vol. 119, pp. 105-109, 2006.

[75]   R. Garg, S.M. Tripathi, K. Thyagarajan, W.J. Bock, "Long period fiber grating based temperature-compensated high performance sensor for bio-chemical sensing applications," *Sensor Actuat. B: Chem.*, Vol. 176, pp. 1121-1127, 2013.

[76]   Y. Chen, F. Tang, Y. Bao, Y. Tang, and G. Chen, B. Lu, "A Fe-C coated long-period fiber grating for corrosion-induced mass loss measurement," *Opt. Lett.*, Vol. 41, pp. 2306-2309, 2016.

[77]   H. Song, and V. Saraswathy, "Corrosion Monitoring of Reinforced Concrete Structures-A Review," *International Journal of Electrochemical Science*, Vol. 2, pp. 1-68, 2007.

[78]   M. Stern, and A.L. Geary, "Electrochemical Polarization I. A Theoretical Analysis of the Shape of Polarization Curves," *Journal of the Electrochemical Society*, Vol. 104, pp. 56-63, 1967.

[79]   ASTM C876 (1999). Standard Test Method for Half-cell Potentials of Uncoated Reinforcing Steel in Concrete, *American Society of Testing and Materials*, West Conshohocken, PA.

[80]   P. Gu, and J.J. Beaudoin, "Obtaining Effective Half-cell Potential Measurements in Reinforced Concrete Structures," Construction Technology Update No. 18, Institute for Research in Construction, National Research Council of Canada (1998).

[81]   M. Pour-Ghaz, O. B. Isgor, and P. Ghods, "Quantitative interpretation of half-cell potential measurements in concrete structures," *Journal of Materials in Civil Engineering*, Vol. 31, pp. 616, 1989.

[82]   S. Millard, J. Harrison and A. Edwards, *Br. J. Nondestructive Testing*, pp. 467-475, 2009.

[83]   P.G.Cavalier and P.R.Vassie, "Investigation and repair of reinforced corrosion in a bridge deck," *In Proceedings of Institution of Civil Engineers*, Vol. 70, pp. 461-480, 1981.

[84]   "Protection of Metals in Concrete Against Corrosion," *ACI 222R-01*, American Concrete Institute, Michigan, USA, pp. 25, 2001.

[85]   F. Mansfeld, "Polarization Resistance Measurement, Electrochemical Techniques for Corrosion," *National Association of Corrosion Engineers*, pp. 18-26, 1977.

[86]   D.A. Jones, "Principles and prevention of corrosion," *Prentice-Hall,* Upper Saddle River, NJ, 1996.

[87]   J. Flis, S. Sabol, H.W. Pickering, A. Sehgal, K. Osseo-Asare and P.D. Cady, "Electrochemical Measurements on Concrete Bridges for Evaluation of Reinforcement Corrosion Rates," *Corrosion Engineering*, Vol. 49, pp. 601-613, 1993.

[88]   M.A. Pech-Canul and P. Castro, "Corrosion measurements of steel reinforcement in concrete exposed to a tropical marine atmosphere," *Cement and Concrete Research*, Vol. 32, pp. 491-498, 2002.

[89]   W. Morris, A. Vico, M. Vazquez and S.R. de Sanchez, "Absolute values of instantaneous corrosion rates by faradaic rectification," *Journal of Electroanalytical Chemistry and Interfacial Electrochemistry*, Vol. 62, pp. 209-218, 1975.

[90]   J.S.Gill, L.M.Callow, J.D.Scantlebury, "Corrosion Measurements Derived from Small Perturbation Non-Linearity—Part 1: Harmonic Analysis," *Corrosion*, Vol. 39, pp. 61-66, 1989.

[91]   D.A.Eden and A.N.Rothwell, "Electrochemical Noise Data: Analysis Interpretation and Presentation," *NACE International*, pp. 1-12, 1992.

[92]   A. Legat and C. Zevnik, "The electrochemical noise of mild and stainless steel in various water solutions," *Corrosion science*, Vol. 35, pp. 1661-1666, 1993.

[93]   J.A. Wharton, R.J.K. Wood and B.G. Mellor, "Wavelet analysis of electrochemical noise measurements during corrosion of austenitic and superduplex stainless steels in chloride media," *Corrosion science*, Vol. 45, pp. 97-122, 2003.

[94]   R.A. Cottis, M.A.A. Al-Awadhi, H. Al-Mazeedi and S.Turgoose, "Measures for the detection of localized corrosion with electrochemical noise," *Electrochimica Acta*, Vol. 46, pp. 3665-3674, 2001.

[95]   A. Aballe, M. Bethencourt, F.J. Botana and M. Marcos, "Using wavelets transform in the analysis of electrochemical noise data," *Electrochimica Acta*, Vol. 44, pp. 4805-4816, 1999.

[96]   X. Zhao, P. Gong, G. Qiao, J. Lu, X. Lv and J. Qu, "Brillouin Corrosion Expansion Sensors for Steel Reinforced Concrete Structures Using a Fiber Optic Coil Winding Method," *Sensors*, Vol. 11, pp. 10798-10819, 2011.

[97]   W. Li, S. C. M. Ho and G. Song, "Corrosion detection of steel reinforced concrete using combined carbon fiber and fiber Bragg grating active thermal probe," *Smart Materials and Structures*, Vol. 25, 2016.

[98]   H. Liu, D. Liang. J. Zeng and J. Geng, "Long Period Fiber Grating Refractive Index Sensitivity-Based Reinforcing Rebar Corrosion Sensor in Concrete," *Acta Optica Sinica*, Vol. 31, 2016.

[99]   H. Liu, D. Liang. J. Zeng, J. Jin, J. Wu and J. Geng, "Design of Long Period Fiber Grating sensor for reinforcing bar corrosion," *Journal of Intelligent Material Systems and Structures*, Vol. 23, pp. 45-51, 2012.

[100] H.Xu, Z. Chen,B.Xu, andD.Ma, "Impact of lowcalciumfly ash on steel corrosion rate and concrete-steel interface," *The Open Civil Engineering Journal*, Vol. 6, pp. 1-7, 2012.

[101] M. Criado, D. M. Bastidas, S. Fajardo, A. Fern´andez-Jim´enez, and J. M. Bastidas, "Corrosion behaviour of a new low-nickel stainless steel embedded in activated fly ash mortars," *Cement and Concrete Composites*, Vol. 33, pp. 644-652, 2011.

[102] M.Maslehuddin, Rasheeduzzafar, and A. I. Al-Mana, "Strength and corrosion resistance of superplasticized concretes," *Journal of Materials in Civil Engineering*, Vol. 4, pp. 108-113, 1992.

[103] K. K. Sideris and A. E. Savva, "Durability of mixtures containing calciumnitrite based corrosion inhibitor," *Cement and Concrete Composites*, Vol. 27, pp. 277-287, 2005.

[104] W. Morris and M. V´azquez, "A migrating corrosion inhibitor evaluated in concrete containing various contents of admixed chlorides," *Cement and Concrete Research*, Vol. 32, pp. 259-267, 2002.

[105] F. Tang, G. Chen, R. K. Brow, J. S. Volz and M. L. Koenigstein, "Corrosion resistance and mechanism of steel rebar coated with three types of enamel," *Corrosion Science*, Vol. 59, pp. 157-168, 2012.

[106] A. B. Darwin and J. D. Scantlebury, "Retarding of corrosion processes on reinforcement bar in concrete with an FBE coating," *Corrosion Science*, Vol. 59, pp. 157-168, 2012.

[107] S. U. Al-Dulaijan, M. Maslehuddin, M. Shameem, M. Ibrahim, and M. Al-Mehthel, "Corrosion protection provided by chemical inhibitors to damaged FBEC bars," *Construction and Building Materials*, Vol. 29, pp. 487-495, 2002.

[108] V. Nachiappan and E. H. Cho, "Corrosion of high chromium and conventional steels embedded in concrete," *Journal of Performance of Constructed Facilities*, Vol. 19, pp. 56-61, 2005.

[109] O. T. de Rinc´on, O. P´erez, E. Paredes, Y. Caldera, C. Urdaneta, and I. Sandoval, "Long-term performance of ZnO as a rebar corrosion inhibitor," *Cement and Concrete Composites*, Vol. 24, pp. 79-87, 2002.

[110] V. Saraswathy, H. Song, "Improving the durability of concrete by using inhibitors," *Building and Environment*, Vol. 42, pp. 464-472, 2007.

[111] M. Badawi and K. Soudki, "Control of corrosion-induced damage in reinforced concrete beams using carbon fiber-reinforced polymer laminates," *Journal of Composites for Construction*, Vol. 9, pp. 4195-201, 2005.

[112] I. A. Wootton, L. K. Spainhour and N. Yazdani, "Corrosion of Steel Reinforcement in Carbon Fiber-Reinforced Polymer Wrapped Concrete Cylinders," *Journal of Composites for Construction*, Vol. 7, pp. 339-347, 2003.

[113] A. S. Debaiky, M. F. Green, and B. B. Hope, "Carbon Fiber-Reinforced Polymer Wraps for Corrosion Control and Rehabilitation of Reinforced Concrete Columns," *International Concrete Abstracts Portal*, Vol. 99, pp. 129-137, 2002.

[114] C. Monticelli, A. Frignani, and G. Trabanelli, "A study on corrosion inhibitors for concrete application," *Cement and Concrete Research*, Vol. 30, pp. 635-642, 2000.

[115] X. Lan, Q. Han, J. Huang, H. Wang, Z. Gao, A. Kaur, H. Xiao, "Turn-around point long period fiber grating fabricated by CO2 laser for refractive index sensing," *Sensor Actuat. B: Chem.*, Vol. 177, pp. 1149-1155, 2013.

[116] C.C.C. Lam, R. Mandamparambil, T. Sun, K.T.V. Grattan, S.V. Nanukuttan, S.E. Taylor, P.A.M. Basheer, "Optical fiber refractive index sensor for chloride ion monitoring," *IEEE Sensors J.*, Vol. 9, pp. 525-531, 2009.

[117] L. Coelho, D. Viegas, J.L. Santos, J.M.M.M. de Almeida, "Characterization of zinc oxide coated with optical fiber long period gratings with improved refractive index sensing properties," *Sensor Actuat. B: Chem.*, Vol. 233, pp. 45-51, 2016.

[118] F. Tang, G. Chen, R.K. Brow, M.L. Koenigstein, "Corrosion resistance of a sand particle modified enamel coating applied to smooth steel bars," *Materials*, Vol. 7, pp. 6632-6645, 2014.

[119] B.V. Jegdic, J.B. Bajat, J.P. Popic, S.I. Stevanovic, V.B. Miskovic-Stankovic, "The EIS investigation of powder polyester coatings on phosphate low carbon steel: the effect of $NaNO_2$ in the phosphating bath," *Corros. Sci.*, Vol. 53, pp. 2872-2880, 2011.

[120] F. Tang, G. Chen, R.K. Brow, "Chloride-induced corrosion mechanism and rate of enamel- and epoxy-coated deformed steel bars embedded in mortar," *Cement Concrete Res*, Vol. 82, pp. 58-73, 2016.

[121] P. Cordoba-Torres, T.J. Mesquita, O. Devos, B. Tribollet, V. Roche, R.P. Nogueira, "On the intrinsic coupling between constant-phase element parameters and Q in electrochemical impedance spectroscopy," *Electrochim. Acta*, Vol. 72, pp. 172-178, 2012.

[122] W. Chen, R. Du, C. Ye, Y. Zhu, C. Lin, "Study on the corrosion behavior of reinforcing steel in simulated concrete pore soluton using in situ Raman spectroscopy assisted by electrochemical techniques," E*lectrochim. Acta*, Vol. 55, pp. 5677-5682, 2010.

[123] H.H. Hassan, E. Abdelghani, M.A. Amin, "Inhibition of mild steel corrosion in hydrochloric acid solution by triazole derivative: part I. Polarization and EIS studies," E*lectrochim. Acta*, Vol. 52, pp. 6359-6366, 2007.

[124] F. Tang, G. Chen, J.S. Volz, R.K. Brow, M.L. Koenigstein, "Cement-modified enamel coating for enhanced corrosion resistance of steel reinforcing bars," *Cement Concrete Comp.*, Vol. 35, pp. 171-180, 2013.

[125]   M. Criado, D.M. Bastidas, S. Fajardo, A. Fernandez-Jimenez, J.M. Bastidas, "Corrosion Behavior of a New Low-Nickel Stainless Steel Embedded in Activated Fly Ash Mortars," *Cement and Concrete Composites,* Vol. 33, pp. 644-652, 2011.

[126]   Z. Yao, Z. Jiang, F. Wang, "Study on Corrosion Resistance and Roughness of Micro-Plasma Oxidation Ceramic Coatings on Ti Alloy by EIS Technique," *Electrochimica Acta,* Vol. 52, pp. 4539-4546, 2007.

[127]   https://en.wikipedia.org/wiki/Fresnel_equations.

[128]   http://www.thefoa.org/tech/ref/testing/test/reflectance.html.

VITA

Yizheng Chen was born in the City of Jilin, Jilin, China. He was admitted to Tongji University, Shanghai, China, in 2005 and received his B.S. degree in Civil Engineering in 2009. He continued his graduate study in Tongji University and received his M.S. degree in Civil Engineering in 2011. He was then admitted into the PhD Program in Structures and Materials Engineering at China Institute of Water Resources and Hydropower Research, Beijing, China. In 2013, he discontinued his PhD Study in China and was admitted into the PhD program in Civil Engineering at Missouri University of Science and Technology under the supervision of Professor Genda Chen. He has served as a Graduate Research Assistant between January 2013 and December 2016 in the Department of Civil, Architectural, and Environmental Engineering. During this period, his research interests were focused on the innovation and application of fiber optic sensors for corrosion monitoring. He has authored one journal paper and two conference papers based on his dissertation work, and co-authored three journal papers and three conference papers on other topics. Another journal paper based on his Ph.D. dissertation was submitted in October 2016. In May 2017, he received his Ph. D. degree in Civil Engineering from Missouri University of Science and Technology, Rolla, Missouri.